# VECTOR FIELD GUIDED TOOL PATH FOR FIVE-AXIS MACHINING

BY

SAMART MOODLEAH

A DISSERTATION SUBMITTED IN PARTIAL FULFILLMENT OF
THE REQUIREMENTS FOR THE DEGREE OF DOCTOR OF
PHILOSOPHY (TECHNOLOGY)
SIRINDHORN INTERNATIONAL INSTITUTE OF TECHNOLOGY
THAMMASAT UNIVERSITY
ACADEMIC YEAR 2015

# VECTOR FIELD GUIDED TOOL PATH FOR FIVE-AXIS MACHINING

BY

SAMART MOODLEAH

A DISSERTATION SUBMITTED IN PARTIAL FULFILLMENT OF
THE REQUIREMENTS FOR THE DEGREE OF DOCTOR OF
PHILOSOPHY (TECHNOLOGY)
SIRINDHORN INTERNATIONAL INSTITUTE OF TECH
THAMMASAT UNIVERSITY
ACADEMIC YEAR 2015

VECTOR FIELD GUIDED TOOL PATH FOR FIVE-AXIS MACHINING

A Dissertation Presented

By

SAMART MOODLEAH

Submitted to

Sirindhorn International Institute of Technology

Thammasat University

In partial fulfillment of the requirements for the degree of

DOCTOR OF PHILOSOPHY (TECHNOLOGY)

Approved as to style and content by

Advisor and Chairperson of

Thesis Committee

_____

(Professor Stanislav Makhanov, Ph.D)

Co-Advisor

_____

(Associate Professor Bunyarit Uyyanonvara, Ph.D)

Committee Member and Chairperson
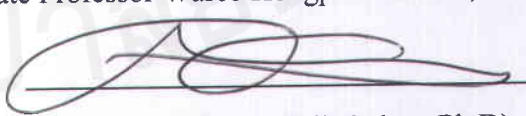
of Examination Committee

_____

(Professor Thanaruk Theeramunkong, D.Eng)

Committee Member

_____

(Associate Professor Waree Kongprawechnon, Ph.D)

Committee Member

_____

(Associate Professor Erik Bohez, Ph.D)

External Examiner: Professor Xun William Xu, Ph.D

JANUARY 2016

i

# Abstract

VECTOR FIELD GUIDED TOOL PATH FOR FIVE-AXIS MACHINING

by

SAMART MOODLEAH

B.Eng. (Electronic), Rajamangala Institute of Technology, 2003

M.Eng. (Information), King Mongkut's Institute of Technology Ladkrabang, 2007

Machining large complex industrial parts with a high accuracy often requires tens or hundreds of thousands of cutter location points and hundreds of hours of machining. That is why reducing the machining time is one of the most important topics in the optimization of CNC codes for 5-axis milling machines. We propose and analyze a new method of constructing curvilinear tool paths which partly or even entirely align with the direction of the maximum material removal rate. The alignment based on the curvilinear elliptic grid generation allows minimization of the machining time while keeping the convenient zigzag-like topology of the path. The method is applicable to a variety of cost functions such as the length of the path, the machining speed, the material removal rate, the kinematic error, etc., generating different machining strategies. The method has been combined with a new version of the adaptive space-filling curves. The material removal rate cost function has been tested against the tool path length minimization. The numerical and machining experiments demonstrate a considerable advantage of the proposed method.

We test the algorithm on parametric and STL surfaces and analyze the performance of the proposed method against the conventional methods by using virtual and real machining.

**Keywords**: kinematics of the milling machines, error minimization, toolpath planning

# Acknowledgement

# Table of Contents

# List of Figures

# List of Tables

# Chapter 1
# Introduction

High precision manufacturing of complex industrial parts often requires computer numerically controlled (CNC) machines designed as a combination of an NC machine and a computer control system. Nowadays, the CNC machines have become a standard manufacturing solution in the aircraft, aerospace, car, ship building, optical equipment medical device and implant industries, for high precision satellite parts and in many other important manufacturing processes. Five-axis machines are designed to control three translation axes and an additional pair of rotation axes. The five degrees of freedom are the minimum combination required to translate the tool into a required position and establish a required orientation [1]. It has been proven that the five-axis solutions usually outperform their three axis counterparts in terms of the accuracy and the ability to manufacture complex shaped parts. Of course, some parts will never become five-axis candidates; however, as long as the complex geometry and the high precision is involved, there always will be five-axis benefits.

The movements of the machine parts are guided by a controller which is fed with the so called NC program or the G-code. The G-code is a sequence of commands which can be generated manually or by a CAM system. The G-code allows for many functions such as G00 (point to point positioning), G01 (line interpolation), G02/G03 (circular interpolation), etc. G-code can also include acceleration and deceleration of the feed rate and many other ways to control the tool; however, one of the most popular ways to design the G-code is the G01 mode. In this case, the command includes three spatial coordinates of the tool-tip and a pair of rotation angles needed to establish the orientation of the tool.

Usually, the tool path generation algorithms compute the cutter contact (CC) points located on the part surface and offset them to generate the cutter location (CL) points which are the components of the G01 command [2]. For some naïve tool path strategies the CC and CL points may coincide, but the majority of the 5-axis algorithms use the tool inclination. Consequently, the tool path is generated as a sequence of CC points and orientations which are translated into the CL points and

1

further into a sequence of the machine coordinates and rotations of the machine tables.

The ultimate goals of tool path optimization are the minimal machining time, minimal tool wear and the maximum accuracy. Additionally, the tool path must provide safety during the machining, that is, it must avoid global collisions. Of course, these goals may contradict and are often mutually exclusive. Therefore, the tool path is usually a compromise between those criteria. For instance, the optimization can aim to reduce the total length of the toolpath or the total machining time, maintaining the prescribed accuracy.

The complex nature in five-axis machining often does not allow for a straightforward optimization of the basic criteria such as the machining time. Consequently, the optimization problems are formulated with regard to some variables which are related to the basic criteria such as the material removal rate, machining strip, or scallop height. The optimization can be subjected to certain constraints, the most important of which is gouging and global interference free positioning. The input parameters are the prescribed (possibly adaptive) tool path pattern, tool positions and orientations, tool geometry, forward step, feed rate, etc.

## 1.1 Literature Review

Our literature review is focused on toolpath generation and the tool orientation. There are many other aspects of five axis machining which are discussed in fairly comprehensive reviews [3,4] and the recent reviews [5,6].

### 1.1.1 Toolpath Generation

The goal of toolpath generation is to provide the sequence of cutter location points (CL-points) and the tool orientations to produce a given surface. Many advanced techniques have been proposed. In this section we will present classical and modern approaches to tool path generation.

- **Classical approaches**

The most popular toolpath patterns in five axis machining are the zigzag and the contour (spiral) paths. The CC (cutter contact) -points are allowed to move along these patterns to achieve feasible forward steps. This method is also known as iso-parametric. The term iso-parametric means that the zigzag or the spiral pattern is constructed in the parametric domain by fixing one of the two parameters in the surface parametric equations $S(u,v)$. For the spiral pattern, the parametric domain is presented in the polar coordinates [7,8].

Increasing the distance between the CC points (forward step) increases the interpolation and kinematics error. The maximum forward step can be evaluated using the bisection method [9]. Li et al.[10] present an approximation to the reference curve and obtain a closed-form solution to evaluate the forward step. An improvement of the accuracy by using multiple points on the tool tip is proposed in [11]. Tool path based on grid generation in the parametric domain is introduced [12,13]. The grid spacing is controlled by a weighting function based on the kinematic error.

The distance between the tool tracks is controlled by the scallop height constraint which leads to an unequal side step [11]. Moreover, the non-uniform distribution of scallops across the surface affects the machining efficiency [14-16]. Another drawback is that the iso-parametric path is not applicable to a complex surface, for instance, to a complex pocket milling with islands [17,18]. Such machining requires special algorithms capable of constructing the toolpath for trimmed surfaces whose boundaries are defined by intersections with other surfaces.

An alternative method intersects the given surface with a series of parallel planes and obtains the intersection points to perform a toolpath called the iso-planar path. As opposed to the iso-parametric path, this method is able to provide the toolpath for a complex surface. The iso-planar algorithm constructs and follows a contour map of the surface [19-21]. The scallop height constraints control the distance between the intersecting planes [14,22].

Park and Choi present a toolpath generation algorithm for direction-parallel milling which can handle multiple connecting areas [23] (see Figure 1.1). As opposed to the contour parallel toolpath which uses successive offsets of the area curves, the direction-parallel milling follows line segments parallel to a specified inclination. The algorithm consists of 3 modules: optimal inclination calculating and storing the tool-path elements, and tool-path linking. The contour map of the complex shaped surface can include several clusters of disconnected contours; therefore, the iso-planar method requires linking the clusters and minimizing the tool retractions [24,25]. The comparison between the directional parallel and contour-linking algorithm has been studied in [26]. The study demonstrated that the smooth zigzag path is the most efficient irrespective of the path interval and feed-rate. Figure 1.2 demonstrates the iso-parametric and iso-planar concepts.



(a)                                                                (b)
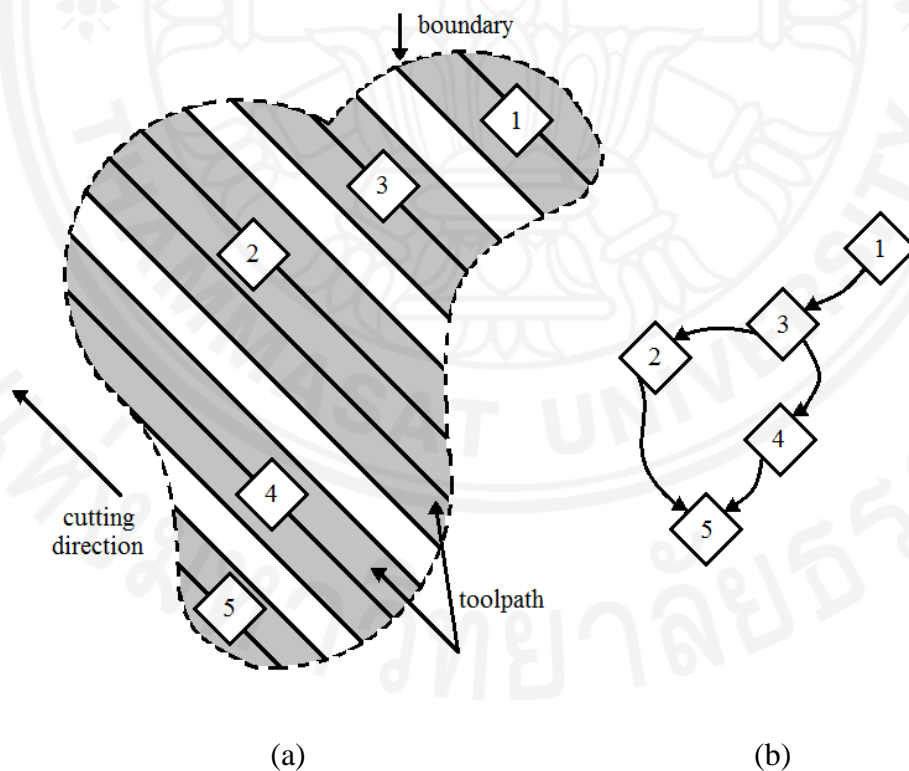
Figure 1.1: Direction-parallel milling (a) toolpath and regions (b) connecting regions.
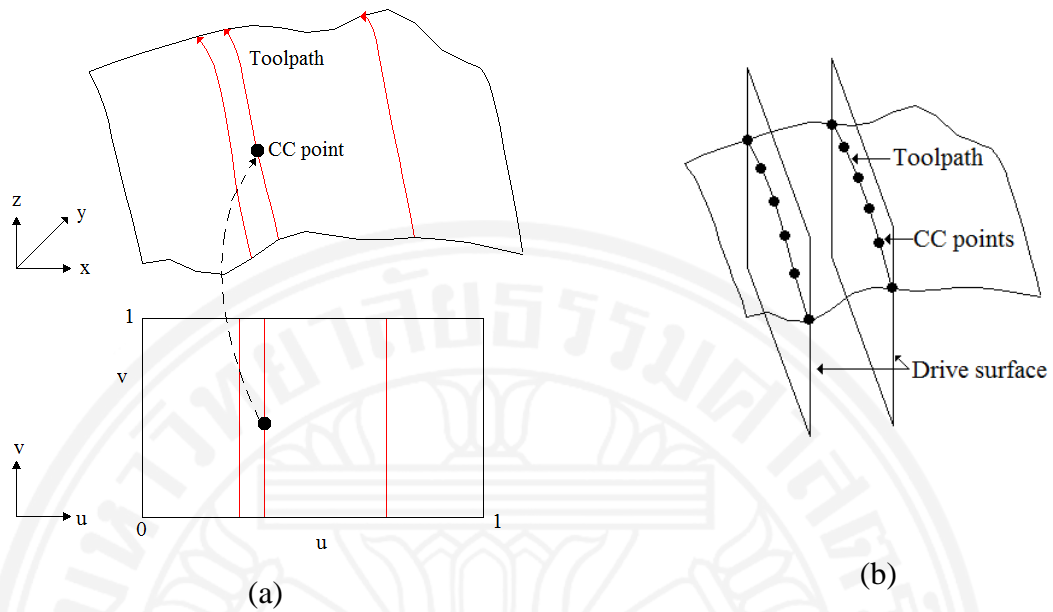
Figure 1.2: Toolpath generation concept (a) iso-parametric (b) iso-planar

Neither the iso-parametric nor the iso-planar method is capable of producing a constant scallop height because the distance between adjacent tracks is based on the maximum allowed scallop height. Therefore, another class of methods called the iso-scallop methods has been introduced in [27]. The initial track is generated and the CC points at the maximum distance which meet the prescribed scallop height constant are evaluated. The first path is usually parallel to the surface boundary and will be used as a base curve for the child paths across the surface. The path interval is calculated by using 2D swept sections of the tool along the tracks, based on the assumption that the swept sections are coplanar or perpendicular to tangent vectors to the principle scallop curve.

The evaluation of the tool path intervals in 3D case has been proposed in [14]. The tool envelop surface is constructed while the tool moves along the toolpath by sweeping a circle which represents the cutter. The toolpath interval is computed by the horizontal distance between the adjacent tracks. A similar approach for three-axis ball-end machining presented [28] uses bisection to find the scallop curve and tool center. Unfortunately, besides its high computational cost the method heavily relies on the initial path.

Sub-optimal path patterns for layer-by-layer rough cutting have been introduced in [29]. Jensen [30] presents a toolpath generation and tool positioning method based on curvature matching between the surface and an effective cutter shape. Ideally, a gouging free toolpath is automatically generated by this approach. However, the proposed algorithm is based on an approximation of the actual cutting shape. The generalized cutter projection methods have been presented in [31,32] .

- **Modern approaches**

The complexity of the part surfaces is one of the reasons why many tool path planning strategies fail. Partition of the entire surface into several sub-surfaces has been well known for 3-axis machining [6]. With some modifications the idea applies to the 5-axis mode.

An iso-phote is the region on the surface in which the angle between a reference vector V and the normal vector n does not exceed a prescribed tolerance angle $\theta$ [33], (see Figure 1.3). In other words, the surface is segmented into regions having close normals. It means that in the 3 axis mode approximately the same path interval can be applied. The boundary of the surface is defined as the initial master toolpath. Then the curve is projected onto a 2D plane to perform the curve offsetting. Finally, the resulted 2D offset curves are projected onto a 3D surface [33-37]. A similar segmentation technique based on the surface curvature can be used for 3-axis and 5-axis machining [42]. Lee and Ji [38] partition the surface into subregions using the first and the second fundamental forms [39] and classify subregions using the differential geometric characteristics such as the Gaussian curvature and the mean curvature. Based on that, the surfaces are classified into six types [8]: concave elliptic, convex elliptic, hyperbolic, concave parabolic, convex parabolic and planar umbilical. Furthermore, the subregions can be defined based on the six prescribed types.
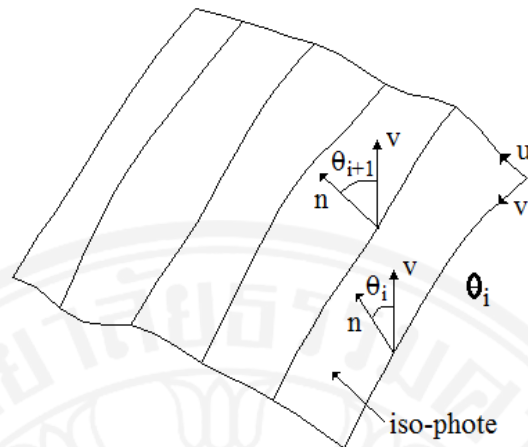
Figure 1.3: concept of iso-phote toolpath.

A surface partition technique using clustering of vector fields of optimal directions has been presented [40,41]. The resulting toolpath is a combination of the standard zigzag or spiral patterns constructed for the individual patches [40-43] connected using a linking strategy [24]. The tool follows a nearly optimal path; however, complex vector fields may require too many clusters. Liu et al. [44] propose a regional-based toolpath using a tensor-based surface subdivision strategy. The optimization objective is described as a rank two tensor in which a tensor field can be established across the surface. The degenerate points of the tensor field are extracted to construct the internal boundaries.

The standard industrial solutions usually include the standard zigzag and spiral patterns which are two particular cases of the space filling curves (SFC). However, other types of the SFCs are applicable. As a matter of fact, the SFC is a well-known pattern searching method in computer graphics, image processing and information systems [45-49]. The first applications of the SFC to the NC toolpath generation are [50,51]. The recently proposed patterns are the Hilbert SFC [50,52-54], the adaptive SFC (ASFC) [55-59], and the biased space filling curves (BSFC) [60]. The advantage of the conventional SFCs such as the Hilbert, Peano or Morton curves is the local refinement property; that is, the SFC can be changed locally to improve the accuracy of the tool path without reconstructing the entire curve. However, the frequent turns make the conventional SFCs impractical for 5 axis machining.

7

The adaptive SFC (ASFC) [61] is a combination of two techniques. The first method is based on grid generation methods whereas the second employs the classical SFC approach. The ASFC is designed to reduce the number of sharp turns; however, it requires a discretized parametric region, usually a rectangular or a curvilinear grid. Therefore, the ASFC toolpath generation is composed of three steps: grid construction, SFCs generation, and correction of the generated SFCs to further reduce the number of the turns (BSFC) and smooth the sharp turns. This framework originally presented in [12] was further developed in [13,62]. It has been demonstrated that the conventional zigzag or spiral toolpath planning is a particular case of the proposed method [41,63-65]. The advanced SFC toolpath developed in [61] combines the advantages of the iso-scallop method, boundary offset methods (complex pocket milling) and the grid navigation schemes.

The majority of the industrial part surfaces cannot be represented by a single parametric surface. There are many ways to represent a multi patch (compound) surface. The most popular is the NURBS representation [66]. Generating the toolpath for such surfaces is similar to the clustering methods presented earlier. The way to link the individual tool paths into a global tool path effects the machining time [7,20]. Optimization procedures for linking the NURBS patches have been presented in [67].

The trimmed surface is created from more than one solid objects combined and formed to become a designed surface, see Figure 1.4. The predefined parametric surfaces usually are subject to Boolean operation of trimming. However, the resultant intersection curves from the Boolean operations do not always coincide with the original curves when the surfaces are trimmed by one or more boundaries. It has been reported that the iso-parametric method might fail when applied to trimmed surfaces [68]. However, in the automotive or aerospace industries the toolpath generation must work for multi-patch surfaces. Surface re-parameterization methods enable generation of the entire toolpath [69,70]. For instance, Li [71] presents a boundary-conforming technique based on interpolation between the boundaries of the subregions to generate the toolpath for the entire surface. The proposed technique is close to the so called algebraic grid generation, see Figure 1.5.

Polyhedral models (also called faceted, tessellated or triangular mesh models) are becoming common in the manufacturing industry [68,72]. The STL (StereoLithography) format which approximates the surface of a solid model by triangles, is becoming the standard for the rapid prototyping industry and is increasingly popular in multi-axis manufacturing. The main reason is compactness, simplicity and applicability to an arbitrary surface.
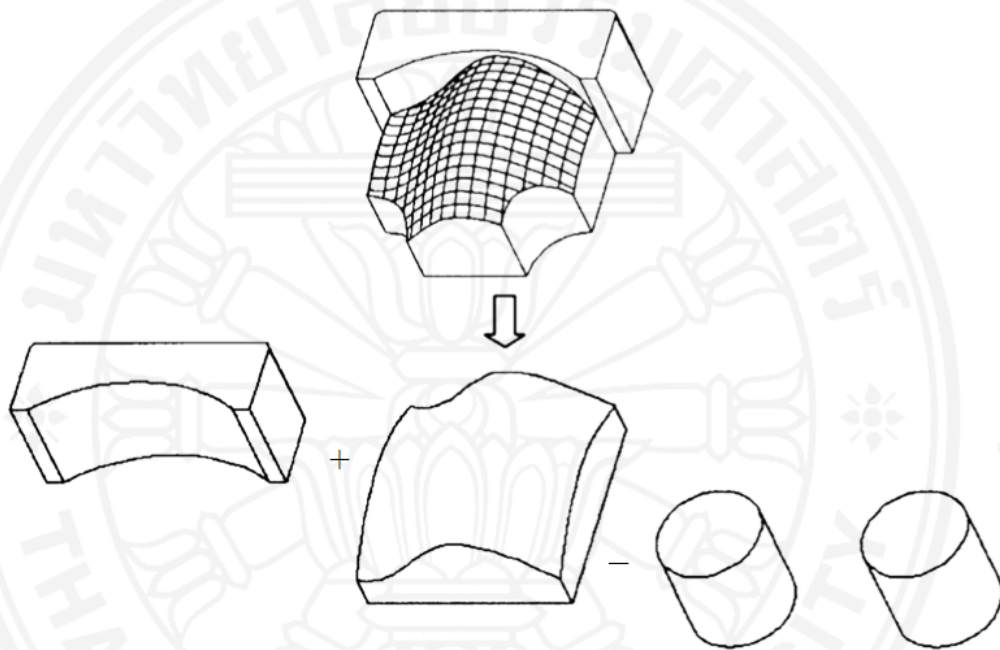


Figure 1.4: An example of trimmed surface created from a Boolean operation applied to multiple surfaces [69].

The tool path generation for precision machining of the polyhedral or STL part surfaces is becoming one of the most important problems of multi-axis machining. The main drawback is that the surface is no longer parametrized (the iso parametric path is not applicable). It is also often the case that the user does not know whether the STL file is correct, that is, whether it includes twisted or degenerated triangles.

The straightforward application of the iso-planar tool path to the STL surface is one of the most practical ideas. For instance Park [73,74] finds the intersection between lines and curves with an offset of triangular mesh model for 3-axis machining. The proposed method consists of two steps. First, obtaining intersection points by slicing the triangular-mesh surface with 2D plane and removing the unwanted intersection-

9

points by the polygonal chain intersection method [75]). Second, generating the toolpath is based on either line-projection (zigzag) or curve projection (contour) pattern.
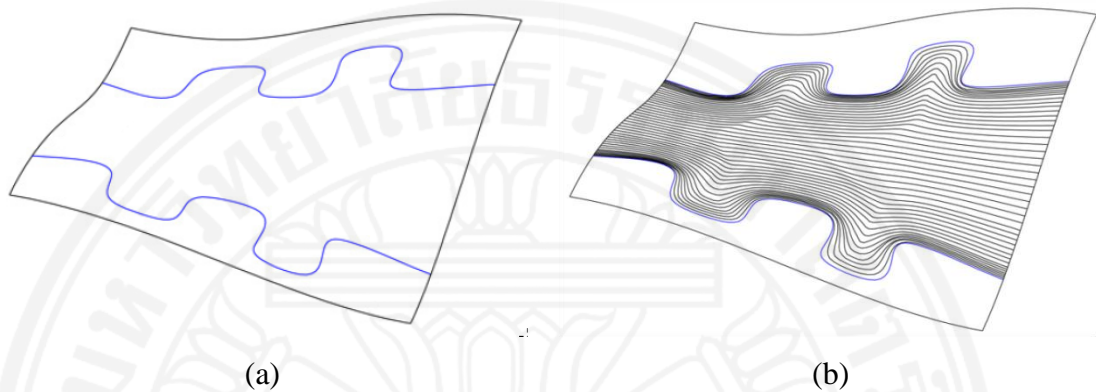


Figure 1.5: A demonstration of boundary-conformal toolpath generation [71] (a) surface with complex boundary edges (b) boundary conformal toolpath.

As far as 5 axis machining of the STL surfaces is concerned, the research on milling the STL files is limited. Xu et al. [76] developed a method for 5-axis machining with a flat-end and a fillet-end tool. The algorithm constructs the 2D C-space corresponding to the tool orientation using machine kinematic constraint parameters. Then a toolpath based on the iso-planar scheme is constructed by generating a series of points where the facet edges and the cutting plane intersect.

Lauwers et al. [77] presented a technique based on curvature matching for 5 axis polyhedral surface. Similarly, to the curvature matching of parametric surface, the cutter tilted angle is calculated based on the approximate normal vector at the CC point on triangle-mesh surface. Based on iso-planar technology, the parallel cutting planes get intersected with the meshed surface, obtaining a series of points for the toolpath generation.

An efficient greedy strategy to generate tool paths on triangular meshes, taking into account the machine kinematics, is presented by Zhang and Tang [78]. Starting from a given CC point, the next CC point is chosen to be the one which maximizes the feed rate limit at the current CC point while at the same time minimizing the cutting strip

10

overlaps. The method provides a toolpath with maximum feed rate based on the approximation of triangle surface curvatures. Through a greedy searching strategy, obtaining the sequence of CC points can be achieved by maximizing the feed rate under the given limit while minimizing the cutting strip overlaps iteratively. This process is repeated until all the mesh vertices are cut. However, the authors point out the main disadvantage of this method which is its disregard of the patterns and creating sharp turning curves. However, regular and uniform pattern of CC curves are always desired while the sharp turning curves should be avoided.

Xu et al [79] introduce a mapping-based approach for CNC machining on a meshed surface. The key feature is elimination of self-intersections. The algorithm consists of three steps. First, the surface is flattened onto a 2D plane using a mesh mapping technique [80]. Second, the offset paths are constructed in the 2D. At this stage, the intersection points are detected and eliminated. Finally, the tool path is mapped back onto the surface.

Many unconventional methods to tackle different criteria of the tool path optimization have been presented in the past few years. Aydin et al. [81] develops a toolpath generation method based on a genetic algorithm. The method optimizing several cost functions to link the CC points has been shown to be effective when optimizing time, straightness of the path and the cutter engagement. The problem of singularities of the 5 axis tool path, originally stated in [82] and analyzed in [83,84], was generalized in [85]. The method includes kinematics element modeling, assembling the elements and deriving the general inverse kinematic equations. Different kinematic configurations of a five-axis machine can be generally represented as a model of revolute joint, prismatic joint, workpiece or cutting tool. The singular points are avoided by deforming the tool orientation vectors interpolated by a 5-th degree B-spline in the quaternion space. The resulting toolpath is capable of avoiding singularity for a variety of the 5 axis configurations.

The method of iso-level has been presented [86]. The objective of the proposed method is global optimization combining the iso-scallop method and smoothing tool orientations (this algorithm used level-set method to generate toolpath).

The preferred feed direction (PFD) method has been proposed in [87]. The PFD is designed to maximize the cutting strip width. The PFD field is partitioned into the subregions by identifying the degenerate points and generating the separatrices. The resulting segmented regions are characterized by similar PFD's and iso-scallop tool paths are then generated for each region to mitigate redundant machining.

The force-minimal toolpath generation has been presented [88]. The method attempts to minimize the cutting force. The workpiece is mapped into small grids to determine the contact regions between the tool and the workpiece. The optimization includes the minimum-cost connection (MCC) function. The toolpath is constructed by propagating the initial MCC path inside the parametric region.

The goal of toolpath generation is to provide an optimal sequence of the CL-points for a particular milling machine. Selecting a suitable toolpath technology is a critical part and may produce various results depending on a particular operation. The evaluation criteria of toolpath generation are computation complexity, machining time, length of the tool path, kinematics error, robustness, applicability to a large family of surfaces, and compatibility with industrial formats. Although the above criteria of tool path quality are relatively simple, a unified approach applicable to an arbitrary surface on an arbitrary 5 axis machine does not exist.

### 1.1.2 Tool posture and gouging avoidance

Interferences during the machining lead to a decrease of the quality of the machined surface, possible damage and even collisions between different parts of the machine. The interferences are usually classified as the local gouging, rear gouging, and global collisions [89]. A set of CL points that free from all types of collisions called the accessibility map.

Local gouging refers to the removal of excess material in the vicinity of the CC point due to the curvature mismatch between the tool and the desired surface resulting in a greater than allowable tolerance. Rear gouging refers to the removal of excess material due to the intrusion of the cutter bottom surface into the part surface. Global

collisions occur when non-cutting parts (e.g., tool holder) of the cutting tool contact (crash) with the machining part or non-machining part, see Figure 1.6.

The term local millability implies that there is an area of the CC point such that the cutter and the part surface don't have a point in common in this area aside from the CC point. My et al. [90] express that "the local millability of a CC point relates to the local principal curvatures of the part surface, the cutter parameters and the tool orientation". If all axis positions pass through a fixed point and if all points of the workpiece surface can be seen from this point, then the local millability implies global millability [91].
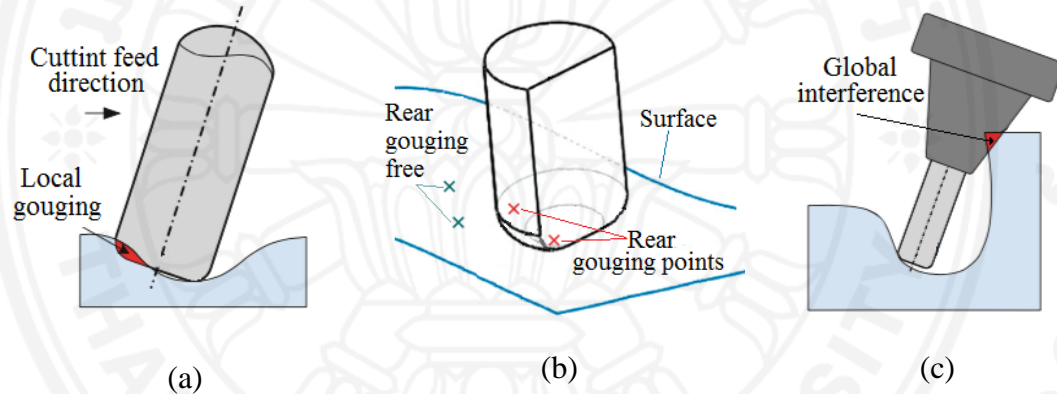


Figure 1.6: Demonstration of gougings (a) local gouging (b) rear gouging (c) global interference [89].

Incorrect tool posture may increase the machining time [76], decrease the machining quality and even leave visible tool marks on the part surface [92]. Tool positioning is particularly important when using the flat-end or a fillet-end mill. In five axis machining, a tool moving along the minimum curvature requires minimal inclination and therefore produces the maximum strip width [93]. However, the strip width depends on the difference between the surface main curvatures at the CC point. The techniques to maximize the machining strip by minimizing the inclination angle have been reported in [15,94,95].

Partitioning the surface into sub-surfaces and selection of the proper cutter to avoid gouging are presented [96]. The method classifies the part surface into concave,

convex and saddle-like regions. Using the flat-end tool for convex regions and the ball-nose tool for the others offers the overall increase of the material removal rate. However a significant disadvantage of the ball-end cutter is that the cutting speed differs along the tool radius. The maximum speed can be reached around the tool circumference being zero at the tool tip.

In [38] gouging avoidance can be achieved by tilting the cutting tool towards the feed direction. The inclination angle is obtained by matching the surface curvature and the effective cutting shape (also called the effective cutting curvature). The curvature of the effective cutting shape (also called effective cutting curvature) can be calculated in a plane normal to the tool path and along the tool path and compared to the surface normal curvature. The inclination angle is calculated as the maximum required by the two respective curvatures. C.C. Lo [97] improves this technique by continuously checking for gouging in every direction. The modification of this idea is also reported [59]. Furthermore, A. Rao and R. Sarma [98] introduce an exact method for local gouging detection and elimination in five axis machining when using a flat-end cutter. This method is based on the curvature of the cutting tool swept surface at any given CC point along the tool path. By sampling a finite set of points on the toolpath, local gouging is detected and eliminated.

It is pointed out by Z.Li and W. Chen [99] that more than one CC point needs to be taken into account in order to establish a correct tool position. The traditional method to obtain the cutter position generally focused on the cutter contact point using local differential geometry and, based only on the geometric properties, will not obtain the best cutter positions. Moreover, the single contact point technique does not guarantee the gouging free positions. This shortcoming is because of considering the geometric properties of the tool and the surface at just a single point and matching the curvature in a single plane or at selected set of planes. The authors define a cutter "virtual cutting edge" relative to the trajectory of the cutter. The trace is used to determine the "instantaneous cutter position error" which characterizes positioning of the cutter on the surface for every point of the path. The multipoint techniques could be used to further improve the accuracy of tool positioning [100,101]. In the multipoint matching method, the lead angle is calculated by taking into account that there are more than

one contact point between the tool and the desired surface. On the other hand, when the intersections are assessed, the numerical iterations may diverge. Also, the computational complexity of the multipoint strategy can be high and there is no absolute guarantee of a gouge-free position.

Jun et al. [102] propose a method based on rear, local and global gouging avoidance. Gray et al. [103] introduce the rolling ball method (RBM) to detect the rear gouging based on the approximation of the bottom tool shadow and a local surface curvature. The strategy is based on a ball having a varying radius rolling along the tool path and positioning the cutting tool inside the ball. The part surface being machined is approximated by a small region of the ball's surface.

P.J Gray et al. [72] propose an improvement of an arc-intersect method that compromises between the multipoint and the curvature matching methods. The tool is tilted towards a feed direction and its vector is constrained within the tilting plane. This allows finding the minimum tilt angle on the surface while the tool contacts the surface without gouging. A modification of this method is presented in [104].

Kim et al. [105] present a gouging-free tool orientation method which exploits hyper-osculating circles to approximate the surface and detect gouging. The author claims that the maximum matching between the tool and the part surface is achieved.

S.P Radzevich [106] detects a non-machinable region and subdivides the surface into several machinable subsurface regions. T.D. Tang et al. [107] presents a promising technique where the part surface and machine bodies are represented by an octree of bounding spheres. The collision is detected as the collision of the approximating spheres.

Even if gouging free positions have been established it does not ensure against global interference, e.g. the tool holder, the fixture or even the machine table can collide with the part surface or with another machine part leading to a damage of the surface, or even the machine itself.

G. Elber and E. Cohen [108] observe that "The problem of accessibly, or the ability to verify and possibly correct gouging into the machined surface or even into other surfaces, is apparently the most fundamental hindering factor in the broad use of five-axis machining.". Hence, the global millability at a point is characterized as the local millability consolidated with the absence of flank milling. Alternatively the global millability can be detected by advanced the solid modeling systems or CAD/CAM systems such as Vericut, UG, MasterCAM (see a recent survey [5]). The solid modeling is capable of recognizing the local interference, the global interference and collisions with the clamping device and machine parts. Therefore, current solid modeling research focuses on efficient and fast algorithms to compute the swept volume of the tool and perform Boolean operations to subtract the intersections from the stock [5].

The smoothness of the tool orientation usually increases the machining time as well as decreases the quality by leaving tool marks on the machined part [92]. The toolpath which includes sharp variations in the positions or orientations requires a decrease in the feed rate [109], thus, increasing the machining time.

The standard approach is the C-space technique where the tool is considered as a rigid body in the 6 dimensional space corresponding to its six degrees of freedom [110,111]. The conventional mathematical approach is smoothing spline interpolation. The local toolpath correction technique based on quintic and septic splines applied to smooth the tool orientations and achieve $C^3$ continuity has been presented [112]. The method includes inserting additional points and spline interpolation performed independently for tool positions and orientations. Bi et al. [113] present an algorithm for smoothing the toolpath for high speed five axis machining. The method calculates two discreet position segment junctions in terms of two cubic Bézier curves in the transition axis and the rotational axis. The dual cubic Bézier curves system has three advantages: (1) the feed speed and stability are improved because the dual-Bézier transition technique smooths the tool trajectory directly in machine coordinate system both the translation and rotational axis simultaneously, (2) the synchronization of parametrization of the translation and rotational can be achieved, and (3) the

analytical solution of the cubic-Bézier transition splines can be integrated in the real-time interpolator.

Castagnetti et al. [92] presents a smooth tool orientation technique based on the domain of admissible orientation (DOA). This approach consists of two stages. First, the domain of admissible orientations is determined in the workpiece coordinates. Then it is transformed into the machine coordinates system. At the second stage, the smooth transition of the tool axis orientations is achieved by minimizing the angular difference between the two successive points as well as the curvature of the tool trajectory.

Farouki et al. [114] present a method that minimizes the deviation between tool orientation and the surface normal to maintain a constant cutting speed with a ball-end tool which in turn to reduces an unnecessary actuation of the machine rotary axes.

Another perspective direction is optimization of the surface position and orientation on the worktable using the spherical indicatrix. The term spherical indicatrix refers to the Gauss maps of the designed surface and of the surface of the cutting device [115]. This characteristic curve detects whether the free-form surface is machinable. The idea, which is to evaluate the optimal surface orientation on the worktable, is presented in [116].

Pengcheng Hu and Kai Tang [117] present the optimization of the machine kinematic error algorithm based on workpiece setup optimization. Additionally, the optimal yaw angles of the tool are evaluated to reduce the maximal angular accelerations of the rotary axes.

Anotaipaiboon et al. introduce the initial worktable optimal setup for five axis machining to reduce the kinematic errors [118]. The proposed method employs the least square distance between the actual and the desired tool trajectories. The resulting nonlinear equations are solved by the Newton–Raphson method. The kinematics errors are claimed to be reduced as much as 99.9%.

There are many other parameters and processes that affect the efficiency and quality of the five axis machining such as machining feed rate [119-122], kinematics and dynamics of the CNC mechanisms [123,124], the cutting forces and tool deflections [125], thermal deformations [126-129] as well as the systematic errors [118,130]. Some other, less prominent but still important, sources of errors are machine operating conditions such as the material removal rate (feed rate), the depth of the cut, wet or dry cutting, clamping conditions, the tool wear and other tool imperfections [5]. However, the tool path generation methods and tool positioning strategies discussed above are the most relevant to the scope of this dissertation.

## 1.2 Dissertation Outlines

The dissertation is structured as follows. Chapter 2 introduces the background of five-axis machining. Chapter 3 presents the vector field aligned path (VFAP) algorithm. Chapter 4 describes the adaptive curvilinear toolpath (ACT) framework. Chapter 5 includes the conclusion and suggestions for future work. Finally, Chapter 6 discusses open problems.

## 1.3 Contributions

The contributions of this dissertation can be summarized as follow:

- development of vector field alignment path (VFAP) algorithm
- development of adaptive curvilinear toolpath (ACT) framework
- modification of biased space filling curve (BSFC)

# Chapter 2
# Basic Concepts of Five-Axis Machining

The idea of using data to control the machine-tool motion was introduced in 1947 by John Parsons when the US Air Force needed to develop an efficient manufacturing method to support modern aircraft production. In 1949, Parsons was awarded a US Air Force contract to build what was to become the first numerical control (NC) machine. Later, in 1952, the project was developed by the Massachusetts Institute of Technology (MIT). MIT demonstrated that simultaneous three-axis movements were possible using a laboratory built controller. The NC machines became available to the industry in 1955 [131]. Nowadays, the computer numerical control (CNC) machine is the industry standard.
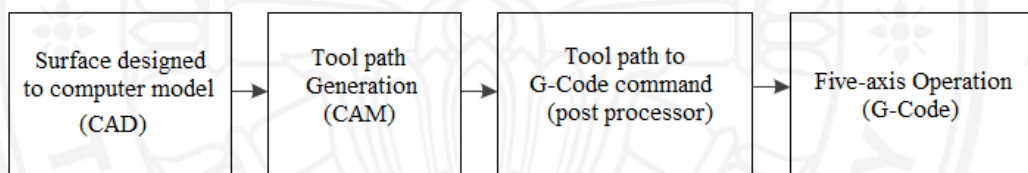


Figure 2.1: Five-axis machining concept

Many steps in the modern product design and manufacturing are automated by computer-aided design (CAD) and computer-aided manufacturing (CAM) software. The CAD software helps to design and translate a part surface (product) into a computer model. The CAM software processes the particular model to generate a tool path being converted into a G-code via an appropriate post-processor and then fetched into the CNC machine (Figure 2.1)

Multiaxis machining is a manufacturing process in which the tool moves in three, four, or five axes controlled by a computer. The terms multiaxis and five-axis are often used interchangeably. With a three-axis machine, the machine parts are produced by drilling, contouring and pocket milling routines, while rotating is performed occasionally by a rotary indexing mechanism. With the rotary axes machining of simple parts becomes straightforward. The benefits include elimination

of multiple set-ups, increased accuracy, and a better surface finish up [132] (Figure 2.2).

## 2.1 Introduction to Five-Axis Machining

Production of high accuracy parts and precision machining require high performance



Figure 2.2: Example of five-axis machine (HASS VF2TR Model)

NC machines. Five-axis machine are one of the possible solutions applicable to complex shaped surfaces required by a variety of industries such as aircraft, aerospace, optical equipment, medical devices and even jewelry. The machines have been used to cut, mill, grind and shape a variety of materials such as stainless steel for aerospace turbines, titanium for a valve block motor engine or ceramics for dental implants.

The machines include three translation axes and a pair of rotation axes. Theoretically, the five degrees of freedom are sufficient to position the tool and the workpiece in any position and under any angle relative to each other [1]. However, the machine limits and configurations provide different machining space. Therefore, the machine configuration is an important subject in the multiaxis machining theory.

On the very basic level, the machine kinematics is characterized by the axes that handle the table and the tool carrying axes. For instance, Figure 2.4 displays a kinematic diagram of the five axis machine in Figure 2.3; four axes handle the workpiece table while the tool is carried by one linear axis. Table 2.1 and Table 2.2 show the classification of 5-axis machines based on this criterion [8].

It should be noted that the classification above is important from the viewpoint of the corresponding inverse kinematics equations. Moreover, our classification is very basic. The extended classification of the 5 axis machines based on the theoretically possible combinations of the degrees of freedom is presented in [1]. Almost all five-axis machines have three translational and two rotational axis [1] due to the fact that this set up is the minimal combination providing an arbitrary position and orientation of the tool within the machine limits.

Finally, the classification of milling machines by ISO 841:2001 [133] standard is based on the relative position of the tool and the party and does not take into account the particular kinematics of the machine [134].

Furthermore, every machine is a compromise in one way or another. For example, the machine in Figure 2.5 has two rotary axes to carry the tool while the table can handle a heavy part. On the other hand, the two rotary axes on the table of the machine in Figure 2.3 might be a better option for small workpieces and complicated shapes. Matching a five-axis machine with a particular application is not an easy task. At present the selection of the machine configuration is performed based on the engineering experience and experiments.

(a)
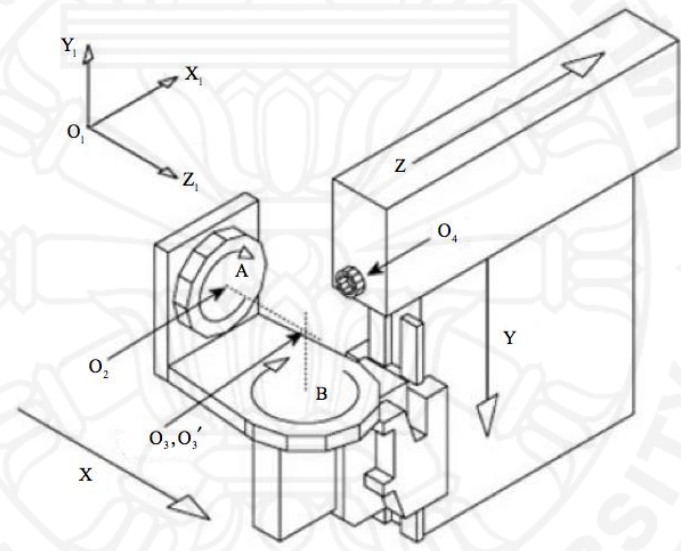


(b)
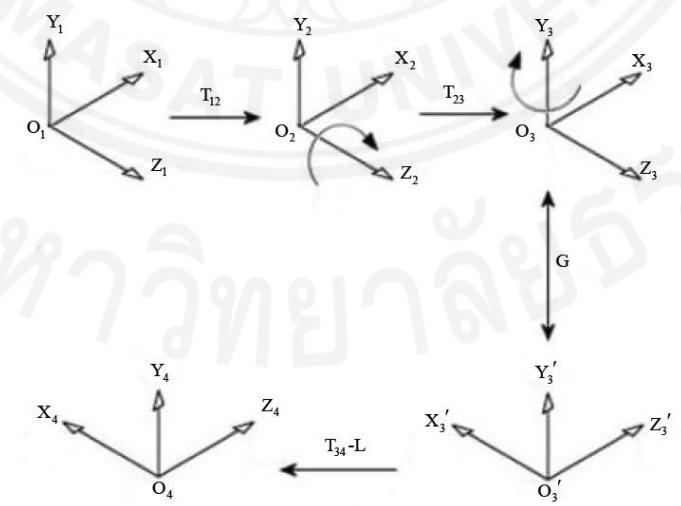


(c)

Figure 2.3: Machine kinematic (a) example of 2-0 machine and (b) the machine coordinate diagram (c) reference coordinate systems

Table 2.1: classification of five axis machines based on the rotary axis

| Type | Number of Table-axis | Number of Tool-axis | Description |
|------|---------------------|---------------------|-------------|
| 2-0  | 2                   | 0                   | Figure 2.3  |
| 1-1  | 1                   | 1                   | -           |
| 0-2  | 0                   | 2                   | Figure 2.5  |

Table 2.2: classification of five axis machines based on the number of axes carrying the table and the tool

| Type | Number of Table-axis | Number of Tool-axis | Description |
|------|---------------------|---------------------|-------------|
| 5-0  | 5                   | 0                   | -           |
| 4-1  | 4                   | 1                   | Figure 2.3  |
| 3-2  | 3                   | 2                   | -           |
| 2-3  | 2                   | 3                   | Figure 2.5  |
| 1-4  | 1                   | 4                   | -           |
| 0-5  | 0                   | 5                   | -           |
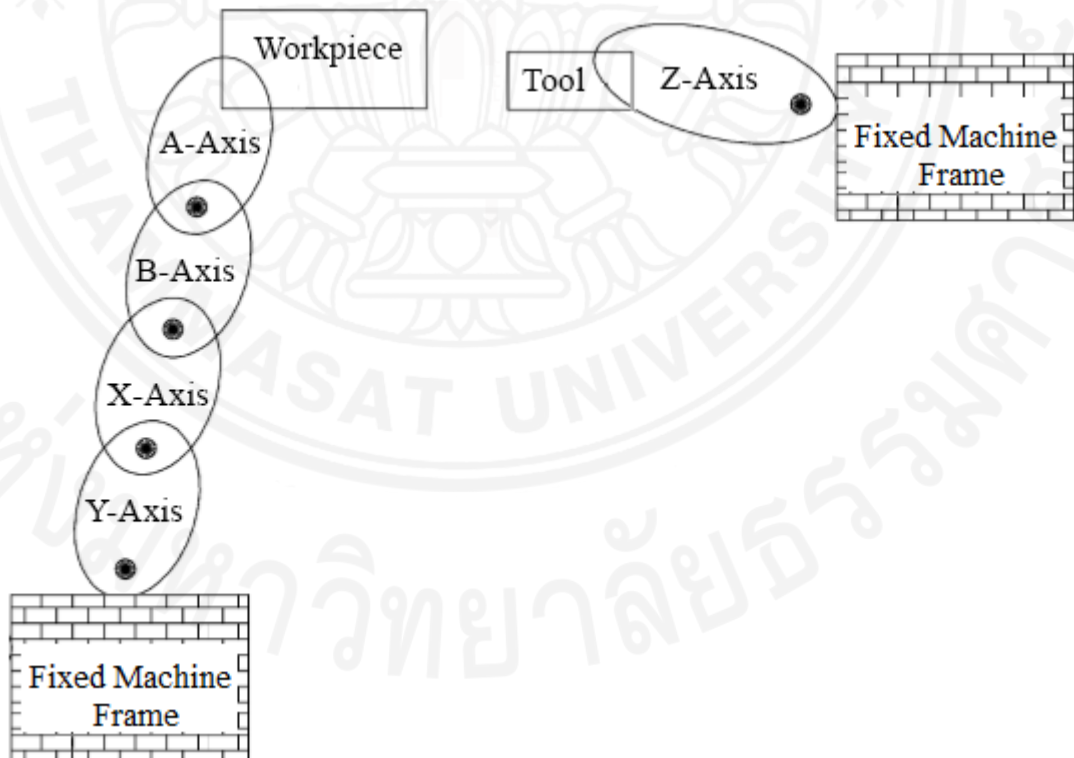
Figure 2.4: Kinematic chain representation of machine in Figure 2.3

(a)
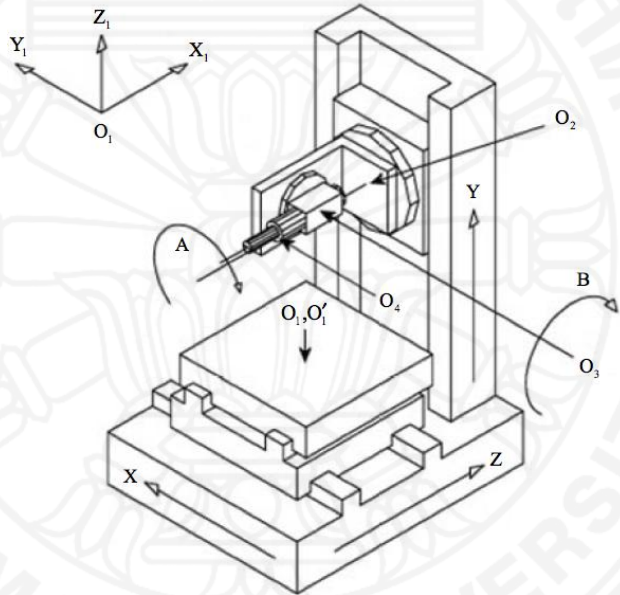


(b)
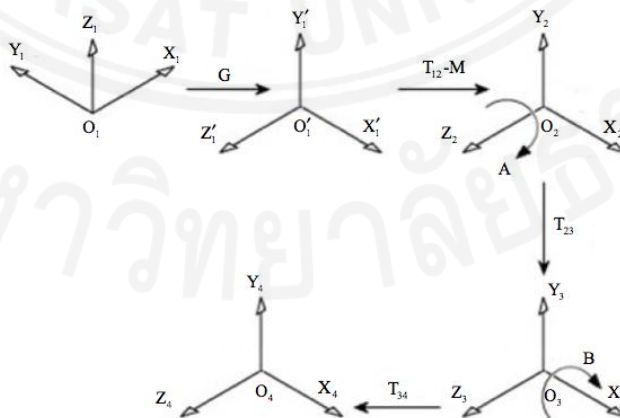


(c)

Figure 2.5: Machine kinematic (a) example of 0-2 machine and (b) the machine

24

## 2.2 Machine Kinematics

The machine kinematic can be interpreted as a transformation of the machine coordinates $M = (x_m, y_m, z_m)$ to the workpiece coordinates $W = (x_w, y_w, z_w)$. The transformation is required to program a post processor for the particular machine. The postprocessor translates the cutter location points (CL) in the workpiece coordinates into the machine coordinates (the inverse kinematics) and further into a G-Code. Below is an example of 2-0 five-axis machine kinematics. The equations are derived by introducing the coordinate systems shown in Figure 2.3 - Figure 2.5 where $A$ denotes the first rotary axis and $B$ the secondary axis [8].

- **Example of 2-0 Machine Kinematics Equation**

The kinematics equations are derived as follows:

Step 1: Coordinate translation $O_1 \rightarrow O_2$

$$C_2 = W + T_{12}, \tag{2.1}$$

where $T_{12}$ is the coordinate of the center of $O_1$ in $O_2$.

Step 2: Rotation around A-axis in $O_2$ by $a$

$$C_{2A} = A[a]C_2 = A[a](W + T_{12}), \tag{2.2}$$

where $A[a] = \begin{bmatrix} \cos a & \sin a & 0 \\ -\sin a & \cos a & 0 \\ 0 & 0 & 1 \end{bmatrix}$ is the rotation matrix around the $A$-axis.

Step 3: Coordinate translation $O_2 \rightarrow O_3$

$$C_3 = C_{2A} + T_{23} = A[a](W + T_{12}) + T_{23}, \tag{2.3}$$

where $T_{23}$ is the coordinate of the center of $O_2$ in $O_3$.

Step 4: Rotation around $B$-axis in $O_3$ by $b$

$$C_{3B} = B[b]C_3 = B[b](A[a](W + T_{12}) + T_{23}), \tag{2.4}$$

where $B[b] = \begin{bmatrix} \cos b & 0 & -\sin b \\ 0 & 1 & 0 \\ \sin b & 0 & \cos b \end{bmatrix}$ is the rotation matrix around the $B$-axis.

Step 5:  Coordinate rotation (axis alignment) $O_3 \rightarrow O_3'$

$$C_3' = GC_{3B} = GB[b]\big(A[a](W + T_{12}) + T_{23}\big), \tag{2.5}$$

where $G = \begin{bmatrix} 0 & 0 & -1 \\ 0 & 1 & 0 \\ 1 & 0 & 0 \end{bmatrix}$ is the alignment matrix.

Step 6:  Coordinate translation $O_3' \rightarrow O_4$ with machine slide translation $M$

$$C_4 = C_4' + T_{34} - M = GB[b]\big(A[a](W + T_{12}) + T_{23}\big) + T_{34} - M, \tag{2.6}$$

where $T_{34}$ is the coordinate of $O_3'$ in $O_4$ with respect to the machine zero point

$M = (0,0,0)$.

Equating $C_4$ and $T_4$ yields

$$T_4 = C_4 = GB[b]\big(A[a](W + T_{12}) + T_{23}\big) + T_{34} - M. \tag{2.7}$$

After rearrangement,

$$\begin{aligned} M &= GB[b]\big(A[a](W + T_{12}) + T_{23}\big) + T_{34} - T_4, \\ W &= A^{-1}[a]\big(B^{-1}[b]G^{-1}(M - T_{34} + T_4) - T_{23}\big) - T_{12}, \end{aligned} \tag{2.8}$$

where $T_4 = (0,0,-L)$ is the coordinate of the tool tip in $O_4$ and $L$ is the tool length.

Let $T_1'$ be the coordinate of $T_4' = (0,0,-L+1)$ in $O_1$ and is given by

$$T_1' = A^{-1}[a]\big(B^{-1}[b]G^{-1}(M - T_{34} + T_4') - T_{23}\big) - T_{12}. \tag{2.9}$$

The relationship between the tool orientation $I = (I_x, I_y, I_z)$ and the rotation angles, $a$ and $b$, is then given by

$$I = T_1' - W = A^{-1}[a]B^{-1}[b]G^{-1}(T_4' - T_4) = \begin{bmatrix} \cos(a)\cos(b) \\ \sin(a)\cos(b) \\ -\sin(b) \end{bmatrix}. \tag{2.10}$$

26

Inverting with regard to $a$ and $b$ yields

$$a = \begin{cases} \tan^{-1}\left(\dfrac{I_y}{I_x}\right) & \text{if } I_x < 0 \text{ and } I_y \geq 0, \\[2mm] \tan^{-1}\left(\dfrac{I_y}{I_x}\right) + \pi & \text{if } I_x < 0, \\[2mm] \tan^{-1}\left(\dfrac{I_y}{I_x}\right) + 2\pi & \text{otherwise,} \end{cases}$$

$$b = -\sin^{-1} I_z.$$

(2.11)

For 1-1 and 0-2 machines, kinematics equations can be obtained using the same methodology (see [8] for details).

The kinematic error, if the tool path is fixed, depends only on the configuration the particular machine. Note that five-axis machines generate non-linear trajectories, which depend on the configuration and the set-up. This makes the kinematic error difficult to evaluate. Ibaraki et al. [135] propose a set of machining tests for a five-axis machine tool to identify and isolate its kinematic errors from other kind of errors. Wang, Hu, and Zan [136] apply the homogeneous transformation matrix method to establish the kinematic error model of five-axis machining tool with two-axis turntable and propose a method for separating the kinematic error. Tsutsumi et al. [137] describe methods of measuring and correcting the geometric deviations inherent to the five-axis machine that result in reducing kinematic error. Tutunea-Fatan and Bhuiya [138] introduce non-linearity error as a method to quantify the kinematic efficiency of a particular five-axis machine configuration.

Note that as compared to the conventional three-axis machines, the additional rotary axes could be the reason of a variety of degrading effects. The additional axes introduce an additional mass which reduces the maximum attainable speed and acceleration and could have a negative impact on the dynamics of the machine, the stability and other critical parameters. The rotary axes are typically slower than the Cartesian (linear) axes, therefore, they can slow down the entire operation. More importantly, the rotational joints change the stability conditions of the cutting operations (the natural frequencies of the system) which may lead to an unexpected

27

chatter (self-excited vibrations) and unwanted waviness of the part surface. Even under stable, chatter free conditions, the tool is subjected to periodic forced vibrations leading to overcuts or undercuts. These effects may amount to as much as 75% of all the errors [139].

Furthermore, the tool deflection errors are one of the most prominent [140]. Milling a complex shape may be affected by deflections of the end mills caused by variation of the cutting forces, especially when a corner cutting (complex pocket milling) is involved [141,142]. The end milling force and deflection depend on the tool path, tool geometry, cutting conditions and the material properties [143,144]. Although it is difficult to entirely eliminate these errors, a considerable reduction can be achieved by various compensating strategies [145]. Finally, there are thermal deformations which may add up in the five-axis case (see studies of the thermal effects for the five-axis configurations including high-speed micro-milling [126-129,146,147]).

As far as the accuracy-related geometric errors are concerned, they can be attributed to three main types. The first type is 5 related to the kinematics of the machine [148] and includes the systematic errors [130] and errors attributed to the initial set-up [118]. The machines with three linear axes have a total of 21 linear independent geometric error components [149], whereas the five-axis milling machine has 42 components (twice of the three-axis machine!) [150]. The second source is the imperfection of the movements the machine components and its fixtures [151,152].

Finally, an important source of the geometric errors is inaccurate tool positioning which leads to a curvature interference and gouging (see, for instance, survey by Makhanov [5]). In many cases, this type of error is unavoidable but can be considerably reduced.

Some other, less prominent but still important, sources of errors are: machine operating conditions such as the material removal rate (feed rate), the depth of the cut, wet or dry cutting, clamping conditions, the tool wear and other tool imperfections [5].

## 2.3 Surface Geometry

The free-form surfaces in manufacturing industries are characterized by complex geometries and variable curvatures. Many of these surfaces can be represented as collections of patches each of which is a parametric surface.

Consider a parametric surface $S \equiv S(u,v)$ where $u$ and $v$ are the parametric coordinates. The most important geometric characteristics of the surfaces are given below [8,38,39].

The unit normal vector $\mathbf{n}$:

$$\mathbf{n} = \frac{S_u \times S_v}{\left|S_u \times S_v\right|} \tag{2.12}$$

The first fundamental form (or line element), $\mathbf{I}$ :

$$
\begin{aligned}
\mathbf{I} &= dS \cdot dS, \\
&= \left(S_u du + S_v du\right) \cdot \left(S_u du + S_v du\right) \\
&= S_u \cdot S_u du^2 + 2S_u \cdot S_v dudv + S_v dv^2, \\
&= Edu^2 + 2Fdudv + Gdv^2,
\end{aligned} \tag{2.13}
$$

where

$$
\begin{aligned}
E &= S_u \cdot S_u, \\
F &= S_u \cdot S_v, \\
G &= S_v \cdot S_v.
\end{aligned} \tag{2.14}
$$

The second fundamental form, $\mathbf{II}$ :

$$
\begin{aligned}
\mathbf{II} &= -d\mathbf{n} \cdot dS, \\
&= -\left(\mathbf{n}_u d_u + \mathbf{n}_v d_v\right) \cdot \left(S_u d_u + S_v d_v\right), \\
&= -\mathbf{n}_u \cdot S_u du^2 - \left(\mathbf{n}_u \cdot S_v + \mathbf{n}_v \cdot S_u\right) dudv - \mathbf{n}_v \cdot S_v dv^2, \\
&= \mathbf{n} \cdot S_{uu} d_u{}^2 + \mathbf{n} \cdot S_{uv} + \mathbf{n} \cdot S_{uv} + \mathbf{n} \cdot S_{vv} d_v{}^2, \\
&= \mathbf{n} \cdot S_{uu} du^2 + 2\mathbf{n} \cdot S_{uv} dudv + \mathbf{n} \cdot S_{vv} dv^2, \\
&= edu^2 + 2fdudv + gdv^2,
\end{aligned} \tag{2.15}
$$

where

29

$$
\begin{aligned}
e &= \mathbf{n} \cdot S_{uu}, \\
f &= \mathbf{n} \cdot S_{uv}, \\
g &= \mathbf{n} \cdot S_{vv}.
\end{aligned}
\tag{2.16}
$$

The normal curvature of $S$ in the direction $\mathrm{v} = aS_u + bS_v$, is given by

$$
k(\mathrm{v}) = \frac{ea^2 + 2fab + gb^2}{Ea^2 + 2Fab + Gb^2}.
\tag{2.17}
$$

The principle curvatures, which are the maximum and minimum of the normal curvature, are given by

$$
\begin{aligned}
k_{\max} &= H + \sqrt{H^2 - K}, \\
k_{\min} &= H - \sqrt{H^2 + K}.
\end{aligned}
\tag{2.18}
$$

where $K$ and $H$ are the Gaussian curvature and mean curvature, respectively, and are given by

$$
\begin{aligned}
K &= \frac{eg - f^2}{EG - F^2} = k_{\min} k_{\max}, \\
H &= \frac{eG - 2fF + gE}{2(EG - F^2)} = \frac{1}{2}(k_{\max} + k_{\min}).
\end{aligned}
\tag{2.19}
$$

The direction $\mathrm{v} = aS_u + bS_v$ associated with a principle curvature, $k$, is computed using the relations

$$
\begin{aligned}
(e - kE)a + (f - kF)b &= 0, \\
(f - kF)a + (g - kG)b &= 0.
\end{aligned}
\tag{2.20}
$$

The surface points are classified into six different types, depending on the values of $K$ and $H$ as shown in the following.

- Concave elliptic point If $K > 0$ and $H > 0$, the surface lies entirely on the surface normal side $(\mathbf{n})$ of the tangent plane in its neighborhood. Both the principal curvatures are positive.

30

- Convex elliptic point If $K > 0$ and $H < 0$, the surface lies entirely on the opposite side $(-\mathbf{n})$ of the tangent plane in its neighborhood. Both the principal curvatures are negative.

- Hyperbolic point If $K < 0$, the surface lies entirely on both sides of the tangent plane in its neighborhood. Both the principal curvatures have different signs.

- Concave parabolic point If $K > 0$ and $H = 0$, the surface lies entirely on the surface normal side $(\mathbf{n})$ of the tangent plane in its neighborhood. One of the principal curvatures is positive and one is zero.

- Convex parabolic point If $K = 0$ and $H < 0$, the surface lies entirely on the opposite side $(-\mathbf{n})$ of the tangent plane in its neighborhood. One of the principal curvatures is negative and one is zero.

Planar umbilical point If $K = 0$ and $H = 0$, the surface lines entirely on the tangent plane in its neighborhood.

The ability to decompose the surface into different clusters enables us to efficiently plan the machining operations [41]. On the other hand, the surface clusters can be used to find the optimal set of tools for a particular surface [38]. For instance, convex and planar regions can be machined without gouging while this must be taken into account when machining the concave regions. A flat-end cutter can be applied to relatively flat regions without an inclination (maximum machining strip) while the concave areas must be machined by an inclined cutter to avoid the gouging.

Another possibility is defining optimal cutting directions using the vector field obtained from the surface by maximizing the cutting strip width or by minimizing the machining time [60]. The latter idea is the main subject of this dissertation.

# Chapter 3
## Vector Field Aligned Paths

Let us consider a part surface, discretize it and at every point evaluate a direction (vector) of the maximum material removal rate. The collection of the vectors constitutes a vector field defined in the parametric coordinates. We will call a tool path which visits every point, follows the desired vector field at every point and does not self-intersect, the optimal tool path. Constructing such a tool path is a difficult task. First attempts to optimize the tool path relative to a certain vector field of the optimal directions are the non-isoparametric tool paths [153,154] and the iso-scallop tool path proposed by [2]. The tool path is generated by an adaptive offsetting an initial curve (usually a boundary) so that the maximum machining strip or maximum allowable scallop height constraint is satisfied. For instance, the iso-scallop algorithm searches for a set of points which lies next to the initial curve and satisfies the scallop constraint. The resulting set of points is then connected to generate the next track of the tool.

An efficient algorithm to find a suboptimal solution of the tool path aligned with the vector field is presented in [32]. The entire surface is discretized using a rectangular grid in the parametric space and then covered by potential machining patches each characterized by one or several optimal directions producing the maximum machining strip (see Figure 3.1).

The method requires an "initial path" which has the largest average machining strip. The entire tool path is constructed by offsetting the initial path and propagating the offsets inside the region. The offset tracks are modified if they substantially deviate from the streamlines of the optimal directions. In other words, at some point the algorithm generates a new initial track.

Unfortunately, many surfaces produce a complicated, non-uniform vector field and although the above algorithm allows one to decompose the surface into sub-surfaces, the decomposition is not very well motivated from the optimization viewpoint. In particular, after the first propagation step, the algorithm searches for a new "initial
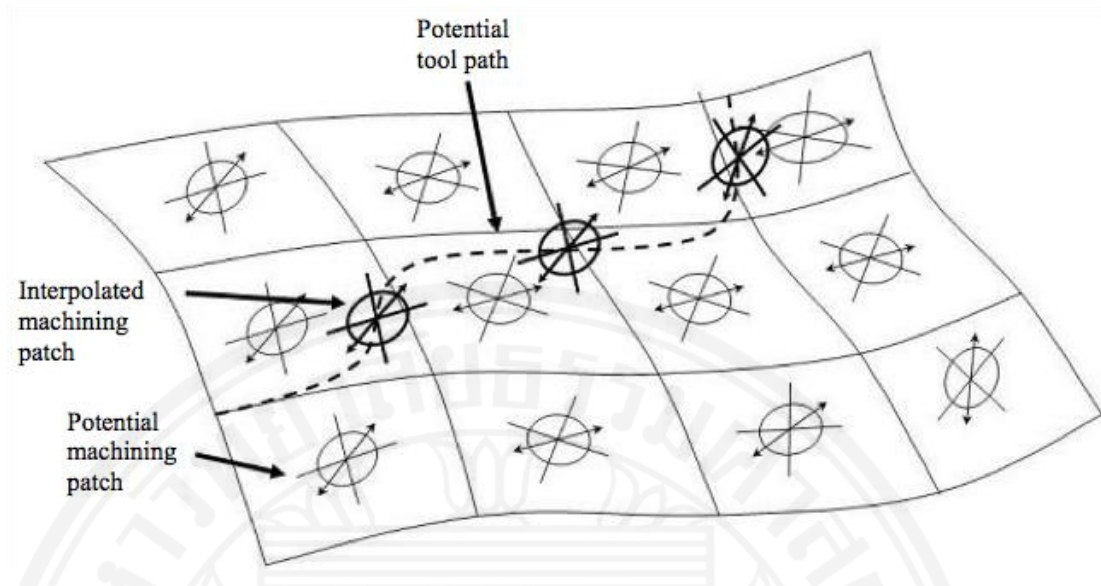
Figure 3.1: Potential vector field

tool path" such that the ratio between the length of the path and the average machining strip is less than a certain threshold. It is not hard to show that such analysis is not always accurate from the viewpoint of global optimization. It may also be sensitive to local variations of the optimization criteria. Moreover, finding the initial tool path is a computationally expensive, NP hard problem. For instance, if the parametric domain is rectangular (the simplest case), taking each side of the rectangle as the initial track generates four entirely different tool paths. Finally, additional efforts must be made to ensure that the resulting tool path is structured; that is, it becomes a zigzag or spiral.

The vector field of the optimal tool directions to capture the "skeletal" information of tool path (or a family of a tool paths) can be combined with the geometric constraints, evaluation of the kinematics performance of the machine and other constraints such as the cutting force limits [155,156]. However, the solutions of such problems are still purely heuristic due to the high computational complexity.

The surface can be partitioned into clusters so that the streamlines of the vector field are close to the conventional zigzag or spiral [41]. The advantage of this approach is that within a cluster the tool follows a nearly optimal path. Clustering optimizes the global criteria of the decomposition and makes it possible not only to decompose the surface but also to recognize similarities to the conventional tool path patterns.

Although an appropriate linking of the clusters can be performed [24], a complicated vector field often produces too many clusters otherwise the tool directions are far from the optimal. Besides, the partition requires tool withdrawals which increase the machining time. More importantly, the surface smoothness at the boundaries can be jeopardized.

Finally, following the optimal or nearly optimal directions can be combined with rear gouging, global gouging and machine limits constraints. For instance, the accessibility map [157] composed of the admissible ranges of the inclination, yaw angles is combined with a smoothness map measured by the derivatives of the tool vectors evaluated at the prescribed cutter location points. The two maps are employed by a path propagation algorithm similar to [32]. However, the algorithm also requires an initial track. Besides, the smoothness map [157] is not efficient from the kinematics error viewpoint. For instance, the stationary points of the surface may invoke large variations of the rotation angles [82] and large kinematic errors; however, the smoothness map does not take into account this effect.

### 3.1 Material Removal Rate

Let $W_1$ be an arbitrary CC (cutter contact) point on the surface (see Figure 3.2). Consider a set of points on the surface defined by $\Omega_{W_1} = \{W : dist_S(W_1, W) = l_1\}$, where $dist_S$ is the geodesic distance and $l_1$ is a small prescribed step (see Figure 3.2(a)). The corresponding set of points in the machine coordinates is denoted by $\Omega_{M_1}$. The distance between the corresponding points is given by $l_{1,M} \equiv l_{1,M}(W)$. The machining strip corresponding to the feed direction $\overrightarrow{W_1,W}$ is denoted by $w_1 \equiv w_1(W)$. Figure 3.2(b) exemplifies $\Omega_{W_1}$ and $\Omega_{M_1}$ for a surface depicted in Figure 3.2(a) obtained by the inverse kinematic transformations of HAAS VF2TR (Figure 2.2-Figure 2.3). Note that $\Omega_{W_1}$ is approximately a circle, whereas $\Omega_{M_1}$ is an irregular, ellipse-shaped, closed curve. Clearly, equal increments on the surface (in the workpiece coordinate system) do not lead to equal increments in the machine coordinates. Therefore, the machining

34

time depends critically on the translations in the machine coordinates rather than in the workpiece coordinates.

Furthermore, introduce an instantaneous material removal rate in the direction $\overrightarrow{W_1,W}$ given by $R_M(W) = \dfrac{F\, l_1(W) w_1(W)}{l_{1,M}}$, where $F$ is the feed rate. The machining strip $w_1$ corresponding to the prescribed feed direction is evaluated by locating the intersections of the effective cutting shape and the design surface (see [59] for details).

Note that the machining strip depends on the shape of the tool (ball nose, flat end, toroidal end mill, etc.) and its inclination. For instance, the flat end tool must be inclined to avoid gouging and curvature interference. Therefore, $R_M(W)$ includes the tool shape and inclination. Since the type of the tool and the tool vector are implicitly included, the algorithm works for any type of the tool and any strategy to avoid gouging and the curvature interference.

We will call the direction $\overrightarrow{W_1,W_2}$ optimal, if $W_2 = \underset{W \in \Omega_{W_1}}{\arg\max}\, R_M(W)$. In other words, $W_2$ maximizes the material removal rate. Evaluating vectors $\overrightarrow{W_1,W_2}$ for each surface point and transferring them into the parametric domain $(u,v)$ generates the vector field $V(u,v) \equiv (v_x(u,v), v_y(u,v))$.

Note that the rotation angles are also implicitly involved in the maximization of $R_M$ as follows. Let us assume that the controller performs the standard linear interpolation. The tool speed at a CC point along $\overrightarrow{W_1,W_2}$ is equal to the prescribed feed rate $F$. Note that these assumptions are not always realistic; however, one can replace the feed rate $F$ by the magnitude of the actual velocity vector and use the evaluation given below without any further modifications.

The time required to move from $W_1$ to $W$ is given by $t_1 = \dfrac{l_{1,M}(W)}{F}$. Consider the rotation angles $(a_1, b_1)$ and $(a, b)$ at $W_1$ and $W$, respectively. The required angular speed is given by $v_a = \dfrac{a_1 - a}{t_1}$. Furthermore, if $v_a > v_{a,\max}$, where $v_{a,\max}$ is the maximum allowable rotational speed, we re-evaluate the material removal rate as follows: $R_M \equiv R_M(W) = \dfrac{l_1(W) w_1(W)}{t_{new}}$, where $t_{new} = \dfrac{a_1 - a}{v_{a,\max}}$. A similar evaluation must be performed with regard to the second rotation angle $b$. The maximum allowed speed is evaluated from the cutting conditions and the material properties. The maximum cutting speed in the air is always given in the specifications of a 5 axis machine.
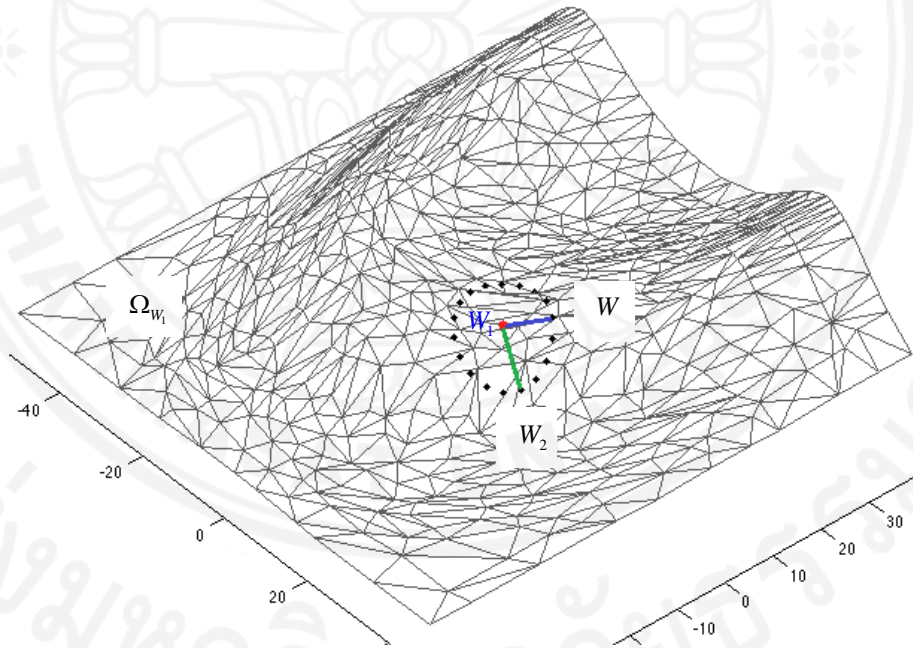


(a) possible directions in the workpiece coordinates

36
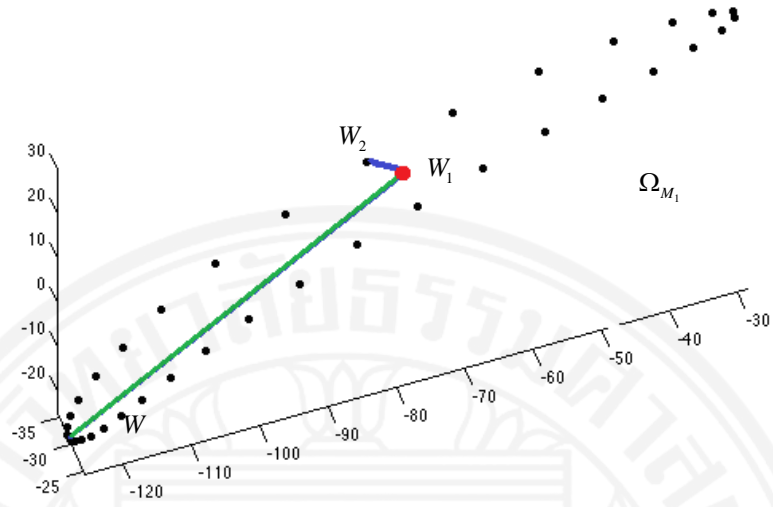
(b) possible directions in the machine coordinates

Figure 3.2: Possible tool feed directions in the workpiece and the machine coordinates

In order to reduce the machining time we maximize the cost function $R_M(W)$ and generate the vector field of the optimal directions based on that particular but important criterion. For each $(u_1, v_1)$ from the parametric domain $K$ we find $W_1 = S(u_1, v_1)$ and $W_2 = \arg\max_{W \in \Omega_{W_1}} R_M(W)$ (some advanced optimization methods can be applied to find $W_2$, however, this subject is beyond the scope of the paper). Note that a variety of other cost functions related to the machine kinematics can be used to produce the required vector fields.

- **The total length of the tool path in the workpiece coordinates**

As noted, this criterion does not minimize the machining time. Although in many cases it reduces the time, it is not as efficient as the proposed maximization of the material removal rate. The main advantage of this option is that it is machine independent. It is also independent with regard to the position and orientation of the workpiece on the table. The criterion is useful when the user is concerned about the tool wear (expensive tools for micro milling or high speed milling). The strategy to minimize the tool path in the workpiece coordinates is often based on maximization of the machining strip (see for instance [32]).

- **The total length of the tool path in the machine coordinates**

This criterion can be also applied to minimize the machining time. It is often very efficient; however, it does not include the rotation angles. Therefore, the minimal tool path in the machine coordinates still does not mean a minimum time. More often than not, the direction of the minimal distance in the machine coordinates does not follow the direction of the maximum machining strip.

- **The kinematic error**

This optimization can be combined with the minimization of the machining time, for instance with the minimization of the material removal rate. In this paper we apply a very basic approach based on additional CC points to keep the kinematic error within the prescribed tolerance. A more sophisticated version of such minimization can be found in [158].

- **The total angle variation**

This criterion can be applied to minimize the kinematic error which is invoked by the sharp rotations [8]. Minimizing the angle variation is less computationally expensive than minimizing the kinematic error explicitly [8,41].

### 3.2 Grid Generation

Let $S(u,v) \equiv (x(u,v), y(u,v), z(u,v))$ be the required part surface, where $u$ and $v$ are the parametric variables. We arrange the cutter location (CC) points $\{(u_{i,j}, v_{i,j}), 0 \leq i \leq N_\xi \ \ 0 \leq j \leq N_\eta\}$ as a curvilinear grid in the parametric domain $(u,v)$. Mathematically, it means that the CC points are the discrete analogy of a mapping from the computational region $\Delta = \{0 \leq \xi \leq N_\xi, 0 \leq \eta \leq N_\eta\}$ onto a parametric region defined in the parametric coordinates $u$, $v$. In other words, there exists a pair of functions $\{u(\xi,\eta), v(\xi,\eta)\}$ such that the rectangular grid [83] being fed to $\{u(\xi,\eta), v(\xi,\eta)\}$ becomes $\{u_{i,j}, v_{i,j}\}$ (see Figure 3.3).
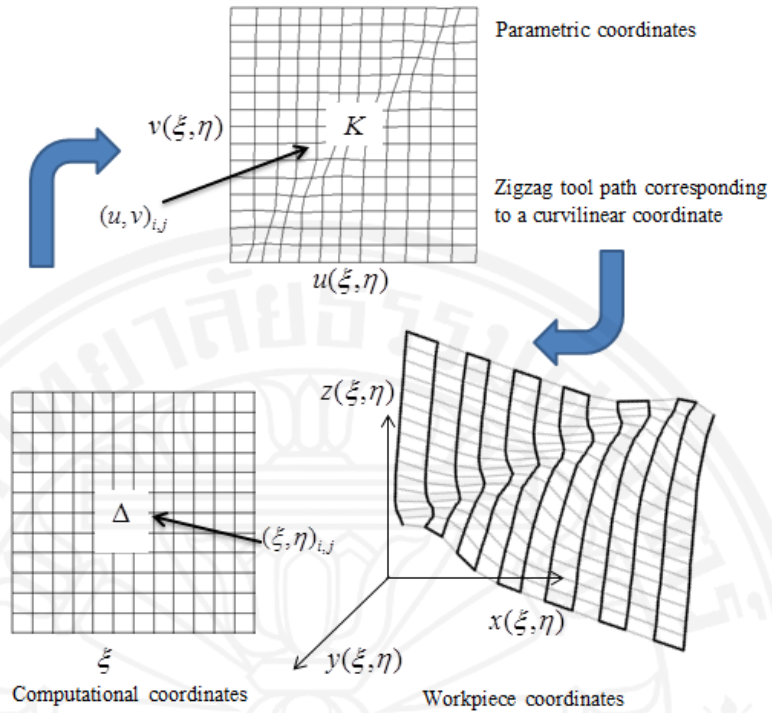
Figure 3.3: Coordinate transformations and the curvilinear grids, $\Delta$ denotes the computational domain, K the parametric domain

The required vector field $V(u,v)$ is partitioned into two vector fields $(\alpha(u,v), \beta(u,v))$ (the dual vector field) corresponding to the $\xi$ and $\eta$ directions as follows:

$$\beta(u,v) = \begin{cases} V(u,v) \in \Omega_\eta, \\ 0, \text{otherwise}, \end{cases} \tag{3.1}$$

where $\Omega_\xi, \Omega_\eta$ are prescribed subsets of the vector field $V(u,v)$ selected according to a certain criteria. For instance, if the vector field has two major directions (Figure 3.4) $d_\xi$ and $d_\eta$, the partition is performed as follows:

(a) $V(u,v)$        (b) $\alpha(u,v)$        (c) $\beta(u,v)$
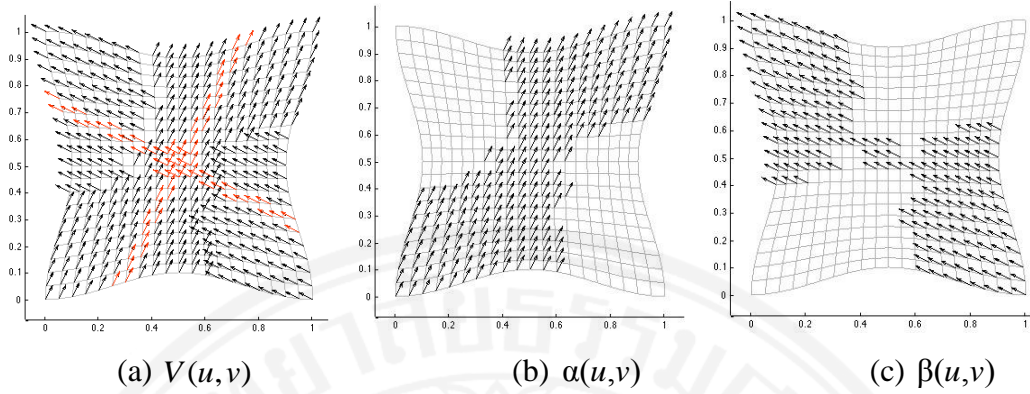
Figure 3.4: Partition of the vector field $V(u,v)$ into $(\alpha(u,v),\beta(u,v))$

$$\alpha(u,v) = \begin{cases} \measuredangle(V,d_\xi) \approx 0 \text{ or } \measuredangle(V,d_\xi) \approx \pi, \\ 0, \quad \text{otherwise,} \end{cases}$$

$$\beta(u,v) = \begin{cases} \measuredangle(V,d_\eta) \approx 0 \text{ or } \measuredangle(V,d_\eta) \approx \pi \\ 0, \quad \text{otherwise.} \end{cases}$$
(3.2)

In other words, the vectors $V(u,v)$ are included into the dual vector field $(\alpha(u,v),\beta(u,v))$ if they are almost parallel or almost anti-parallel to $d_\xi$ or $d_\eta$. Mathematically, it means that $\left\| \dfrac{(V,d)}{\|V\|\|d\|} \right| - 1 \right| \leq \varepsilon_V$, where $\varepsilon_V$ is the prescribed threshold.

For vector fields with regular geometry it is often sufficient to align only one family of grid curves. In this case $\alpha(u,v)$ is a subset of $V(u,v)$, whereas $\beta(u,v) = 0$. The vector field $(\alpha(u,v),\beta(u,v))$ can be further simplified. For instance, a point $(u,v)$ can be considered "important", if the optimal direction substantially reduces the machining time, otherwise $\alpha(u,v) = \beta(u,v) = 0$.

Furthermore, the curvilinear grid $\{u(\xi,\eta),v(\xi,\eta)\}$ is aligned with the dual vector field $(\alpha(u,v),\beta(u,v))$ using a modification of classical grid generation methods [159-161].

40

The smoothness of the grid is represented by a functional given by

$$F_S = \iint u_\xi^2 + u_\eta^2 + v_\xi^2 + v_\eta^2 \, d\xi d\eta \tag{3.3}$$

where subscripts denote the partial derivatives.

Note that $F_s$ is a classical variational functional providing smoothness of the mapping $\{u(\xi,\eta), v(\xi,\eta)\}$ [160,162]. Originally, the functional was applied to the tool path generation in [63]. The corresponding Euler equations for (3.3) are Laplacians able to offset the boundary due to their smoothing property. For example, if the boundary of the parametric region is a rectangle, functional (3.3) generates a rectangular grid corresponding to the conventional zigzag tool path. Furthermore, we show that a combination of the smoothness functional $F_S$ and the vector field alignment generates the required curvilinear tool path.

For simplicity, consider alignment of the grid lines $\eta$=const with a vector field $\alpha(\xi,\eta) \equiv (\alpha_1(\xi,\eta), \alpha_2(\xi,\eta))$. The alignment is provided by a functional given by

$$F_A = \iint (s_\xi \alpha')^2 \, d\xi d\eta, \tag{3.4}$$

where $\alpha'(\xi,\eta) \equiv (\alpha_1', \alpha_2') = (-\alpha_2, \alpha_1)$ is the vector field perpendicular to $\alpha(\xi,\eta)$ and $s_\xi = (u_\xi, v_\xi)$ is the tangent to the grid line $\eta$=const. If $s_\xi$ is parallel or antiparallel to $\alpha$, then $F_A = 0$. Following [160], the functionals $F_S$ and $F_A$ are combined linearly as follows: $\Phi = F_S + \lambda F_A$, where $\lambda$ is the weighting coefficient.

The corresponding Euler equations are

$$\Phi_u - \Phi_{\xi,u_\xi} - \Phi_{\eta,u_\eta} = 0, \tag{3.5}$$

$$\Phi_v - \Phi_{\xi,v_\xi} - \Phi_{\eta,v_\eta} = 0.$$

Substitution $s_\xi \alpha' = u_\xi \alpha_1' + v_\xi \alpha_2'$ and differentiation yields

$$u_{\xi\xi} + u_{\eta\eta} + 2\lambda[\alpha_1'(\alpha_1' u_\xi + \alpha_2' v_\xi)]_\xi = 0, \tag{3.6}$$

$$v_{\xi\xi} + v_{\eta\eta} + 2\lambda[\alpha_2'(\alpha_1' u_\xi + \alpha_2' v_\xi)]_\xi = 0.$$

Let us introduce a vector field $\beta(\xi,\eta) = (\beta_1(\xi,\eta), \beta_2(\xi,\eta))$ to be aligned with $s_\eta = (u_\eta, v_\eta)$. Equations (3.6) are then modified as follows

$$u_{\xi\xi} + u_{\eta\eta} + 2\lambda\{[\alpha_1'(\alpha_1'u_\xi + \alpha_2'v_\xi)]_\xi + [\beta_1'(\beta_1'u_\eta + \beta_2'v_\eta)]_\eta = 0, \tag{3.7}$$

$$v_{\xi\xi} + v_{\eta\eta} + 2\lambda\{[\alpha_2'(\alpha_1'u_\xi + \alpha_2'v_\xi)]_\xi + [\beta_2'(\beta_1'u_\eta + \beta_2'v_\eta)]_\eta = 0.$$

where $\beta(\xi,\eta) \equiv (\beta_1', \beta_2') = (-\beta_2, \beta_1)$.

Finally, we endow the proposed system of the elliptic partial differential equations with appropriate boundary conditions designed in such a way that the grid nodes slide along the boundary to adapt to the geometry of the grid lines inside the parametric region. Their positions are obtained iteratively by projecting the near-boundary nodes onto the boundary along the direction of the grid lines (see details in [159]).

The numerical solution of the system (3.7) is based on the discrete Laplacian, the central differences for the first derivatives and numerical iterations. The corresponding finite-difference equations are solved by the Newton method.

## 3.3  Bias Space Filling Curve (BSFC)

Although the generated curvilinear grid has been aligned with the prescribed vector field, the distance between the CC points has not been optimized with regard to the machining strip. Therefore, the grid is converted into a pair of continuous functions $u(\xi,\eta), v(\xi,\eta)$ using the bilinear interpolation. Next, we construct two iso-parametric paths in the $\xi$ and $\eta$-direction by calculating the largest tool path interval and using it as an offset as follows. The first tool track $T_0$ lies at the boundary of the parametric domain. Next, $T_1$ is a curve $\eta=\eta_1$ defined by $\{u(\xi,\eta_1), v(\xi,\eta_1)\}$ such that $\text{dist}_H(T_0,T_1) < w_{R,0} + w_{L,1}$, where $w_{L,0}, w_{R,1}$ is the left and the right maximum allowed strip width. The next track is generated by $\{u(\xi,\eta_2), v(\xi,\eta_2)\}$ such that $\text{dist}_H(T_1,T_2) < w_{R,1} + w_{L,2}$. The two overlaying tool paths represented by the coordinate lines are characterized by the maximum possible machining strip between any pair of the adjacent tool tracks.

Next, the problem is simplified by thresholding the vector field as follows:

$$I(\xi,\eta) = \begin{cases} V(\xi,\eta), & \text{if } K_I > k', \\ (0,0), & \text{otherwise,} \end{cases} \tag{3.8}$$

where $k'$ is the prescribed threshold and $K_I$ is the measure of importance of the particular point. We consider, two measures, $\max|K|$, where $K$ is the curvature of the surface and $\max R_M - \min R_M$. The first measure is the basic characteristic of the surface implying that if the curvature of the surface is high, the feed direction is important. The second measure tells you that if the difference between the max and the minimum material removal rate at the particular point is large, the feed direction is important. Equation (3.8) defines "important points", where $I(u,v) \neq 0$ and "unimportant points", where $I(u,v) = 0$.

Furthermore, the rectangular grid in $(\xi,\eta)$ is regarded as an undirected graph $G$, where each two adjacent cells are connected by an edge. The cells are then connected by the biased adaptive space filling curve (BSFC) using the following procedure.

Consider an "important" cell $A$.

**Case 1**. The grid is well aligned with the vector field. In this case, $A$ can be connected with one of the neighboring cells $B$ such that $\overrightarrow{AB}$ is almost parallel or almost antiparallel to the direction of the corresponding vector field $V(\xi,\eta)$ (see Figure 3.5).

**Case 2**. The grid is not well aligned with the vector field. In this case none of the directions $\overrightarrow{AB}$ is close to $V(\xi,\eta)$. Therefore, we evaluate the material removal rate $R_{M_1}$ $R_{M_2}$, $R_{M_3}$, $R_{M_4}$ in the four possible directions and connect in the direction of the $\max_i R_{M_i}$ (as shown in Figure 3.5).

Finally, if cell $A$ is unimportant, we connect it with one of the four neighboring cells randomly. Within this framework it is often practical to use the "tracing bug" techniques designed to avoid frequent turns. In this case the unimportant

43

cell is connected to the next cell following the direction of the tracing bug from the preceding step.
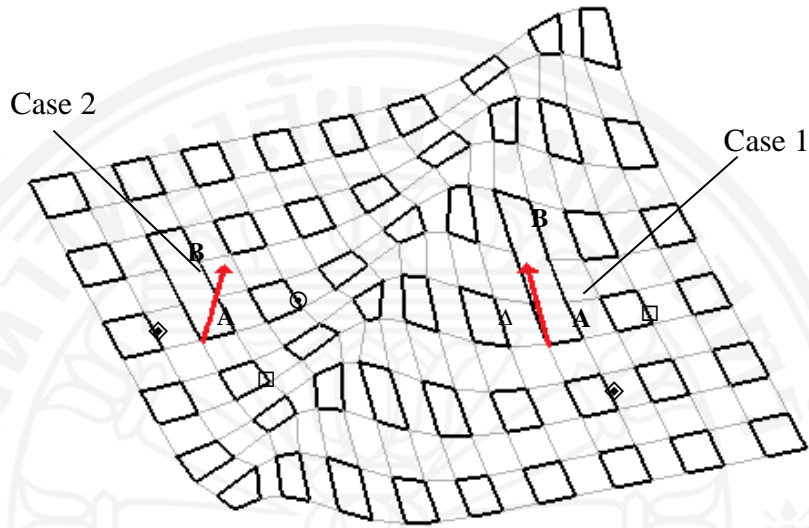


Figure 3.5: BSFC: case 1 and case 2; $\odot$ $\square$ $\Delta$ $\diamondsuit$ denote $R_{M_1}$ $R_{M_2}$ $R_{M_3}$ $R_{M_4}$, respectively.

Finally, the BSFC is a modification of the adaptive SFC proposed in [61]. The advantage of BSFC is the reduction of the machining time by following a set of the prescribed directions at the important points. Furthermore, large kinematic errors appear when the tool feed vector abruptly changes direction. Therefore, the BSFC decreases the kinematic error by reducing frequent sharp turns using the following correction. For each point we calculate the number of the preceding consecutive turns. The segments with a large number of turns will be marked and the vector field $V(\xi,\eta)$ at each point of this segment will be adjusted as follows: $V(\xi,\eta) = d_W(\xi,\eta)$, where $d_W(\xi,\eta)$ denotes the "principal direction" in a window around a segment as shown in Figure 3.6. The procedure can be considered as a high frequency filter.

Figure 3.7 illustrates the diagram of VFAP algorithm described above.

The segment with the
large number of turns

Corrected

(a)      Marked segments                    (b) Corrected BSFC
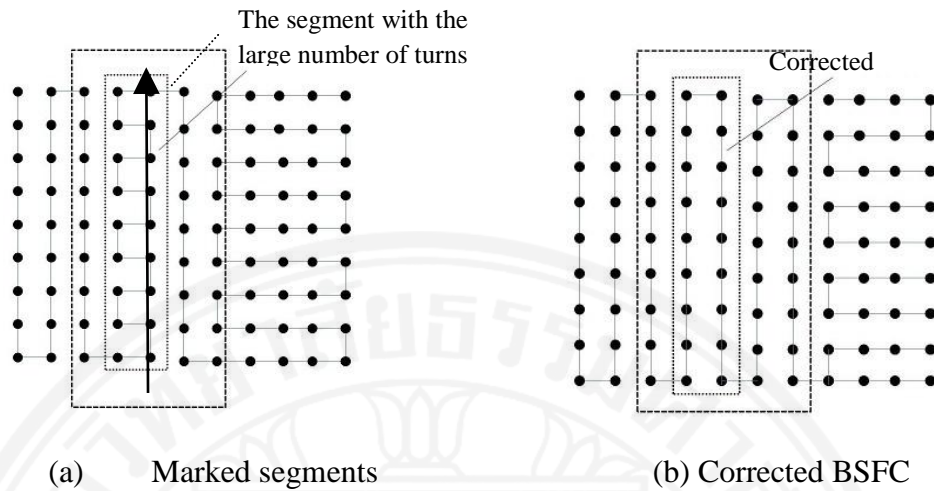
Figure 3.6: Correcting the biased space filling curve



Surface Characteristic Analysis

Input

Ouput

Parametric Surface

- Normal
- Principal curvature direction
  - Maximum curvature
  - Minimum curvature

Curvilinear Grid Generation

Input

Ouput

Defining the cost functions
- Maximal strip width
- Minimum machining time*
- Maximal removal rate*
- Min kinematic error*
* need machine configuration info

Curvilinear Grid

Toolpath Generation

Input

Ouput

- Machining parameters
  - cutter: radius, type
  - scallop-height
- Methods
  - iso-parametric
  - BSFC
- Curvilinear Grid

Toolpath
(G-code)

Figure 3.7: VFAP algorithm

## 3.4 Quality of the machined surface

We measure the quality of the machined surface in terms of its roughness and waviness. Roughness represents micro peaks and valleys of the surface produced by the tool while waviness is often attributed to the vibrations. Waviness often increases when the milling machine operations involve large and sharp periodic rotations. Considering the surface as a 2D signal, the roughness is associated with high frequencies of the signal and the waviness with medium frequencies (Figure 3.8).
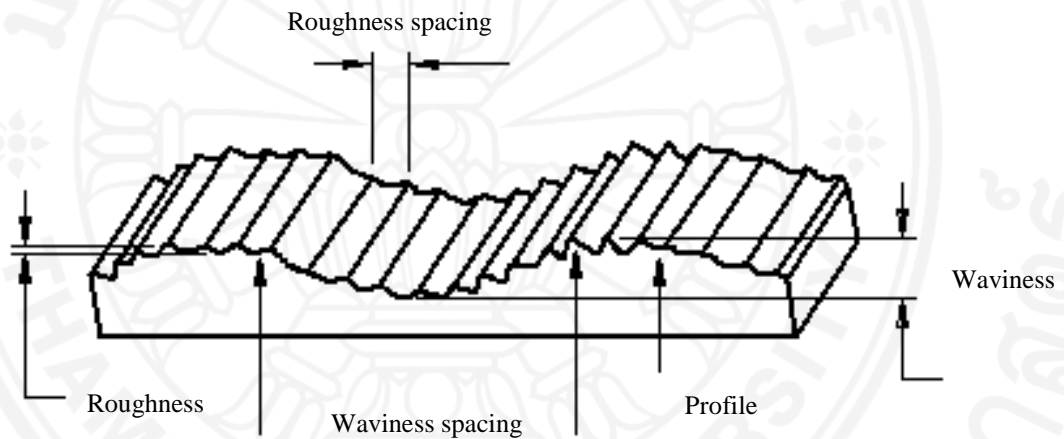


Figure 3.8: Surface characteristics and terminology

We measure the roughness by one of the most commonly used methods called the stylus contact profiling [163]. The surface profile obtained by a high-resolution probe is post processed by the Gaussian filter [164]. The surface roughness is given by $R_a = \frac{1}{N} \sum_{i=1}^{N} |y_i|$, where $y_i$ is the height of the profile relative to a mean Gaussian curve and $N$ the total number of the measurement points. Furthermore, the Gaussian filter allows us to evaluate waviness by subtracting the roughness profile from the raw profile.

We measured 20 sample profiles with the standard cutoff of 0.8 mm [164]. The average value was compared with the roughness and waviness produced by the conventional method. The roughness of the machined surfaces was within the acceptable range for surface milling operations, that is, between 0.2 and 25 µm [165] (see Figure 3.9).

| $R_a$ µm | 50 | 25 | 12.5 | 6.3 | 3.2 | 1.6 | .8 | .4 | .2 | .1 | .05 | .025 | .012 |
|---|---|---|---|---|---|---|---|---|---|---|---|---|---|
| $R_a$ µin | 2000 | 1000 | 500 | 250 | 125 | 63 | 32 | 16 | 8 | 4 | 2 | 1 | .5 |

**METAL CUTTING**

- sawing
- planning, shaping
- drilling
- milling
- boring, turning
- broaching
- reaming

Common ▪ (black) less frequent ▪ (gray)
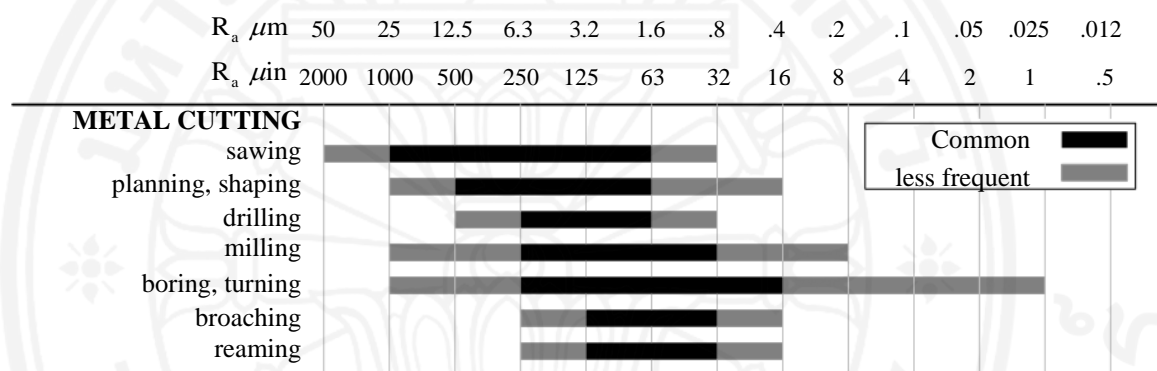
Figure 3.9: Acceptable surface roughness

### 3.5 Experiments of VFAP algorithm

In this section, the proposed VFAP-BSFC method is compared with the iso-parametric zigzags tool path (ISO) for both parametric surface and triangle facet mesh surface (STL). The experiment also tests the methods against MasterCam X5, "Follow Periphery" (UG-FP), "Helical or Spiral"(UG-HS) options of Unigraphics NX9 and the adaptive curvilinear SFC [61]. The test surfaces were initialized in the MasterCam environment using a parametric representation. Next, the surfaces were exported into the STEP or IGES formats and imported into the UG. The test process has been applied with an appropriate setup optimization [118]. The accuracy of the machining has been evaluated in terms of the kinematic error, roughness and waviness. All surfaces have been machined by the flat-end tool.

The evaluation process also tests the proposed cost function against minimization based merely on the length of the tool path. In this case, the vector field is generated along the direction of the maximum machining strip and the BSFC is based on the length of the tool path. The corresponding cost function is evaluated by replacing the material removal rates with the length of the tool path between the corresponding nodes. The indication of material removal rate and the tool path length versions of the optimization is denoted by subscripts $R$ and $L$, respectively, for instance $VFAP_R$ and $VFAP_L$.

The three convex-concave single parametric surfaces have been tested using proposed VFAP-BSFC technology.

### 3.5.1 Example 1. A Concave–Convex Surface with Multiple Peaks. Rough Cut

The example demonstrates the efficiency the VFAP with the reference to the traditional iso-parametric path (ISO), an automatic tool path generation procedure of MasterCam X5 as well as the algorithms UG-FP and UG-HS. We also test $VFAP_L$ against $VFAP_R$ and against the adaptive SFC based on the kinematic error proposed in [61].

Consider a surface in Figure 3.10(a) given by

$$
\begin{aligned}
x(u,v) &= 100u - 50, \\
y(u,v) &= 100v - 50, \\
z(u,v) &= 11.6e^{-30(v-1.7u+0.3)^2} + 11.6e^{-30(v-1.7u+1.3)^2} + 11.6e^{-30(1.7u-v+0.6)^2} \\
&\quad - 33.3v(v-1) + 70.
\end{aligned}
\tag{3.9}
$$
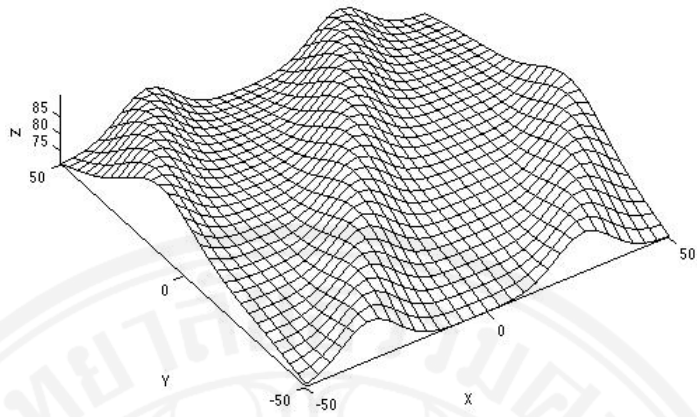
(a)　　　The part surface



(b)　　vector field $V_L$



(c)　　vector field $V_R$



(d)　　grid $G_L$



(e)　　grid $G_R$

(f)     SFC$_L$                     (g)     SFC$_R$

(h)     BSFC$_L$                   (i)     BSFC$_R$

(j)     $G_A$                          (k)     SFC$_A$
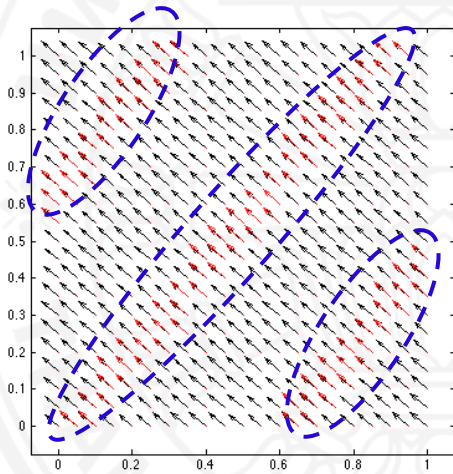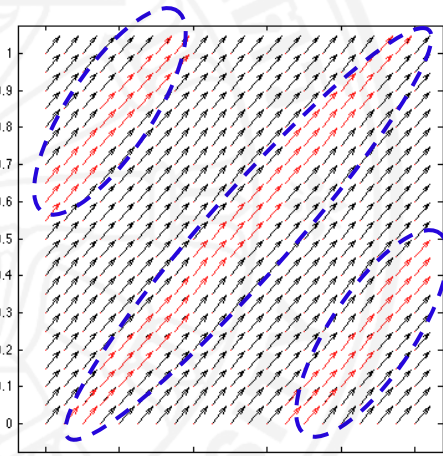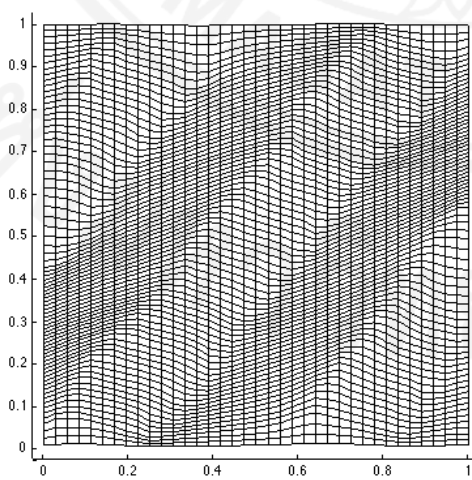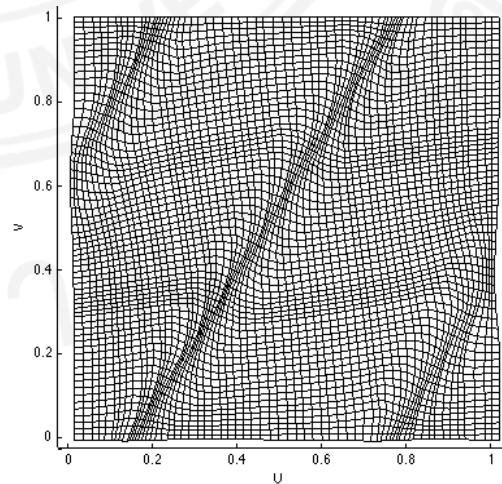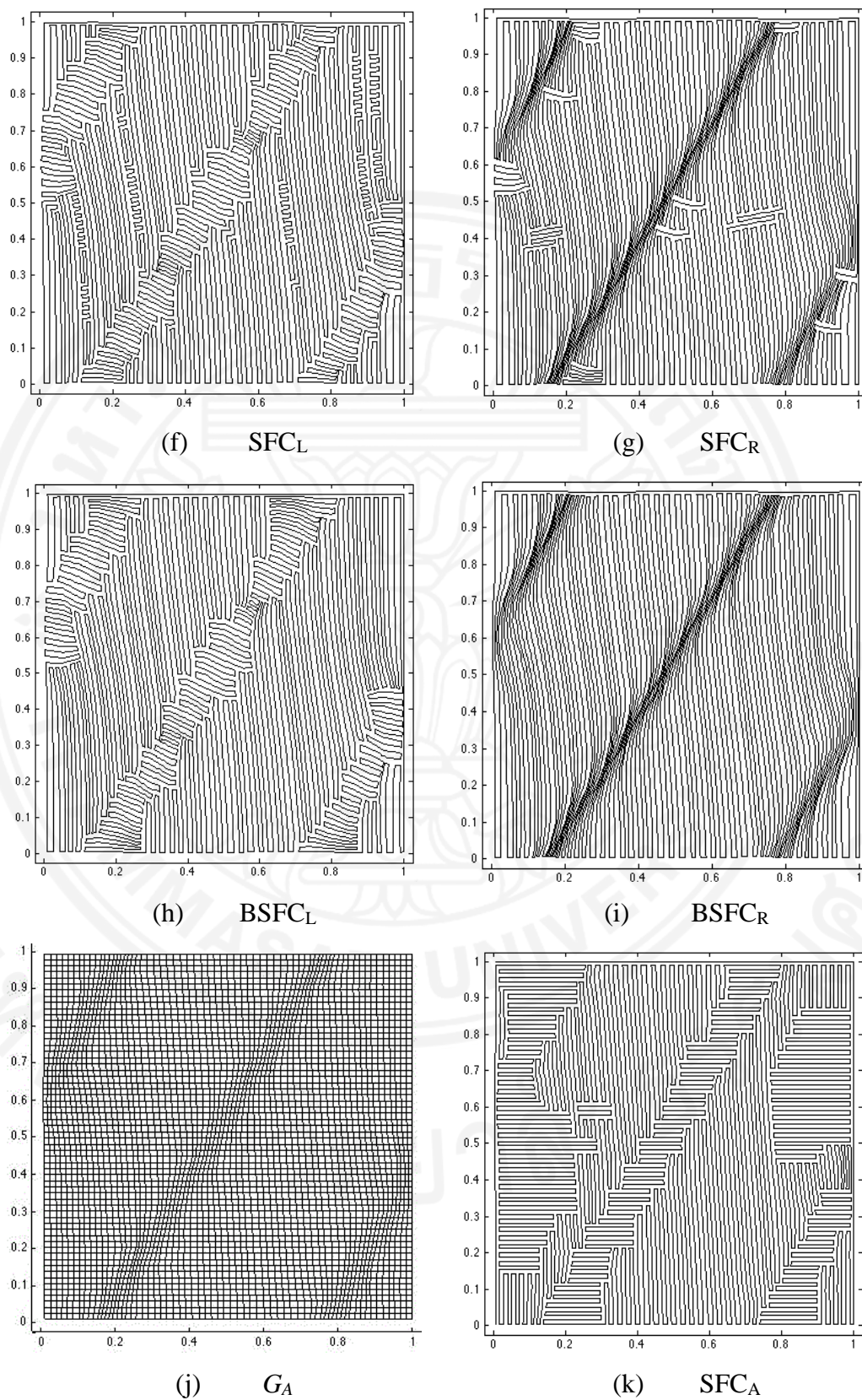
Figure 3.10: VFAP solution for surface 1

The corresponding vector fields $V_L$ and $V_R$ are shown in Figure 3.10(b) and (c) respectively, where the dashed lines indicate the "important points." The curvilinear grids $G_L$ and $G_R$ adapted to the prescribed vector fields are shown in Figure 3.10 (d) and (e). $SFC_L$ and $SFC_R$ are displayed in Figure 3.10 (f) and (g), whereas the proposed $BSFC_L$ and $BSFC_R$ are shown in Figure 3.10 (h) and (i). Additionally, we generated a curvilinear grid $G_A$ and the corresponding adaptive $SFC_A$ [61] shown in Figure 3.10 (j) and (k). The grid and the $SFC_A$-tool path have been constructed using the minimization of the kinematic error [61]. The surface was machined virtually by Vericut 7.0 and on the five-axis machine HAAS VF-2TR by a flat-end tool with the radius 4 mm.

The results obtained by the VFAP technology compared with the conventional ISO toolpath, MasterCam X5, UG-FP, UG-HS and the adaptive $SFC_A$ are given in Table 3.1. The improvement is defined as $\dfrac{before-after}{before}100$. The machining depends on the configuration of the machine, position of the workpiece and the prescribed scallop height; however, VFAP always provides an improvement. Furthermore, $VFAP_R$ designed to reduce the machining time provides 37%, and 28% improvement of the machining time for the MAHO 600E and HAAS VF2TR, respectively, whereas $VFAP_L$ generates 40% improvement in terms of the tool path length. This is considerable progress considering hundreds or even thousands of hours typically spent for machining complicated industrial parts.

Figure 3.11 shows the surface obtained by the ISO tool path vs. surfaces machined using the proposed method. Table 3.1: VFAP vs. conventional tool paths. Surface 1 displays the advantages of the method. For instance, the maximum allowed scallop of 0.05 mm requires 1h04 min and 1h43 minutes for a non-optimal tool path on MAHO 600E and HAAS VF2TR, whereas with the optimization the machining requires 40min and 1h14min, respectively. Clearly, it is an impressive advantage for such a small workpiece of 100x100mm.

51

Table 3.1: VFAP vs. conventional tool paths. Surface 1

| Tool radius 4 mm | | | Tool path generation method | | Scallop height(mm) | | |
|---|---|---|---|---|---|---|---|
| | | | | | 0.25 | 0.1 | 0.05 |
| Performance | Tool path length (mm) | | Master CAM | | 34698.0 | 75392.0 | 144098.0 |
| | | | UG | HS | 30713.0 | 74354.0 | 148130.0 |
| | | | | FP | 6707.8 | 10833.0 | 15280.0 |
| | | | ISO Zigzag | | 6371.9 | 10187 | 14535 |
| | | | $G_A$ | $SFC_L$ | 4417.9 | 6605.3 | 9367.5 |
| | | | $VFAP_L$ | | 4473.3 | 6176.1 | 8610.3 |
| | | | $VFAP_R$ | | 4724.1 | 7117.0 | 9947.0 |
| | Machining Time | MAHO 600E | UG | HS | 3:24:33.8 | 8:18:32.6 | 16:37:30.3 |
| | | | | FP | 0:39:34.1 | 1:05:15.8 | 1:33:52.2 |
| | | | ISO Zigzag | | 0:28:01.0 | 0:44:58.0 | 1:04:21.0 |
| | | | $G_A$ | $SFC_L$ | 0:27:15.3 | 0:42:36.5 | 0:59:32.2 |
| | | | $VFAP_L$ | | 0:27:13.2 | 0:42:10.7 | 0:58:18.5 |
| | | | $VFAP_R$ | | 0:18:14.2 | 0:28:03.4 | 0:40:04.2 |
| | | HAAS VF2TR | UG | HS | 6:15:24.6 | 15:07:51.0 | 30:07:46.4 |
| | | | | FP | 0:39:35.6 | 2:13:45.3 | 3:10:43.1 |
| | | | ISO Zigzag | | 0:45:08.0 | 1:12:41.0 | 1:43:41.0 |
| | | | $G_A$ | $SFC_L$ | 0:44:34.2 | 1:09:20.5 | 1:37:29.2 |
| | | | $VFAP_L$ | | 0:43:57.9 | 1:08:40.3 | 1:35:52.4 |
| | | | $VFAP_R$ | | 0:33:52.7 | 0:52:47.5 | 1:14:28.2 |
| Advantage rel. to ISO | Tool path length (mm) | | $G_A$ | $SFC_L$ | 30.7% | 35.2% | 35.6% |
| | | | $VFAP_L$ | | 29.8% | 39.4% | **40.8%** |
| | | | $VFAP_R$ | | 25.9% | 30.1% | 31.6% |
| | Machining Time | MAHO 600E | $G_A$ | $SFC_L$ | 2.7% | 5.2% | 7.5% |
| | | | $VFAP_L$ | | 2.8% | 6.2% | 9.4% |
| | | | $VFAP_R$ | | 34.9% | 37.6% | **37.7%** |
| | | HAAS VF2TR | $G_A$ | $SFC_L$ | 1.2% | 4.6% | 6.0% |
| | | | $VFAP_L$ | | 2.6% | 5.5% | 7.5% |
| | | | $VFAP_R$ | | 24.9% | 27.4% | **28.2%** |

(a) conventional zigzag, virtual cut
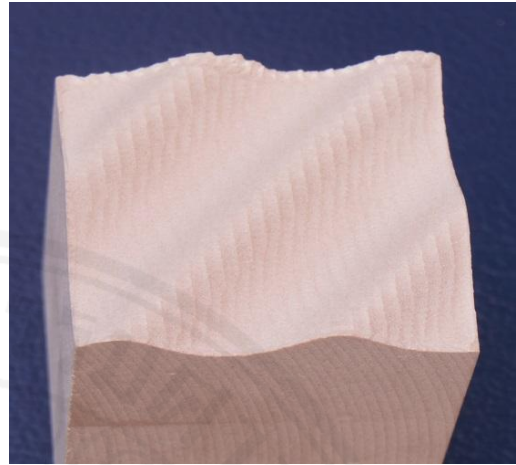
(b) conventional ISO zigzag, actual cut, tool path length = 14535.0 mm, time = 1:43:41 hrs

(c) VFAP$_L$, virtual cut

(d) VFAP$_L$, actual cut, tool path length = 8610.3 mm (**advantage 40.8%),** time = 1:35:52 hrs (**advantage 7.5%)**

| (f) | VFAP$_R$, virtual cut |
|---|---|

(f) VFAP$_R$, actual cut, tool path length = 9947.0 mm (**advantage 31.6%),** time = 1:14:28 hrs (**advantage 28.2%)**

Figure 3.11: Test surface 1. Virtual and real machining

Observe an overwhelming advantage over the tool path generated by MasterCam X5. For $h$=0.25, 0.1 and 0.05 mm, the tool path length has been reduced by factors of 4, 10 and 14, respectively. Furthermore, the UG tool path is considerably better than that generated by MasterCam and the proposed method outperforms UG as well. For instance, compared to UG-FP the tool path has been reduced by 34%, 43% and 43.5% for $h$=0.25, 0.1 and 0.05, respectively.

There is a clear advantage in the machining time as well. For example, on MAHO 600E for $h$=0.25 the VFAP$_R$ requires 40 min versus 1h33min using UG-FP and 16h37min using UG-HS( see a detailed comparison in Table 3.1).

Finally, cutting large complex industrial parts with a high accuracy employs tens or hundreds of thousands, and even millions of CC points and hundreds of hours. Therefore, the improvement in the tool path length and in the machining time is significant, saving long hours of machining and reducing wear on the tool.

Table 3.2 displays the kinematic error. The constraint imposed on the scallop height $h$ is used as an upper limit for the allowable kinematic error. If the kinematic error between two CC points exceeds $h$, an additional CC point is inserted until $\max(\varepsilon) \le h$.

Next, we evaluate the average error given by $\varepsilon' = \dfrac{\sum\limits_{k=0}^{m-1} \varepsilon_k}{m}$, where $m$ is the number of trajectories. If $\varepsilon' \ll h$, the surface is close to the required surface not only in the sense of the maximum Hausdorff distance, but in the sense of the average Hausdorff distance as well. This indicates a good quality of the surface.

Clearly, the average error is a small fraction of the required accuracy $h$. As a matter of fact, the difference between the results is in the range of 0.02 for $h$=0.25, 0.01 for $h$=0.1 and 0.001 for $h$=0.05. For the majority of the modern milling machines this difference still lies outside the range of machining accuracy. Therefore, the proposed method provides a tangible increase in terms of the length of the tool path and the machining time while maintaining the same accuracy. Table 3.2 demonstrates that the method substantially reduces the number of required CC points for high accuracy milling ($h$=0.1 and $h$=0.01). Note that the decrease in the number of the CC points is in particular important for high speed milling when the programmed feed rate can exceed the sampling speed of the controller.

Table 3.2: Kinematic error VFAP vs. conventional tool paths. Surface 1

| | Tool path generation method | | Hausdorff distance between the actual and required trajectory | | | | | | | | |
| | | | $h$=0.25 | | | $h$=0.10 | | | $h$=0.05 | | |
| | | | #CC | Ave | Std | #CC | Ave | Std | #CC | Ave | Std |
|---|---|---|---|---|---|---|---|---|---|---|---|
| MAHO 600E | UG | HS | 5557 | 0.055 | 0.059 | 32351 | 0.033 | 0.026 | 120327 | 0.020 | 0.013 |
| | | FP | **1139** | 0.047 | 0.057 | 7329 | 0.029 | 0.025 | 14542 | 0.018 | 0.013 |
| | ISO Zigzag | | 4574 | 0.075 | 0.057 | 9339 | 0.043 | 0.023 | 17940 | 0.024 | 0.011 |
| | $G_A$ | $SFC_L$ | 3390 | 0.106 | 0.059 | 7577 | 0.045 | 0.024 | 14932 | 0.023 | 0.012 |
| | VFAP$_L$ | | 3552 | 0.097 | 0.059 | 7413 | 0.043 | 0.023 | 14601 | 0.022 | 0.012 |
| | VFAP$_R$ | | 2622 | 0.085 | 0.058 | **5689** | 0.042 | 0.023 | **11526** | 0.021 | 0.012 |
| HASS VF2TR | UG | HS | 8649 | 0.066 | 0.063 | 48163 | 0.037 | 0.026 | 169196 | 0.022 | 0.012 |
| | | FP | 1675 | 0.057 | 0.060 | 8154 | 0.034 | 0.026 | 18810 | 0.034 | 0.027 |
| | ISO Zigzag | | 4677 | 0.087 | 0.058 | 10205 | 0.044 | 0.022 | 19455 | 0.025 | 0.011 |
| | $G_A$ | $SFC_L$ | 3510 | 0.108 | 0.060 | 8178 | 0.045 | 0.023 | 16603 | 0.023 | 0.011 |
| | VFAP$_L$ | | 3652 | 0.104 | 0.061 | 8159 | 0.045 | 0.023 | 16373 | 0.023 | 0.011 |
| | VFAP$_R$ | | 2805 | 0.095 | 0.060 | 6323 | 0.043 | 0.022 | 12910 | 0.022 | 0.011 |

Table 3.3 displays the average roughness and waviness of the machined surface. Roughness of VFAP$_L$ ,VFAP$_R$ and ISO-zigzag is 6.1, 6.2  and 6.7 µm, respectively, whereas the waviness of VFAP$_L$ is about 14 µm and  VFAP$_R$ and ISO-zigzag is about 27 µm for both cases. Therefore, the surface generated by the proposed method is characterized by a slightly better roughness and waviness relative to the conventional ISO–path while outperforming the conventional zigzag in terms of the cutting time and the length of the tool path.  Finally, the measured roughness complies with the standard industrial requirements for the quality of the surface milling (see Figure 3.9).

Table 3.3: Roughness and Waviness of VFAP vs. conventional tool paths. Surface 1

| Roughness $R_a$ ($\mu$m) | | | Standard Deviation | | | Waviness ($\mu$m) | | | Standard Deviation | | |
|---|---|---|---|---|---|---|---|---|---|---|---|
| ISO Zigzag | VFAP$_L$ | VFAP$_R$ | ISO Zigzag | VFAP$_L$ | VFAP$_R$ | ISO Zigzag | VFAP$_L$ | VFAP$_R$ | ISO Zigzag | VFAP$_L$ | VFAP$_R$ |
| 6.7 | 6.2 | **6.1** | 9.1 | 8.5 | 3.7 | 26.9 | 26.9 | **13.7** | 8.1 | 7.9 | **4.7** |

### 3.5.2 Example 2 A Peak-crossing Surface

Analyzing surface 1 above characterized by the parallel diagonal peaks, one may arrive at the following question. "Can we rotate the standard zigzag path so that the cut is performed along the optimal direction?" Unfortunately, it is not always possible. Consider a surface in Figure 3.12(a) given by

$$
\begin{aligned}
x(u,v) &= 50u - 25, \\
y(u,v) &= 50v - 25, \\
z(u,v) &= 4.5\left(e^{-30(v-2u+0.5)^2} + e^{-30(u+2v-1.5)^2}\right)
\end{aligned}
\tag{3.10}
$$

The corresponding vector fields $V_L$ and $V_R$ are shown in Figure 3.12(b) and Figure 3.12 (c). The diagonal clusters of "important points" are indicated by the dashed lines.
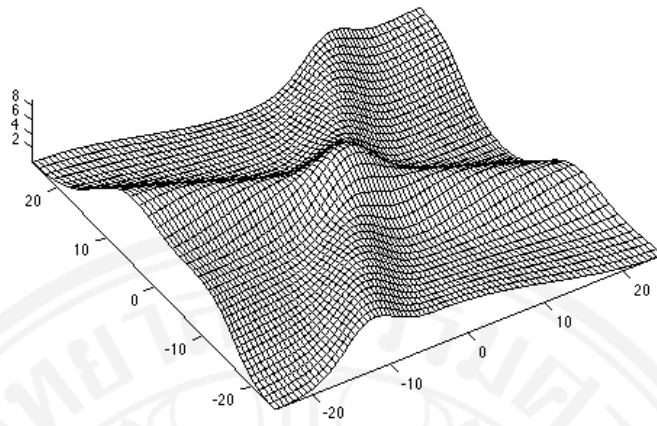
(a)      Test surface 2



(b) vector field $V_L$



(c) vector field $V_R$



(d) grid $G_L$



(e)  grid $G_R$

57
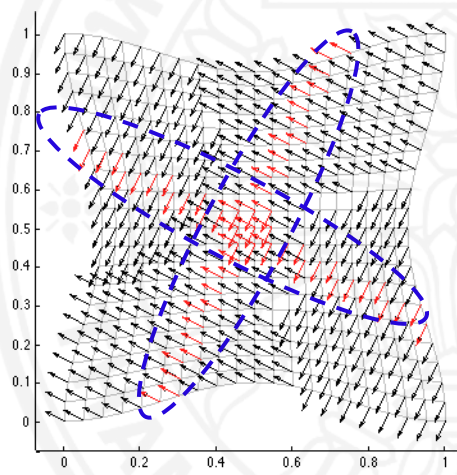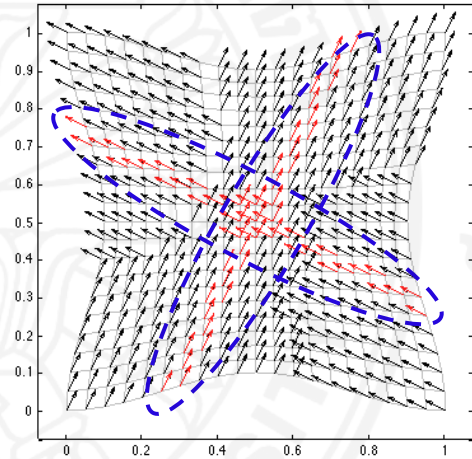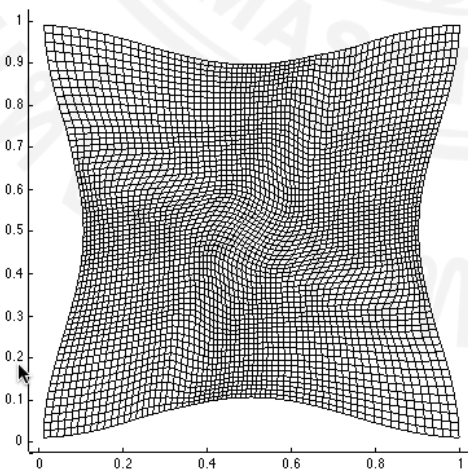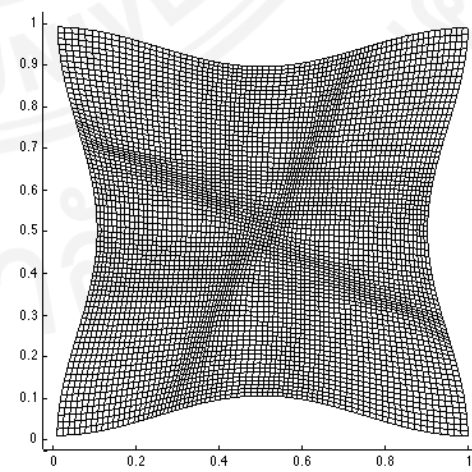
(f) BSFC$_L$                    (g) BSFC$_R$
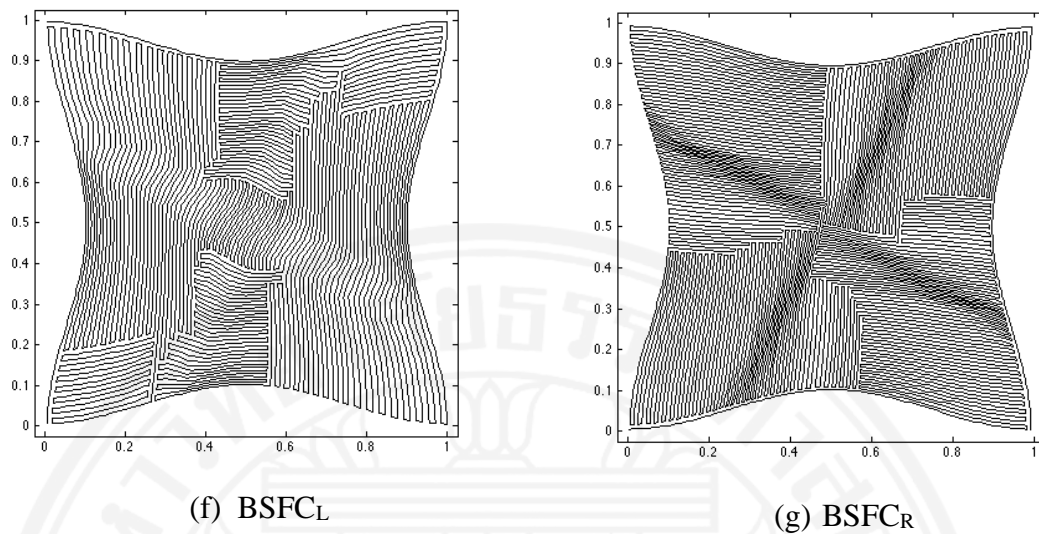
Figure 3.12: VFAP solution for surface 2

Clearly, the above mentioned re-orientation cannot provide the required alignment. Besides, the surface is defined on a curvilinear rectangle which creates additional problems for a conventional tool path generation. Therefore, the curvilinear grids $G_L$ and $G_R$ in Figure 3.12 (d) and (e) are generated using the dual vector field technology (see Figure 3.4). The corresponding BSFC$_L$ and BSFC$_R$ are shown in Figure 3.12 (f) and (g). The virtual cuts performed with the 2 mm flat-end tool radius and the 0.25 mm maximum scallop height are shown in Figure 3.13 (a) -(c) for ISO, VFAP$_L$ and VFAP$_R$, respectively.
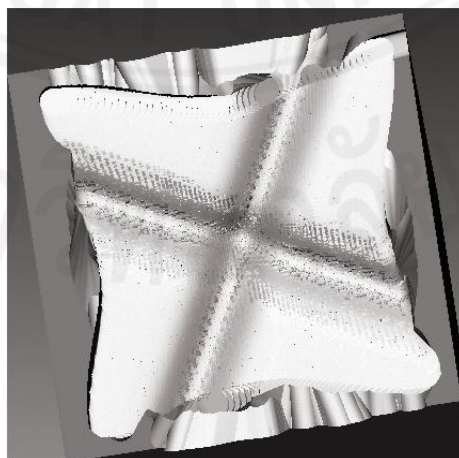


(a)conventional ISO zigzag tool path length= 5644.3 mm, time = 1:15:03 hrs
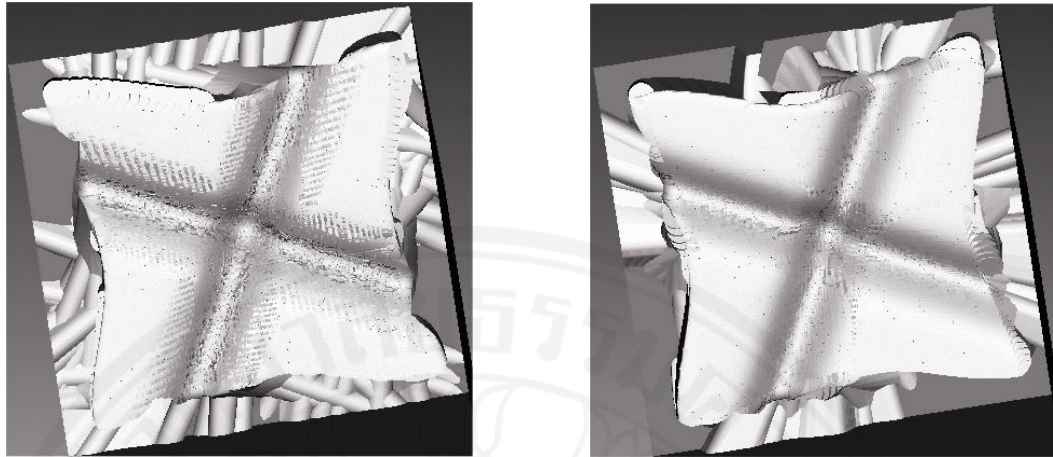
(b)   VFAP$_L$, tool path length = 4323.5 mm (**advantage 23.4%)**,    time = 1:13:12 hrs (**advantage 2.5%)**

(c)   VFAP$_R$, tool path length = 5323.8 mm (**advantage 5.7%)** , time = 0:56:26 hrs (**advantage 24.8%)**

Figure 3.13: Example 2 Machined surfaces

Table 3.4 demonstrates advantages of the proposed method over ISO, MasterCam X5, UG-FP and UG-HS. The proposed method outperforms the above algorithms for every prescribed scallop height. For instance, for h=0.25mm VFAP$_L$ tool path is 5.3 times shorter than that generated by MasterCam, 23% shorter than ISO, 7.8 times shorter than UG-HS and 40% shorter than UG-FP.

There is a clear advantage in the machining time as well. For instance, MAHO 600E for $h$=0.05 the VFAP$_R$ requires 13min versus 46min using UG-FP and 3h02min using UG-HS( see the full evaluation in Table 3.4).

Table 3.5 shows the accuracy of the proposed method in terms of the kinematic error. The error behaves similarly to Example 1 with negligible deviations from the prescribed accuracy. Still, the orientation may help. As a matter of fact, a complicated surface may require a combination of orientation and the proposed BSFC. However, as long as there is at least one non-linear or even diagonal cluster of important points there always will be benefits provided by the VFAP technology.

Finally, as opposed to Example 1, where only one family of the grid curves was adapted to the required vector field (see Equation (3.6), Example 2 shows the efficiency of the method applied with the dual vector fields.

Table 3.4: VFAP vs. conventional tool paths. Surface 2

| Tool radius 2 mm | | | Tool path generation method | | Scallop height(mm) | | |
|---|---|---|---|---|---|---|---|
| | | | | | 0.25 | 0.1 | 0.05 |
| **Performance** | Tool path length (mm) | | Master CAM | | 6325.5 | 13760.0 | 23294.4 |
| | | | UG | HS | 6555.2 | 15595.5 | 33865.5 |
| | | | | FP | 3283.6 | 5138.9 | 7260.3 |
| | | | ISO Zigzag | | 2591.4 | 4021.7 | 5644.3 |
| | | | VFAP$_L$ | | 2036.1 | 3125.0 | **4323.5** |
| | | | VFAP$_R$ | | 2483.9 | 3807.4 | 5323.8 |
| | Machining Time | MAHO 600E | UG | HS | 0:34:55.3 | 1:22:50.4 | 3:02:12.2 |
| | | | | FP | 0:20:08.2 | 0:32:17.8 | 0:46:07.8 |
| | | | ISO Zigzag | | 0:08:05.2 | 0:12:40.4 | 0:17:51.8 |
| | | | VFAP$_L$ | | 0:07:53.8 | 0:12:18.6 | 0:17:10.2 |
| | | | VFAP$_R$ | | 0:06:29.9 | 0:09:55.3 | 0:13:47.7 |
| | | HAAS VF2TR | UG | HS | 2:59:36.0 | 7:10:23.0 | 14:54:48.8 |
| | | | | FP | 1:27:46.9 | 2:18:47.6 | 3:16:01.8 |
| | | | ISO Zigzag | | 0:33:48.7 | 0:53:10.3 | 1:15:03.7 |
| | | | VFAP$_L$ | | 0:34:21.1 | 0:52:03.5 | 1:13:12.6 |
| | | | VFAP$_R$ | | 0:26:42.5 | 0:41:55.5 | **0:56:26.1** |
| **Advantage rel. to ISO** | Tool path length (mm) | | VFAP$_L$ | | 21.4% | 22.3% | **23.4%** |
| | | | VFAP$_R$ | | 4.1% | 5.3% | 5.7% |
| | Machining Time | MAHO 600E | VFAP$_L$ | | 2.3% | 2.9% | 3.9% |
| | | | VFAP$_R$ | | 19.6% | 21.7% | **22.8%** |
| | | HAAS VF2TR | VFAP$_L$ | | -1.6% | 2.1% | 2.5% |
| | | | VFAP$_R$ | | 21.0% | 21.2% | **24.8%** |

Table 3.5: Kinematic error. VFAP vs. conventional tool paths. Surface 2

| | Tool path generation method | | Hausdorff distance | | | | | | | | |
|---|---|---|---|---|---|---|---|---|---|---|---|
| | | | $h$=0.25 | | | $h$=0.10 | | | $h$=0.05 | | |
| | | | #CC | Ave | Std | #CC | Ave | Std | #CC | Ave | Std |
| MAHO 600E | UG | HS | 2130 | 0.043 | 0.056 | 9940 | 0.026 | 0.025 | 37174 | 0.018 | 0.012 |
| | | FP | **1732** | 0.055 | 0.061 | 5973 | 0.032 | 0.027 | 12115 | 0.019 | 0.013 |
| | ISO Zigzag | | 4584 | 0.030 | 0.046 | 7834 | 0.021 | 0.022 | 12306 | 0.015 | 0.012 |
| | VFAP$_L$ | | 2330 | 0.057 | 0.061 | **5678** | 0.030 | 0.026 | **11922** | 0.016 | 0.013 |
| | VFAP$_R$ | | 2436 | 0.035 | 0.041 | 5998 | 0.013 | 0.014 | 11957 | 0.007 | 0.007 |
| HASS VF2TR | UG | HS | 7268 | 0.085 | 0.064 | 34395 | 0.041 | 0.025 | 113968 | 0.024 | 0.011 |
| | | FP | 4192 | 0.085 | 0.068 | 12240 | 0.041 | 0.026 | 27106 | 0.022 | 0.012 |
| | ISO Zigzag | | 5164 | 0.059 | 0.065 | 9966 | 0.032 | 0.025 | 17349 | 0.020 | 0.012 |
| | VFAP$_L$ | | 3378 | 0.095 | 0.069 | 8610 | 0.041 | 0.025 | 18536 | 0.021 | 0.012 |
| | VFAP$_R$ | | 2789 | 0.064 | 0.061 | 6709 | 0.023 | 0.023 | 13444 | 0.012 | 0.012 |

### 3.5.3 Example 3. A Semi-Oval Ridge (Composite Grid) Rough and Fine Cut

A surface in Figure 3.14 (a) is characterized by a ridge nearby the boundary. We adopted this shape from the dental micro-milling, where the elevated part represents the ridges of a dental crown or implant [166]. The VFAP for such surfaces can be combined with a decomposition of the parametric region and generation of a curvilinear grid in each subregion. Figure 3.14 (b) shows that the most important region is a semicircular ridge nearby the boundary characterized by the high curvature



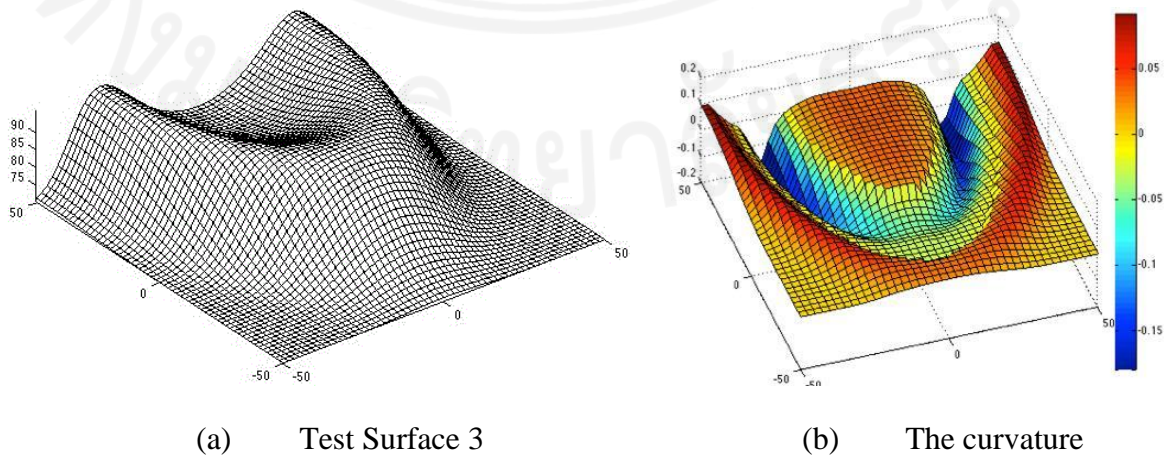(a)     Test Surface 3                    (b)     The curvature

Figure 3.14: The test surface 3 and its curvature

We model a situation when the user needs a minimal tool path for the rough cut to reduce the tool wear and the minimal time for the fine cut. The proposed tool path generation method allows for these strategies. The rough machining is performed along the direction of the highest curvature in order to maximize the machining strip, that is, VFAP$_L$. This machining path has been employed in order to minimize the tool wear during the rough machining. The finishing strategy employs VFAP$_R$ which maximizes the material removal rate and reduces the machining time. We observed that most of the time the tool is moving along the direction of the minimal curvature.

The parametric region is decomposed into several subregions taking into account the direction of the vector field. Such decomposition can be performed manually, or using vector field clustering [41]. In our particular case, the "important points" belong to a semi-circular region shown in Figure 3.14 (b). The tool path in the remaining region does not generate large errors. Therefore, we partition the parametric region into two subregions and construct the required curvilinear grid in each subregion independently (see Figure 3.15(a)). The BSFCs for the rough and fine cuts constructed from the curvilinear grid are shown in Figure 3.15 (b) - (e), respectively. Note that in this particular case we use a single grid $G_{LR}$ so that one family of the grid lines is used for VFAP$_L$ and another for VFAP$_R$.



vector field V$_L$        vector field V$_R$        curvilinear grid
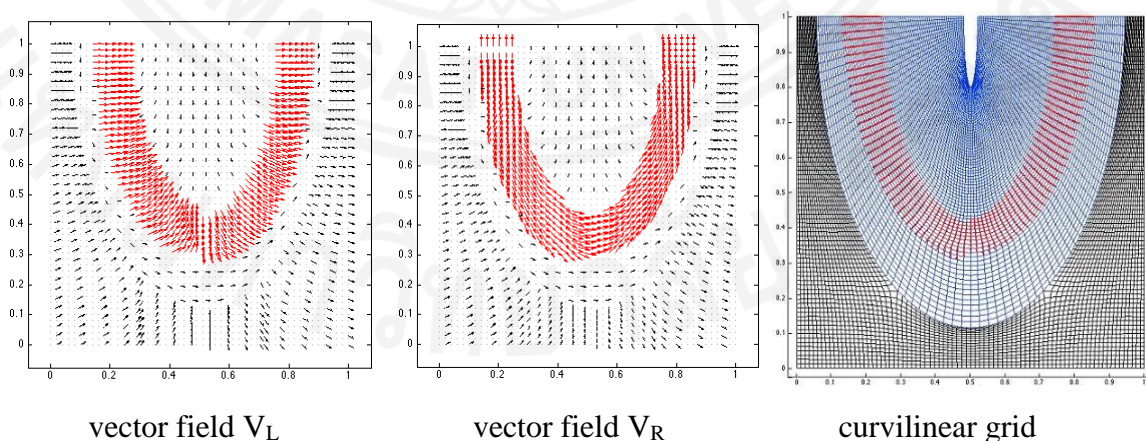
(a) Vector fields V$_L$ and V$_R$ and the composed curvilinear grid $G_{LR}$

(b)  BSFC$_L$, rough cut                    (c)  BSFC$_R$, rough cut



(d)  BSFC$_L$, fine cut                      (e)  BSFC$_R$, fine cut
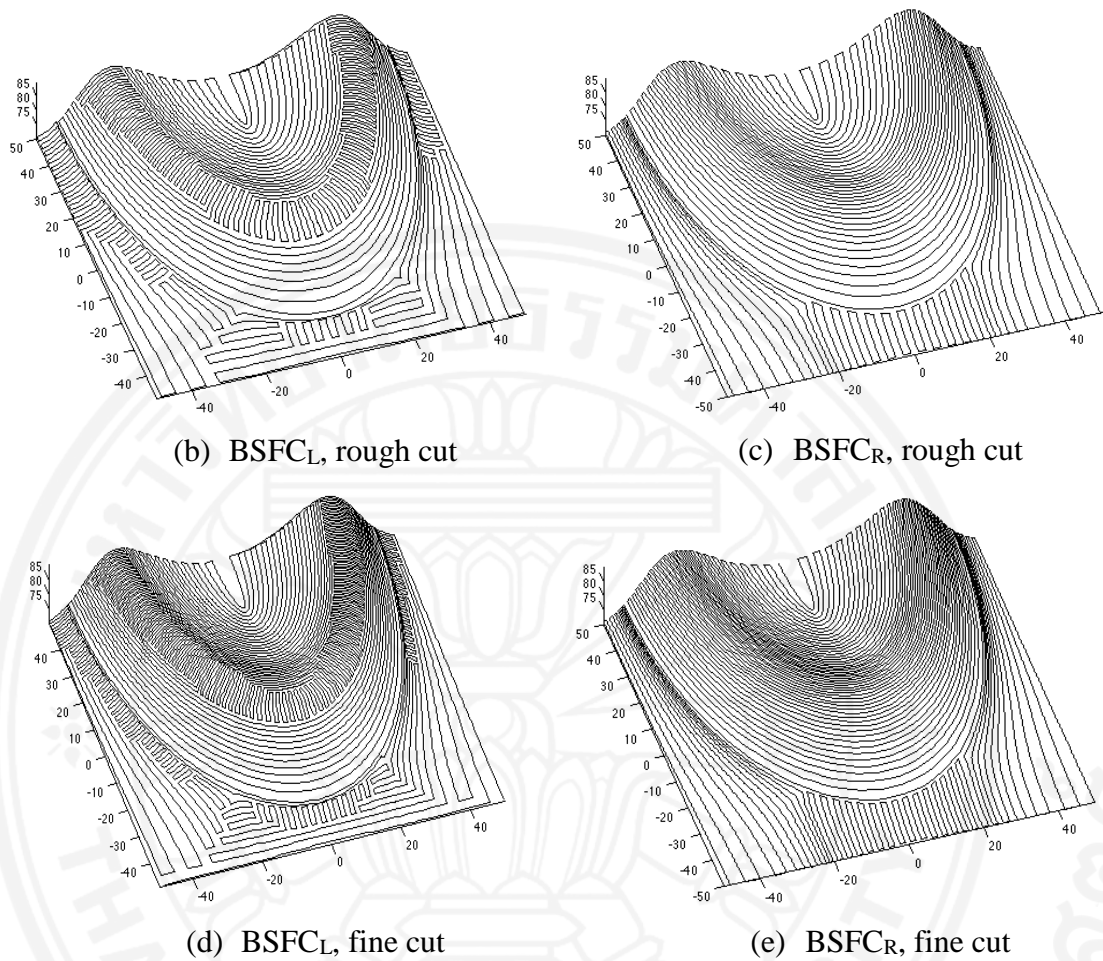
Figure 3.15: VFAP solution for surface 3

The virtual and the real machining are presented in Figure 3.16. The optimized tool path tested against the benchmark algorithms is presented in Table 3.6. The length of VFAP$_L$-path based on the adaptive grid technology is shorter by 7-20%. For instance, when the maximum allowable scallop height $h$=0.05, the length of the tool path is about 2,500 mm shorter. The machining time for the fine cut using VFAP$_R$ has been reduced by 76%. In other words, the proposed method reduces the machining time by (approximately) factor 2.

There is a clear advantage relative to UG. For instance, MAHO 600E for $h$=0.25 the VFAP$_R$ requires 39 min versus 1h42min using UG-FP and 18h57min using UG-HS( see the full evaluation in Table 3.6).

Table 3.7 compares the quality of the proposed method vs. the ISO path in terms of kinematic error and the number of the required CC points.  Clearly, the error stays

within the prescribed limits, whereas the number of the CC points has been drastically reduced for high accuracy milling ($h$=0.1 and $h$=0.01).

Table 3.8 shows the quality of machined surface for the rough and finishing cuts evaluated by the stylus profiling. The rough cut by $VFAP_L$ has slightly better quality compared to ISO zigzag, 7.8 vs. 8.1 µm. Waviness produced by $VFAP_L$ is much lower, 17.8 vs. 31.9. Similarly, the fine cut $VFAP_R$ is characterized by a slightly better quality 7.0 vs. 7.3 µm and the improved waviness: 10.7 vs. 14.0 µm. We hypothesize that the improved waviness is due to a reduced variation of the rotation angles. However, the main advantage of the method is the reduction of the length of the tool path and the machining time while keeping the same quality of the part surface.

Finally, since the proposed trajectory requires iterative calculations, the computational time might be a concern. Therefore, Table 3.9 compares the computational time of the proposed methods with the benchmark algorithms and the machining time. The proposed algorithm implemented in Matlab (some libraries have been compiled from C) works slower than the benchmark methods; however, the computational time is only several minutes. The largest computational time is 10 min for $h$=0.01 (about 10,000 CC points). Note that translating the entire code from Matlab into C usually decreases the computational time by factor 3-10.
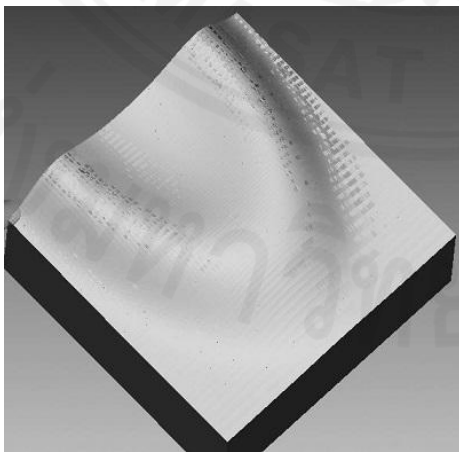


(a) Virtual machining ISO zigzag, rough cut

(b) Real machining, zigzag ISO, rough cut tool path length= 12034.0 mm, time = 2:01:03 hrs
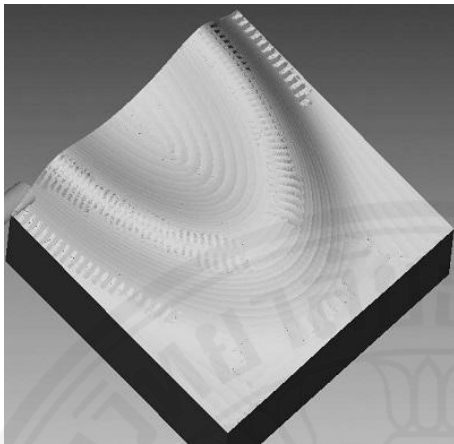
(c) Virtual machining VFAP_L, rough cut
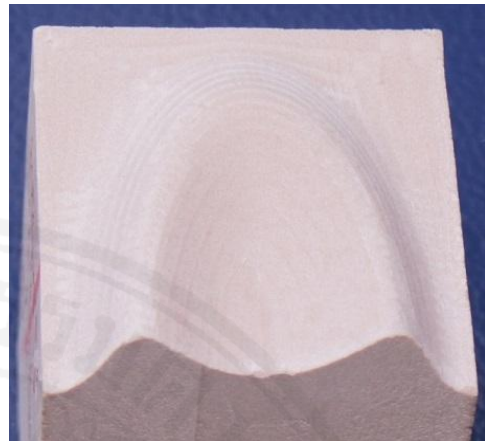
(d) Real machining VFAP_L, rough cut, tool path length = 9545.7 mm (**advantage 20.7%**) time = 1:55:52 hrs (**advantage 4.3%**)
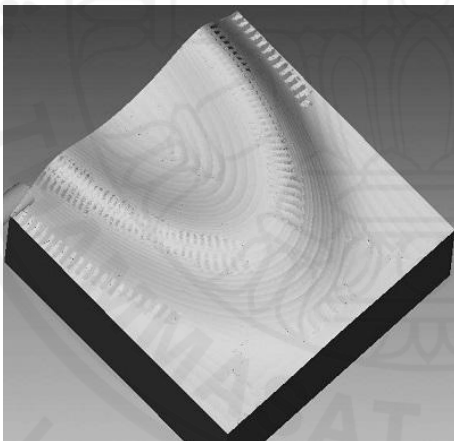


(e) Virtual machining VFAP_R, rough cut

(f) Real machining VFAP_R, rough cut, tool path length = 10075.0 mm (**advantage 16.3%**) time = 0:33:36 hrs (**advantage 72.2%**)
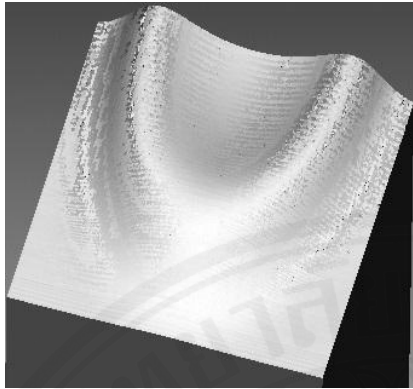
(g) Virtual conventional cut, fine cut
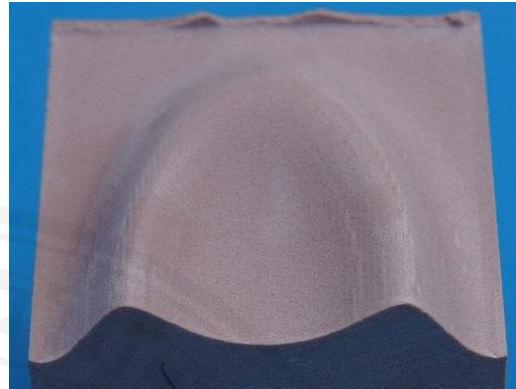
(h) Real machining, zigzag ISO, fine cut tool path length= 26305.0 mm (**advantage 20.9%**), time = 4:27:22 hrs (**advantage 7.1%**)
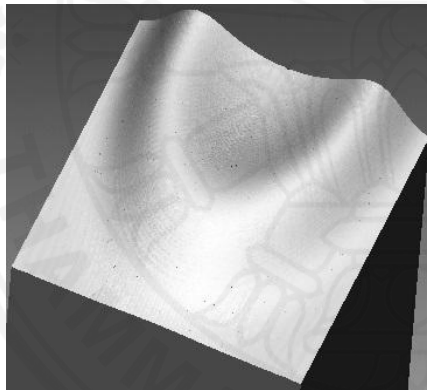


(i) Virtual machining $VFAP_R$, fine cut

(j) Real machining $VFAP_R$, fine cut, tool path length = 22676.7 mm (advantage **13.8%**), time = 1:03:59 hrs (**advantage 76.1%**)

Figure 3.16: VFAP vs. the ISO zigzag

Table 3.6: VFAP vs. conventional tool paths. Surface 3

| Tool radius 4 mm | | | Tool path generation method | | Scallop height(mm) | | | |
|---|---|---|---|---|---|---|---|---|
| | | | | | Roughing | | | Finishing |
| | | | | | 0.25 | 0.1 | 0.05 | 0.01 |
| **Performance** | Tool path length (mm) | | Master CAM | | 35553.0 | 72215.0 | 128879.0 | - |
| | | | UG | HS | 25991.0 | 62825.0 | 125070.0 | 640866.0 |
| | | | | FP | 5480.4 | 8115.6 | 11175.0 | 24150.0 |
| | | | ISO Zigzag | | 5755.2 | 8666.1 | 12034.0 | 26305.0 |
| | | | VFAP$_L$ | | 5336.9 | 7092.7 | 9545.7 | 20819.8 |
| | | | VFAP$_R$ | | 5489.1 | 7601.2 | 10075.0 | 22676.7 |
| | Machining Time | MAHO 600E | UG | HS | 2:03:53.1 | 4:57:21.7 | 9:52:27.2 | 18:57:04.1 |
| | | | | FP | 0:22:15.4 | 0:33:09.6 | 0:46:22.0 | 1:42:32.4 |
| | | | ISO Zigzag | | 0:28:22.1 | 0:43:39.8 | 1:01:03.8 | 2:14:50.2 |
| | | | VFAP$_L$ | | 0:27:14.5 | 0:41:20.4 | 0:56:19.7 | 2:00:41.2 |
| | | | VFAP$_R$ | | 0:10:25.4 | 0:14:21.7 | 0:19:22.9 | 0:39:19.1 |
| | | HAAS VF2TR | UG | HS | 3:26:00.6 | 8:13:54.1 | 16:22:50.4 | 29:54:09.1 |
| | | | | FP | 0:45:04.7 | 1:07:20.4 | 1:33:35.8 | 3:24:28.2 |
| | | | ISO Zigzag | | 0:56:13.9 | 1:26:37.5 | 2:01:03.5 | 4:27:22.0 |
| | | | VFAP$_L$ | | 0:55:09.7 | 1:24:21.2 | 1:55:52.1 | 4:08:22.3 |
| | | | VFAP$_R$ | | 0:17:46.1 | 0:24:56.1 | 0:33:36.1 | 1:03:58.7 |
| **Advantage rel. to ISO** | Tool path length (mm) | | VFAP$_L$ | | 7.3% | 18.2% | **20.7%** | **20.9%** |
| | | | VFAP$_R$ | | 4.6% | 12.3% | 16.3% | 13.8% |
| | Machining Time | MAHO 600E | VFAP$_L$ | | 4.0% | 5.3% | 7.8% | 10.5% |
| | | | VFAP$_R$ | | 63.3% | 67.1% | 68.3% | 70.8% |
| | | HAAS VF2TR | VFAP$_L$ | | 1.9% | 2.6% | 4.3% | 7.1% |
| | | | VFAP$_R$ | | 68.4% | 71.2% | **72.2%** | **76.1%** |

Table 3.7: Kinematic error. VFAP vs. conventional tool paths. Surface 3

| | | | Hausdorff distance | | | | | | | | | | | |
| --- | --- | --- | --- | --- | --- | --- | --- | --- | --- | --- | --- | --- | --- | --- |
| Tool path generation method | | | Roughing | | | | | | | | | Finishing | | |
| | | | h=0.25 | | | h=0.10 | | | h=0.05 | | | h=0.01 | | |
| | | | #CC | Ave | Std | #CC | Ave | Std | #CC | Ave | Std | #CC | Ave | Std |
| MAHO 600E | UG | HS | 3806 | **0.040** | 0.059 | 19262 | 0.025 | 0.024 | 62482 | 0.017 | 0.012 | 210745 | 0.005 | 0.003 |
| | | FP | **1663** | 0.040 | 0.054 | 7152 | 0.026 | 0.024 | 14921 | 0.019 | 0.014 | 57320 | 0.005 | 0.003 |
| | ISO Zigzag | | 5047 | 0.064 | 0.063 | 9334 | 0.038 | 0.025 | 16652 | 0.022 | 0.012 | 68889 | 0.005 | 0.002 |
| | VFAP$_L$ | | 4059 | 0.054 | 0.002 | 9059 | **0.022** | 0.025 | 16773 | 0.012 | 0.013 | 65186 | 0.003 | 0.002 |
| | VFAP$_R$ | | 5374 | 0.009 | 0.004 | **7151** | 0.009 | 0.001 | **9331** | **0.009** | 0.001 | **29288** | **0.003** | 0.001 |
| HASS VF2TR | UG | HS | 6295 | 0.053 | 0.062 | 29996 | 0.032 | 0.026 | 102859 | 0.019 | 0.012 | 312345 | 0.005 | 0.002 |
| | | FP | **3406** | 0.053 | 0.062 | **7091** | 0.033 | 0.028 | 18016 | 0.019 | 0.013 | 95136 | 0.005 | 0.002 |
| | ISO Zigzag | | 5882 | 0.082 | 0.064 | 10299 | 0.040 | 0.024 | 18603 | 0.023 | 0.012 | 83202 | 0.005 | 0.002 |
| | VFAP$_L$ | | 4321 | 0.065 | 0.006 | 9418 | 0.025 | 0.026 | 17437 | 0.013 | 0.013 | 68075 | **0.003** | 0.002 |
| | VFAP$_R$ | | 5378 | **0.013** | 0.010 | 7157 | **0.013** | 0.008 | **9625** | **0.011** | 0.004 | **32515** | 0.004 | 0.001 |

Table 3.8: Roughness and Waviness of VFAP-BSFC vs. conventional tool paths
Surface 3

| | Roughness $R_a$ ($\mu$m) | | | Standard Deviation | | | Waviness ($\mu$m) | | | Standard Deviation | | |
| --- | --- | --- | --- | --- | --- | --- | --- | --- | --- | --- | --- | --- |
| Machining Stage | ISO Zigzag | VFAP$_L$ | VFAP$_R$ | ISO Zigzag | VFAP$_L$ | VFAP$_R$ | ISO Zigzag | VFAP$_L$ | VFAP$_R$ | ISO Zigzag | VFAP$_L$ | VFAP$_R$ |
| Rough Cut | 8.1 | 7.8 | **6.8** | 10.5 | 8.1 | **3.1** | 31.9 | 17.8 | 12.2 | 7.5 | 6.2 | **1.5** |
| Finishing | 7.3 | / | 7.1 | 10.2 | / | 9.1 | 14.0 | / | 10.7 | 4.1 | / | 0.7 |

Table 3.9:  Computational time vs. the machining time

| Test | Scallop Height (mm) | Computational Time (min) | | | | | Machining Time (min) | | | |
| | | Master Cam | UG | | Matlab/C | | MAHO 600E | | HASS VF2TR | |
| | | Zigzag | HS | FP | Zigzag | VFAP | Zigzag | VFAP | Zigzag | VFAP |
| Surface 1 | 0.25 | 1 | 1 | 1 | 1 | 3 | 28 | 18 | 45 | 33 |
| | 0.10 | 1 | 8 | 2 | 1 | 4 | 44 | 28 | 72 | 52 |
| | 0.05 | 1 | 30 | 2 | 1 | 5 | 64 | 40 | 103 | 74 |
| Surface 2 | 0.25 | 1 | 1 | 1 | 1 | 6 | 8 | 6 | 33 | 26 |
| | 0.10 | 1 | 1 | 1 | 1 | 8 | 12 | 9 | 53 | 41 |
| | 0.05 | 1 | 3 | 1 | 1 | 10 | 17 | 13 | 75 | 56 |
| Surface 3 | 0.25 | 1 | 1 | 1 | 1 | 2 | 28 | 10 | 56 | 17 |
| | 0.10 | 1 | 3 | 1 | 1 | 2 | 43 | 14 | 86 | 24 |
| | 0.05 | 1 | 27 | 1 | 1 | 2 | 61 | 19 | 121 | 33 |
| | 0.01 | 1 | 54 | 1 | 1 | 2 | 134 | 39 | 267 | 63 |

# Chapter 4
# Adaptive Curvilinear Toolpath

## 4.1    Adaptive Curvilinear Toolpath (ACT) Framework

An important practical application of the toolpath generation methods is machining surfaces represented by the STL format. In order to apply adaptive curvilinear toolpath (ACT) to the STL we have to either adapt the algorithms to the 3D case or flatten the STL surface and generate the required curvilinear grid in the resulting parametric domain. Note that meshing algorithms in 2D are more efficient than in 3D [167]; therefore, we incorporate a "radial plane" flattening approach into the proposed framework (see a short survey in the section 4.2 Flattening Algorithm).

Our methodology includes the following components:
- Flattening.
- Evaluation of the surface characteristics in the parametric domain.
- Grid generation in the parametric domain.
  - o    Boundary fitted grids
  - o    Different types of grids such as the C-grid, O-grid, H-grid [168].
  - o    Grids adapted to control functions: scalar functions, vector fields
- Space filling curves
  - o    Adaptive space filling curves.
  - o    Biased space filling curves.

The methodology has been tested on a variety of STL surfaces including surfaces with multiple ridges, human masks as well as dental crowns or even tooth implants represented by the STL files. In particular, we demonstrate the efficiency of the algorithms by machining all types of human teeth: molars, premolars, canine and incisors.

The proposed tools have been tested against the standard ISO path, MasterCam generated path and advanced toolpath generation methods of NX9. The experiments show that there is no universal sequence of steps applicable to every surface.

However, the tools available within the ACT-framework are capable of substantially improving the quality of the toolpath in terms of its length and the machining time.

In the context of the grid generation technologies the Cartesian grids include H-grid, O-grid and C- grid (see Figure 4.1). We will show the premolar, molar and canine STL models can be produced using the O-grid for a shorter time using a shorter tool path.
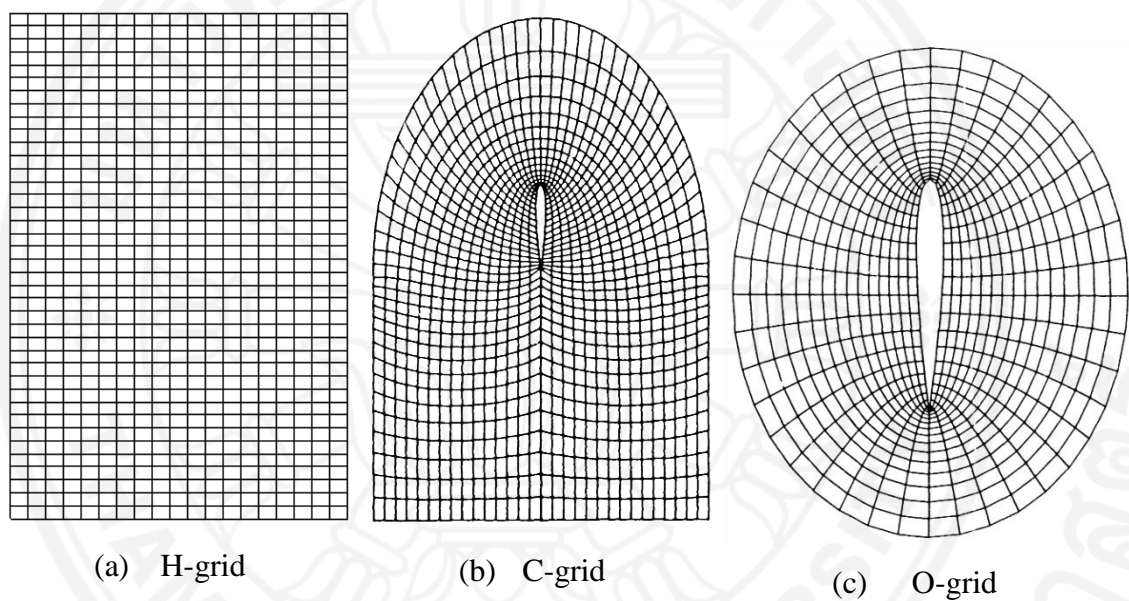


(a)    H-grid                    (b)    C-grid                    (c)    O-grid

Figure 4.1: H-grid, O-grid and C-grid [169]

## 4.2    Flattening Algorithm

The majority of toolpath generation techniques have been demonstrated on a single parametric surface such as the Bezier patch, Gregory patch, B-spline, etc. However, the explicit parametric representation is rarely used in the industry. The most popular formats are STL [170], IGES [171], STEP [172], as well as SET [173], CATIA [174] and PHIGS [175]. The STL format, which approximates the surface of a solid model by triangles, is becoming the standard for the rapid prototyping industry and is increasingly popular in multi-axis manufacturing. The main reason is simplicity and applicability to an arbitrary surface.

The algorithms for flattening triangulated or tessellated surfaces have been used in many research areas such as generation of clothing patterns, 3D reconstruction, texture mapping reconstruction, multi-resolution analysis, formation of ship hulls, metal forming, etc. By flattening we understand a one-to-one mapping of the STL surface to a planar domain in the parametric space. Geometrically, the flattening algorithm unfolds the surface onto a plane without self-intersections, that is, each point of the original surface is associated with a unique point $(u,v)$ in the parametric space.

A variety of algorithms have been proposed for parameterization of the triangulated surfaces. Marcum [176] introduces the use of finite-element techniques to compute the locations of the flat mesh nodes. The method uses an iterative procedure where the boundary and interior are recomputed in separate consecutive steps. Eck et al. [177] suggest a method based on the harmonic maps. Floater [178] introduces a parameterization based on convex combinations and considering the triangulated surface as a simply-connected plane graph. Sheffer and Sturler [179] defines the flattening problem as optimization constrained with regard to the angles of the flat triangles. McCartney et al. [180] minimizes the strain energy required to deform the edges of the triangular mesh. This approach is combined with an original method of arbitrarily siting darts or gussets to assist in the fitting process. The minimization of the strain energy/string model is used by Y. Zhong, B. Xu [181] and J. Xu and C. Jin [182]. However, despite computational complexity and high computational cost, none of the proposed methods guarantee the validity of the resulting flat mesh. On the other hand, the simplicity and fast execution of the geometrical slicing methods have often been overlooked. Besides, the slicing methods do not require boundary conditions which (in case of the energy minimization) must be set up manually.

In this dissertation, the radial plane flattening is proposed and demonstrated for a particular practical case of STL surfaces representing the human teeth. The method was also successfully tested on parts which can be roughly approximated by surfaces having radial symmetry. Note that this approximation could be very far from ideal (see the human face example); however, the radial flattening still works better than some general commercial software (see Figure 4.2). Also, the proposed algorithm

preserves distances along the trajectories in the radial planes and reduces angular and metric distortions in the proximity of the focus point [183].

A polar coordinate system centered is defined at a point of reference $O_p$. Given the surface's tangential plane at the reference point, a perpendicular plane through the reference point and an arbitrary STL point $S'$. The method evaluates the trajectory connecting $O_p$ and $S'$ on the surface by finding intersections of the radial plane and the corresponding STL triangles (Figure 4.2).

The technique requires solving a large series of linear (possibly singular) systems 2x2 and 3x3 and a special tracing procedure to connect the intersection points.

The new coordinates $(s, \theta)$ are the length of the trajectory $O_p S'$ and the angle between the radial plane and the reference plane, respectively (Figure 4.2). Note that the radial flattening does not necessarily mean that the curvilinear grid must be polar. As a matter of fact, we map the resulting triangles onto the Cartesian plane. However, using a polar parametrization and the spiral toolpath is a feasible option which can be implemented by the ACT. Figure 4.3 compares the proposed algorithm with MeshFlatten [184].
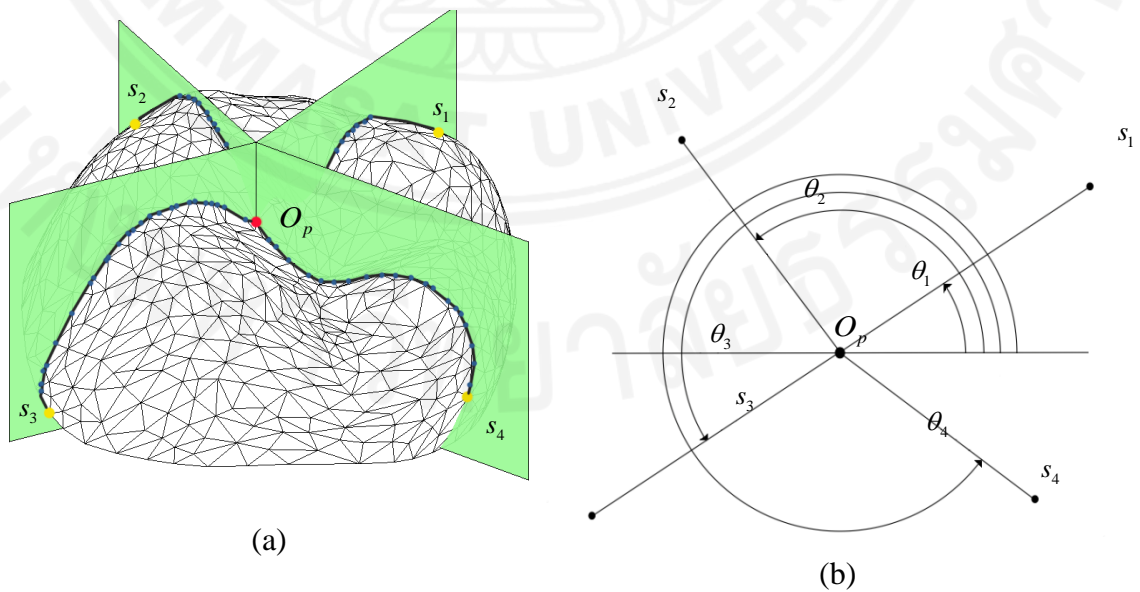


(a)

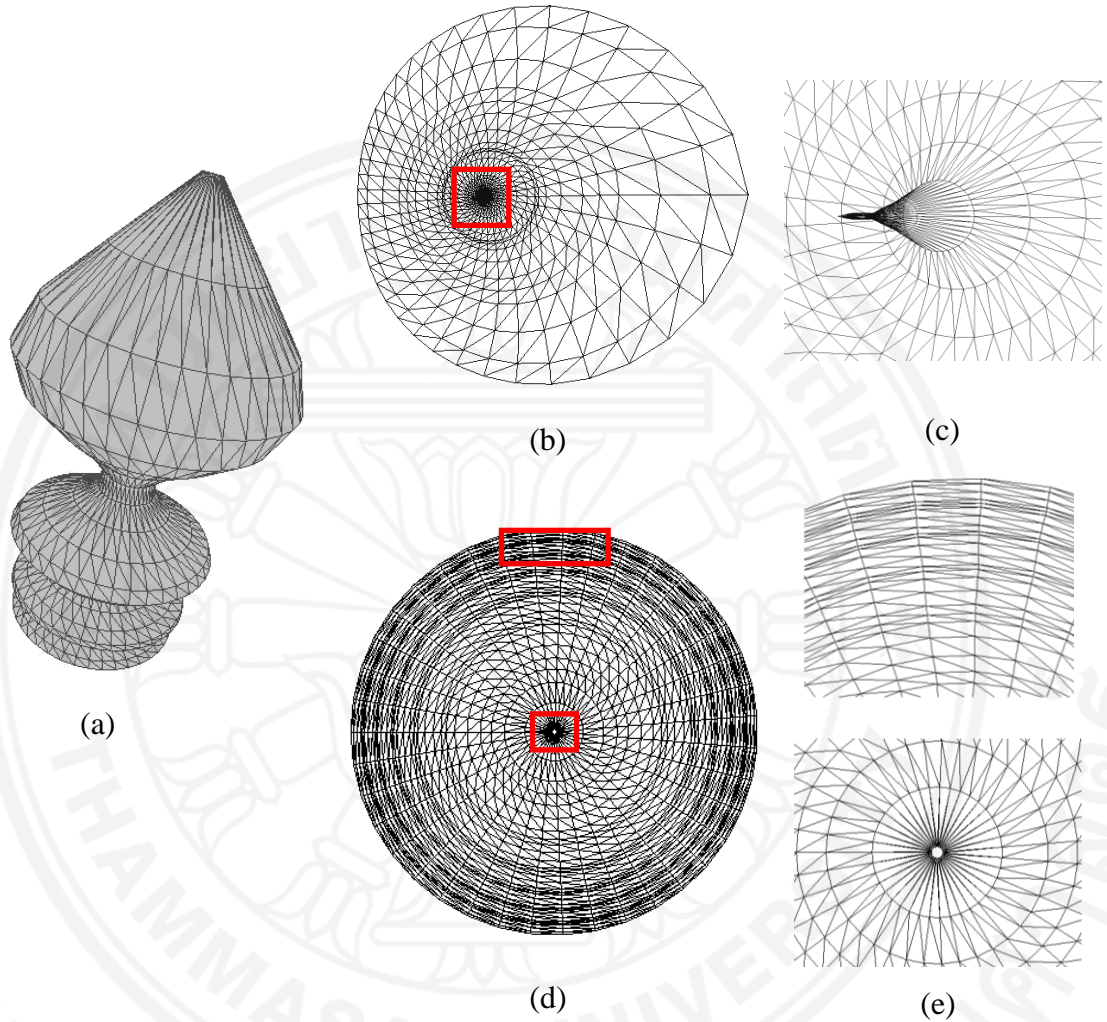(b)

Figure 4.2: Radial plane flattening algorithm

Figure 4.3: Flattening (a) 3D Model (b)-(c) MeshFlatten, (d)-(e) radial plane flattening

Clearly, MeshFlatten fails to return an acceptable parametrization whereas a correct choice of the reference point $O_p$ allows construction of the required flattening using the radial plane approach.

The surface normal and the curvature required by the toolpath generation methods are evaluated using a modification of an algorithm [185] for finding per-vertex characteristics by averaging adjacent per-face characteristics. The per-face computation of the curvature is based on the second fundamental tensor given by

74

$$\text{II} \equiv \begin{pmatrix} e & f \\ f & g \end{pmatrix} = \begin{pmatrix} \dfrac{\partial n}{\partial u'} u' & \dfrac{\partial n}{\partial v'} u' \\ \dfrac{\partial n}{\partial u'} v' & \dfrac{\partial n}{\partial v'} v' \end{pmatrix},$$

(4.1)

,

where $u', v'$ are the directions of the orthonormal coordinate system in the plane tangent to the surface. Given an arbitrary STL triangle (Figure 4.4) we approximate the second fundamental tensor as follows
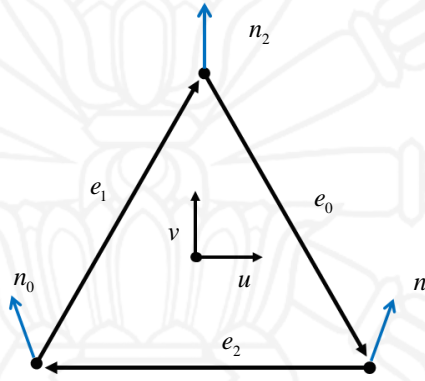


Figure 4.4: Estimation of the curvature tensor on the STL surface

$$\text{II} \begin{pmatrix} e_0 u' \\ e_0 v' \end{pmatrix} = \begin{pmatrix} u(n_2 - n_1) \\ v(n_2 - n_1) \end{pmatrix}, \text{II} \begin{pmatrix} e_1 u' \\ e_1 v' \end{pmatrix} = \begin{pmatrix} u(n_0 - n_2) \\ v(n_0 - n_2) \end{pmatrix}, \text{II} \begin{pmatrix} e_2 u' \\ e_2 v' \end{pmatrix} = \begin{pmatrix} u(n_1 - n_0) \\ v(n_1 - n_0) \end{pmatrix}.$$

(4.2)

Next, the equations above are used in the least square approximation to find $e$, $f$ and $g$. Furthermore, given the curvature tensor in the coordinate system of the face, we evaluate the curvature at an arbitrary point inside the triangle in a direction $d'$ as

$$k' = d' \, \text{II} \, d'.$$

(4.3)

The curvature at the vertices is accumulated using weighting relative to the corresponding "Voronoi area", the portion of the area closest to the prescribed vertex.

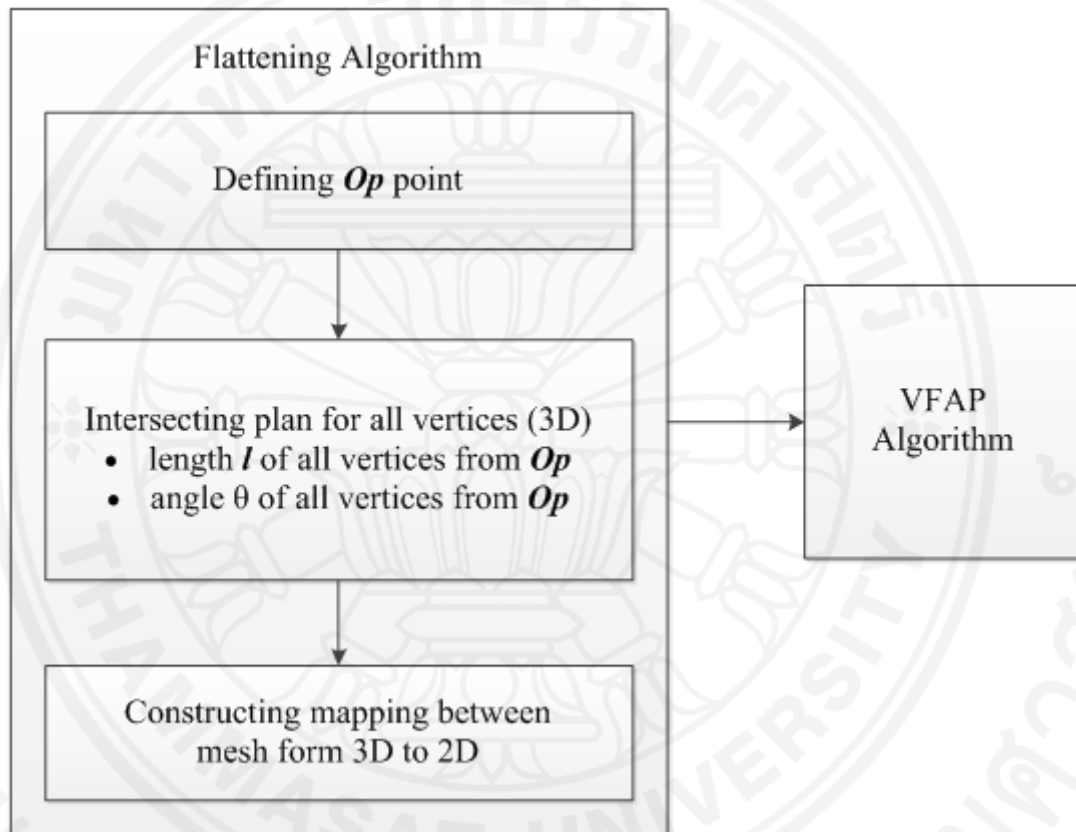Figure 4.5 demonstrates the diagram of flattening algorithm described above.



Figure 4.5: Flattening algorithm

## 4.3 Experiments

The ACT is applied to STL toolpath generation. The numerical technology has been tested against the standard ISO as well as against MasterCam and advanced toolpath algorithms   Helical/Spiral (HS) and Follow Periphery (FP) of NX9 (formerly UG). All surfaces have been machined using a flat end cutter. The experiments have been performed for MAHO-600E and HAAS VF2TR.

Recall that the ACT- approach includes

- Flattening (parametrization)
- Cost function (vector field generation)
- Decomposition into sub-surfaces
- Selection of the grid type (H-grid, O-grid, C-grid)
- Grid generation (boundary fitted, adaptation to a cost function, adaptation to a vector field)
- Toolpath generation (ISO,  spiral, adaptive space filling curve, biased space filling curve)

The grid alignment is based on cost functions representing the material removal rate and the toolpath length. We will denote these options by subscripts $R$ and $L$ respectively, for instance $VFAG_R$ and $VFAG_L$.

### 4.3.1 Example 1 Surface decomposition and ACT for a synthetic dental surface

A surface in Figure 4.6(a) is characterized by a ridge nearby the boundary. We adopted this shape from the dental milling, where the elevated part represents the ridges of a dental crown or implant [166].  The size of the workpiece is 100x100 mm. The surface was designed using MasterCam, then converted into the STL format (Figure 4.6 (a)) and flattened using the proposed radial plane approach (Figure 4.7 (b)).

The VFAG for such surfaces can be efficiently generated in subregions obtained automatically or manually. Clearly,  the surface is composed of a flat region and a region characterized by a high curvature. The high curvature narrows the machining

strip, whereas inside the flat area the tool can cut the material using the maximum machining strip.

The optimal directions corresponding to the material removal rate and machining strip width respectively in Figure 4.6 (c) and (d) show that it is possible to construct a single grid such that one family of the grid lines is adapted to $V_R$ and another to $V_L$.

Consider the case when the user requires a minimal tool path for the rough cut to reduce the tool wear and the minimal time for the fine cut. The generated VFAG in Figure 4.6 (e) accomplishes both tasks. The rough machining is performed along the direction of the highest curvature in order to maximize the machining strip ($ACT_L$). The finishing strategy employs $ACT_R$ to maximize the material removal rate and to reduce the machining time. In this case, most of the time the tool moves along the direction of the minimal curvature. Note that a boundary fitted grid in Figure 4.6 (f) was used as the initial approximation for VFAGs. The toolpaths constructed by BSFC are shown in Figure 4.6(g) and (h). Clearly, the two cost functions generate very different toolpaths. The virtual and real machining results are illustrated in Figure 4.6 (i)-(l).

The performance of ACT in terms of the length of the toolpath and the machining time is summarized in Table 4.1. The table clearly demonstrates the advantages of $ACT_L$ and $ACT_R$ for varying scallop height. The benchmark methods are the regular ISO, MasterCam and advanced algorithms HS and FP of NX9.

Compared to ISO, the length of $ACT_L$-path is shorter by 7-20%. For instance, when the maximum allowable scallop height $h$=0.01, the length of the tool path is about 2,500 mm shorter while the entire ISO is approximately 12000mm. The machining time for the fine cut using $ACT_R$ has been reduced by 76%. In other words, the proposed method reduces the machining time by (approximately) factor 2. There is a clear advantage relative to NX9. For instance, on MAHO 600E for $h$=0.01 the $ACT_R$ requires 19 min versus 46 min using FP and 9h52min using HS (see the entire evaluation in Table 4.1.

Table 4.2 compares the quality of the proposed method vs. ISO in terms of the average kinematic error $\bar{\varepsilon}$, the corresponding standard deviation $\sigma_\varepsilon$ and the number of the required CC points $N_{CC}$. Clearly, the error stays within the prescribed limits, whereas the number of the CC points has been reduced. For instance, for HAAS VF-2TR $N_{CC,ISO} = 18603$, $N_{CC,R} = 9625$, $N_{CC,L} = 17437$.

Table 4.3 shows the quality of the produced surface for the rough and finishing cuts evaluated by the stylus profiling [163]. The surface profile obtained by a high-resolution probe is post processed by the Gaussian filter [164]. Twenty sample profiles were measured with the standard cutoff of 0.8 mm [164]. Roughness of the machined surface is within the acceptable range for surface milling operations [165]. The rough cut by $ACT_L$ has a better quality compared to ISO, that is, roughness: 7.8 vs. 8.1 μm and waviness 17.8 vs. 31.9. We hypothesize that the major improvement in waviness is due to a reduced variation of the rotation angles which are implicitly included in the evaluation of the material removal rate since maximization of the removal rate leads to the reduction in the angular distance between the CC points.



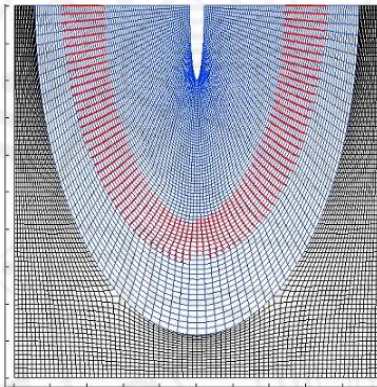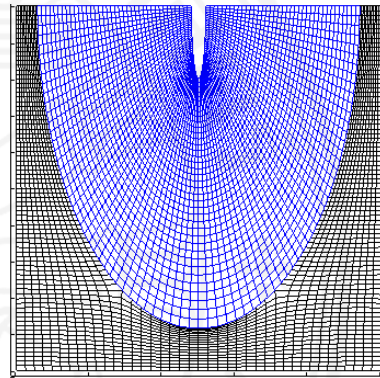| (a) | Synthetic dental surface | (b) | Flattened surface |
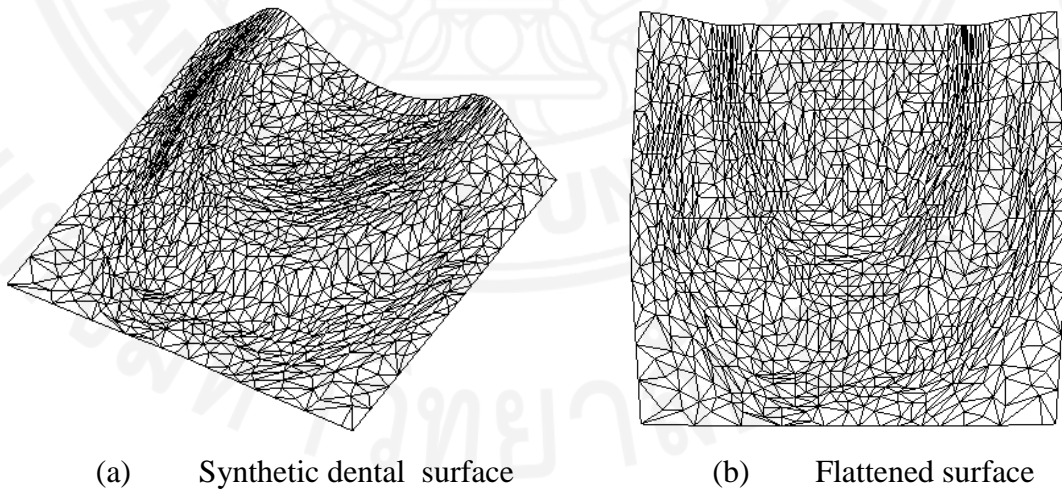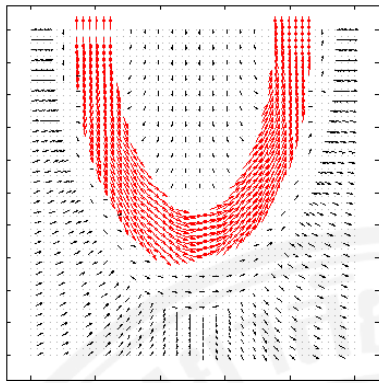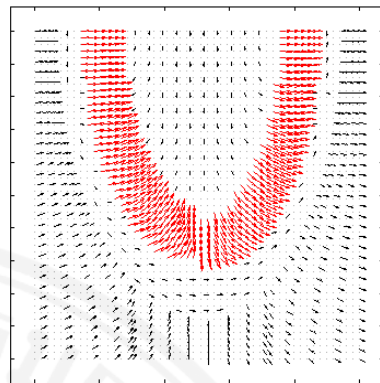
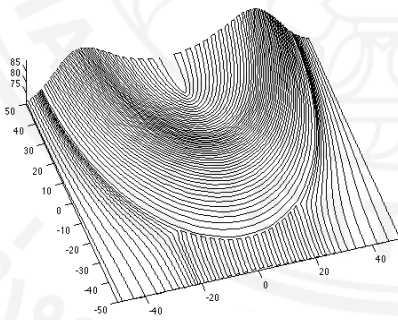(c)    $V_R$                        (d)    Vector field $V_L$
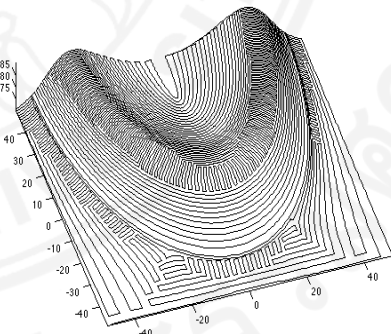
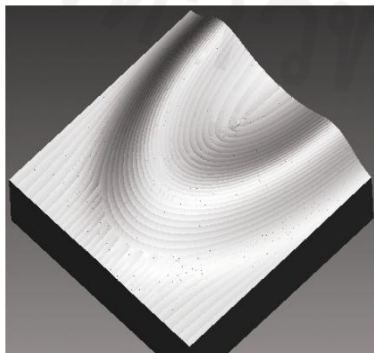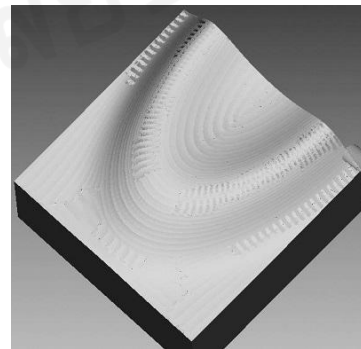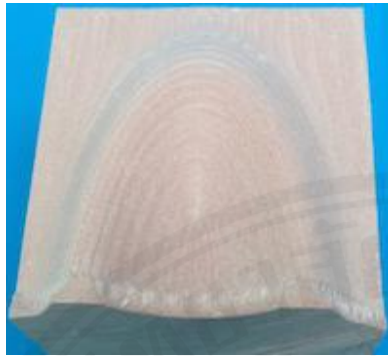(e)   VFAG                      (f)      Boundary fitted grid

(g)    $ACT_R$                    (h)    $ACT_L$

(i)    Virtual $ACT_R$             (j)    Virtual $ACT_L$
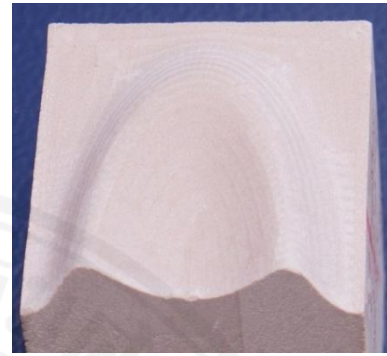
|            (k)           Machining by $ACT_R$            |            (l)           Machining by $ACT_L$            |

Figure 4.6: Synthetic (ridge-cusp) dental surface

Table 4.1: Synthetic dental surface: ACT vs. the reference methods

| Toolpath Generation Methods | | | Scallop Height h (mm) | | |
|---|---|---|---|---|---|
| | | | 0.25 | 0.10 | 0.05 |
| **Performance** | Toolpath Length (mm) | Master CAM | 35553.0 | 72215.0 | 128879.0 |
| | | HS | 25991.0 | 62825.0 | 125070.0 |
| | | FP | 5480.4 | 8115.6 | 11175.0 |
| | | ISO | 5755.2 | 8666.1 | 12034.0 |
| | | $ACT_R$ | 5489.1 | 7601.2 | 10075.0 |
| | | $ACT_L$ | 5336.9 | 7092.7 | 9545.7 |
| | Machining Time / HAAS VF2TR | HS | 3:26:00.6 | 8:13:54.1 | 16:22:50.4 |
| | | FP | 0:45:04.7 | 1:07:20.4 | 1:33:35.8 |
| | | ISO | 0:56:13.9 | 1:26:37.5 | 2:01:03.5 |
| | | $ACT_R$ | 0:17:46.1 | 0:24:56.1 | 0:33:36.1 |
| | | $ACT_L$ | 0:55:09.7 | 1:24:21.2 | 1:55:52.1 |
| | MAHO 600E | HS | 2:03:53.1 | 4:57:21.7 | 9:52:27.2 |
| | | FP | 0:22:15.4 | 0:33:09.6 | 0:46:22.0 |
| | | ISO | 0:28:22.1 | 0:43:39.8 | 1:01:03.8 |
| | | $ACT_R$ | 0:10:25.4 | 0:14:21.7 | 0:19:22.9 |
| | | $ACT_L$ | 0:27:14.5 | 0:41:20.4 | 0:56:19.7 |
| **Advantage rel. to ISO** | Toolpath Length (mm) | $ACT_R$ | 4.6% | 12.3% | 16.3% |
| | | $ACT_L$ | 7.3% | 18.2% | 20.7% |
| | Machining Time / HAAS VF2TR | $ACT_R$ | 68.4% | 71.2% | 72.2% |
| | | $ACT_L$ | 1.9% | 2.6% | 4.3% |
| | MAHO 600E | $ACT_R$ | 63.3% | 67.1% | 68.3% |
| | | $ACT_L$ | 4.0% | 5.3% | 7.8% |

81

Table 4.2: Synthetic dental surface: CC points, kinematic error, ACT vs. ISO

| Toolpath Generation techniques | HAAS VF-2TR | | | | | | | | | MAHO 600-E | | | | | | | | |
|---|---|---|---|---|---|---|---|---|---|---|---|---|---|---|---|---|---|---|
| | h=0.25 mm | | | h=0.10 mm | | | h=0.05 mm | | | h=0.25 mm | | | h=0.10 mm | | | h=0.05 mm | | |
| | $N_{CC}$ | $\bar{\varepsilon}$ | $\sigma_\varepsilon$ | $N_{CC}$ | $\bar{\varepsilon}$ | $\sigma_\varepsilon$ | $N_{CC}$ | $\bar{\varepsilon}$ | $\sigma_\varepsilon$ | $N_{CC}$ | $\bar{\varepsilon}$ | $\sigma_\varepsilon$ | $N_{CC}$ | $\bar{\varepsilon}$ | $\sigma_\varepsilon$ | $N_{CC}$ | $\bar{\varepsilon}$ | $\sigma_\varepsilon$ |
| ISO | 5882 | 0.082 | 0.064 | 10299 | 0.040 | 0.024 | 18603 | 0.023 | 0.012 | 5047 | 0.064 | 0.063 | 9334 | 0.038 | 0.025 | 16652 | 0.022 | 0.012 |
| $ACT_R$ | 5378 | 0.013 | 0.010 | 7157 | 0.013 | 0.008 | 9625 | 0.011 | 0.004 | 5374 | 0.009 | 0.004 | 7151 | 0.009 | 0.001 | 9331 | 0.009 | 0.001 |
| $ACT_L$ | 4321 | 0.065 | 0.006 | 9418 | 0.025 | 0.026 | 17437 | 0.013 | 0.013 | 4059 | 0.054 | 0.002 | 9059 | 0.022 | 0.025 | 16773 | 0.012 | 0.013 |

Table 4.3: Synthetic dental surface: roughness and waviness, ACT vs. ISO

| Roughness $R_a$ ($\mu$m) | | | Standard Deviation | | | Waviness $R_a$ | | | Standard Deviation | | |
|---|---|---|---|---|---|---|---|---|---|---|---|
| ISO | $ACT_R$ | $ACT_L$ | ISO | $ACT_R$ | $ACT_L$ | ISO | $ACT_R$ | $ACT_L$ | ISO | $ACT_R$ | $ACT_L$ |
| 8.1 | 6.8 | 7.8 | 10.5 | 3.1 | 8.1 | 31.9 | 12.2 | 17.8 | 7.5 | 1.5 | 6.2 |

## 4.3.2 Example 2 Dual vector field on a single Cartesian grid STL model of the human face mask

The ACT applied to the surface from Example 1 employs decomposition techniques to achieve the best alignment with the vector field. However, certain surfaces allow for a decomposition of the vector field $V(u,v)$ into a dual vector field $V_D(u,v) = (\alpha(u,v), \beta(u,v))$ and adaptation of the two families of the coordinate curves to $\alpha(u,v)$ and $\beta(u,v)$, respectively within a single parametric region.

We apply these techniques to an STL model of the human face mask in Figure 4.7 (a) and (b). The two families of vector fields shown in Figure 4.7 (c) and (d) are obtained using $V_R$ while Figure 4.7 (e) and (f) show the vector field obtained using $V_L$. The VFAGs are presented in Figure 4.7 (g) and (h). The particular cost function affects BSFCs displayed in Figure 4.7 (i) and (j). Virtual and real machining using the regular ISO and $ACT_R$ are presented in Figure 4.7 (k) - (m) and Figure 4.7 (l) - (n), respectively.

Table 4.4 presents the performance of the ACT against the benchmark toolpath generation methods shows the advantages of the proposed framework. $ACT_L$ is shorter by 17% and $ATC_R$ is faster by 13% compared to ISO. Note that the real industrial parts require thousands of hours of costly machine operations and qualified technicians. Therefore, the advantage of 13-17% is financially and technically sound. Besides, the example shows that even for a very complicated surface and seemingly chaotic  vector field the ACT based on a single VFAG can lead to important improvements (our next example shows that those improvements could be even more tangible). Table 4.5 shows that the efficiency of the ACT measured by the number of the required CC increases, whereas the average kinematic error practically does not change.  Finally, Table 4.6 displaying the roughness and waviness of the machined surface measured by stylus profiling shows the advantages of ACT.



(a)  Human mask          (b)  Flattened human mask
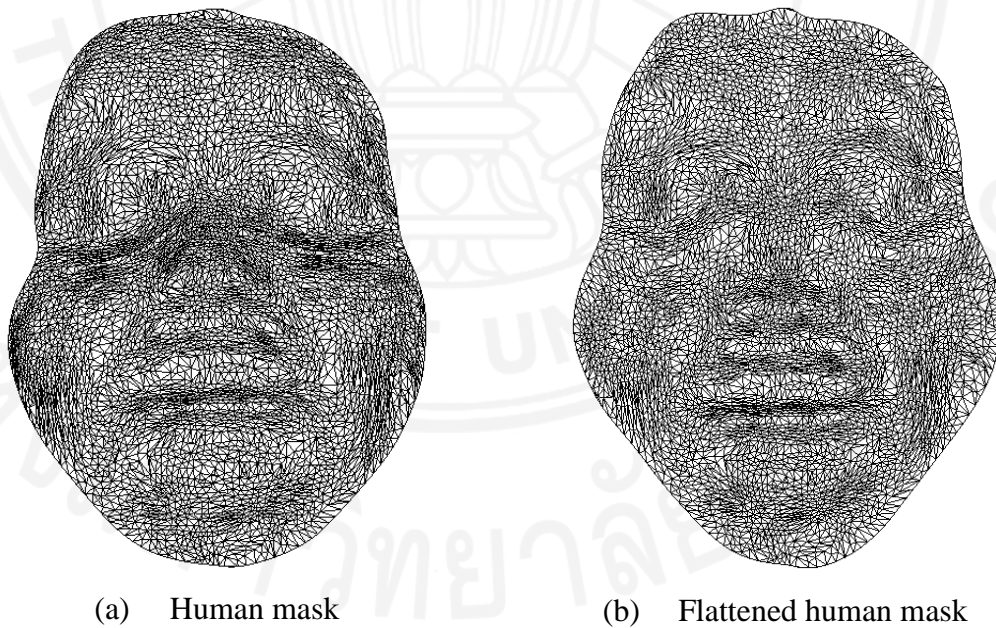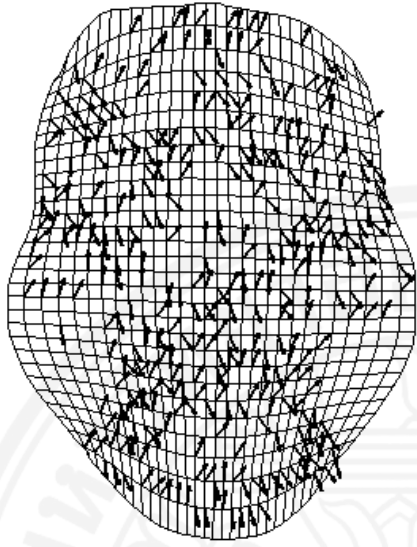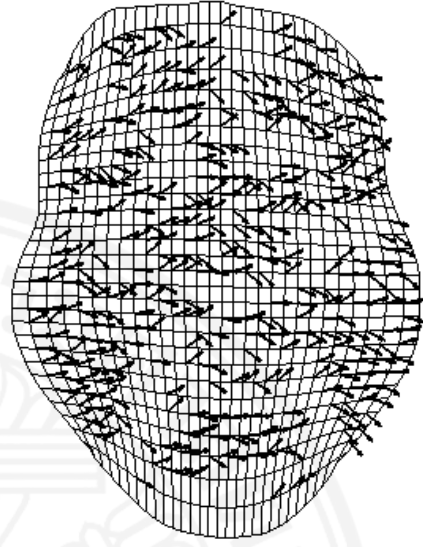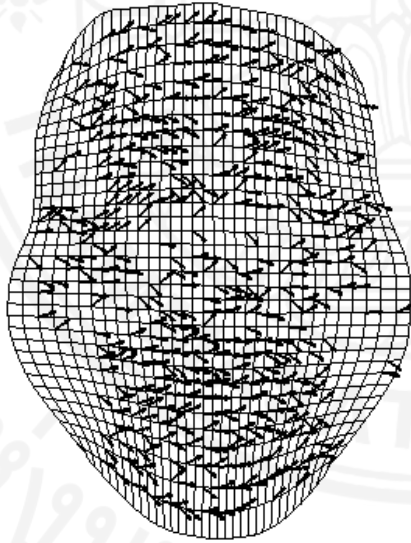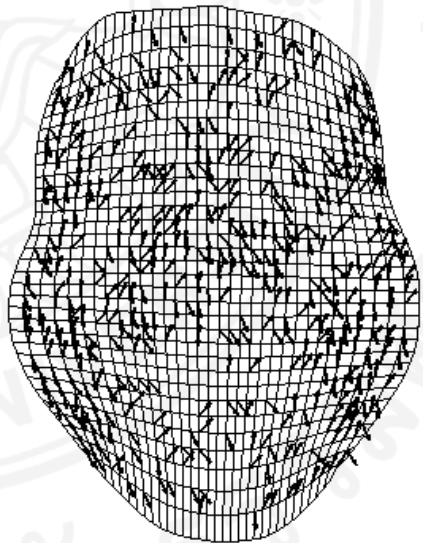
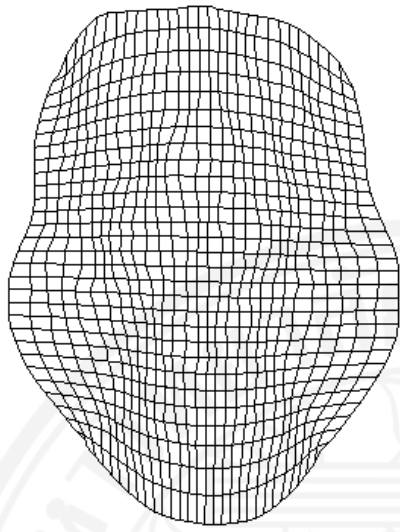(c)    $\alpha_R(u,v)$                           (d)    $\beta_R(u,v)$
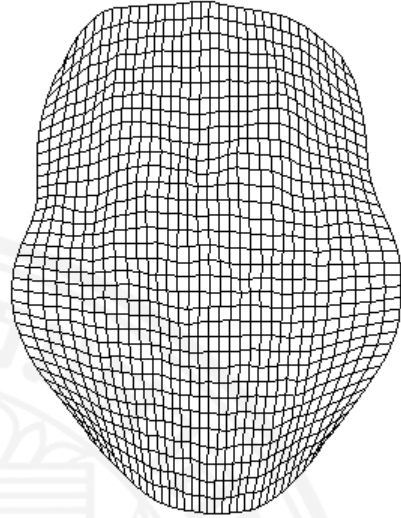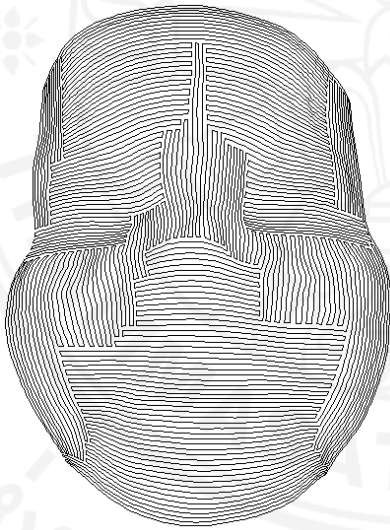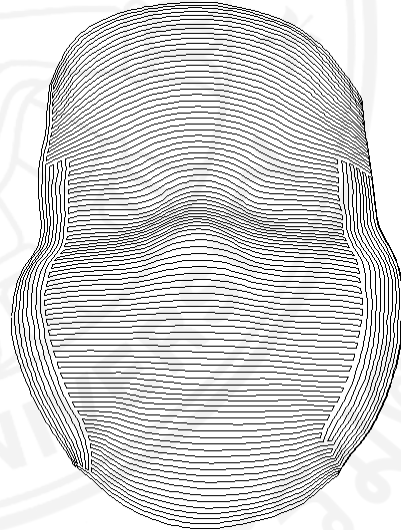
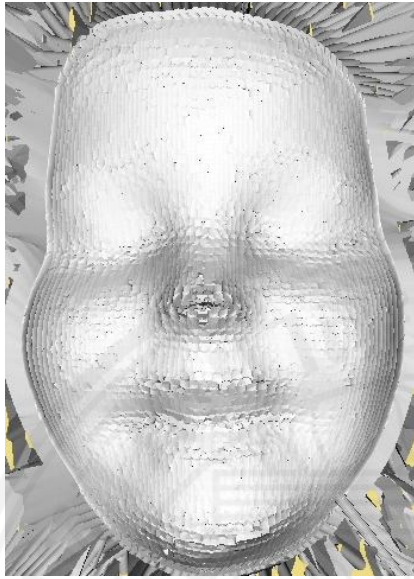(e)    $\alpha_L(u,v)$                           (f)    $\beta_L(u,v)$

(g)  VFAG$_R$          (h)  VFAG$_L$



(i)  BSFC$_R$          (j)  BSFC$_L$
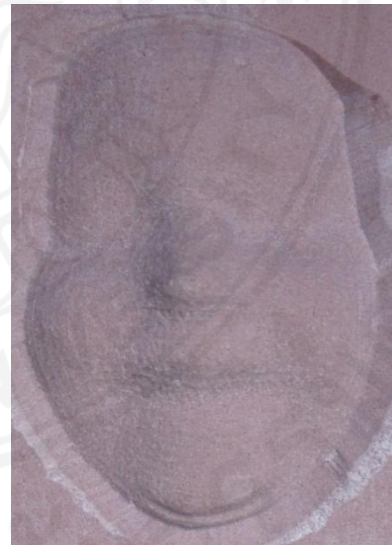
(k)    Virtual machining, ISO


(l)    Virtual machining, $ACT_R$


(m)    Real machining, ISO


(n)    Real machining, $ACT_R$

Figure 4.7: Machining the human face mask

Table 4.4: Human mask ace surface: ACT vs. the reference methods

| Toolpath Generation Methods | | | Scallop Height (mm) | | |
|---|---|---|---|---|---|
| | | | 0.25 | 0.10 | 0.05 |
| Performance | Toolpath Length (mm) | Master CAM | 17372.6 | 37669.5 | 71054.5 |
| | | HS | 2968.6 | 7072.1 | 13988.8 |
| | | FP | 3224.6 | 3241.2 | 4426.2 |
| | | ISO | 3115.6 | 3203.0 | 4072.0 |
| | | $ACT_R$ | 2944.9 | 2961.8 | 3530.1 |
| | | $ACT_L$ | 2681.3 | 2671.1 | 3364.0 |
| | Machining Time / HAAS VF2TR | HS | 0:24:42.0 | 0:57:53.8 | 1:53:36.8 |
| | | FP | 0:48:24.1 | 0:48:48.2 | 1:07:05.6 |
| | | ISO | 0:54:27.4 | 0:55:59.7 | 1:11:29.1 |
| | | $ACT_R$ | 0:51:57.2 | 0:51:43.1 | 1:02:10.3 |
| | | $ACT_L$ | 0:53:30.3 | 0:54:41.2 | 1:09:30.9 |
| | MAHO 600E | HS | 0:18:18.6 | 0:42:44.2 | 1:23:53.4 |
| | | FP | 0:24:57.8 | 0:25:17.8 | 0:34:30.2 |
| | | ISO | 0:17:52.6 | 0:18:24.9 | 0:23:27.5 |
| | | $ACT_R$ | 0:17:11.1 | 0:17:04.4 | 0:20:50.5 |
| | | $ACT_L$ | 0:17:39.2 | 0:18:07.3 | 0:22:57.1 |
| Advantage rel. to ISO | Toolpath Length (mm) | $ACT_R$ | 5.5% | 7.5% | 13.3% |
| | | $ACT_L$ | 13.9% | 16.6% | **17.4%** |
| | Machining Time / HAAS VF2TR | $ACT_R$ | 4.6% | 7.6% | **13.0%** |
| | | $ACT_L$ | 1.7% | 2.3% | 2.8% |
| | MAHO 600E | $ACT_R$ | 3.9% | 7.3% | 11.2% |
| | | $ACT_L$ | 1.2% | 1.6% | 2.2% |

Table 4.5: Human face surface: CC points, kinematic error, ACT vs. ISO

| Toolpath Generation techniques | HAAS VF-2TR | | | | | | | | | MAHO 600-E | | | | | | | | |
|---|---|---|---|---|---|---|---|---|---|---|---|---|---|---|---|---|---|---|
| | h=0.25 mm | | | h=0.10 mm | | | h=0.05 mm | | | h=0.25 mm | | | h=0.10 mm | | | h=0.05 mm | | |
| | $N_{CC}$ | $\bar{\varepsilon}$ | $\sigma_\varepsilon$ | $N_{CC}$ | $\bar{\varepsilon}$ | $\sigma_\varepsilon$ | $N_{CC}$ | $\bar{\varepsilon}$ | $\sigma_\varepsilon$ | $N_{CC}$ | $\bar{\varepsilon}$ | $\sigma_\varepsilon$ | $N_{CC}$ | $\bar{\varepsilon}$ | $\sigma_\varepsilon$ | $N_{CC}$ | $\bar{\varepsilon}$ | $\sigma_\varepsilon$ |
| ISO | 1509 | 0.081 | 0.616 | 3936 | 0.056 | 0.183 | 6917 | 0.050 | 0.031 | 1260 | 0.050 | 0.154 | 1221 | 0.028 | 0.064 | 3132 | 0.022 | 0.060 |
| $ACT_R$ | 1446 | 0.060 | 0.179 | 3896 | 0.035 | 0.104 | 6832 | 0.028 | 0.018 | 1171 | 0.034 | 0.076 | 1206 | 0.019 | 0.049 | 2704 | 0.009 | 0.030 |
| $ACT_L$ | 1023 | 0.061 | 0.077 | 2822 | 0.035 | 0.036 | 4911 | 0.025 | 0.029 | 275 | 0.026 | 0.050 | 962 | 0.018 | 0.027 | 1941 | 0.013 | 0.020 |

Table 4.6: Human face surface, roughness and waviness, ACT vs. ISO

| Roughness $R_a$ ($\mu$m) | | Standard Deviation | | Waviness $R_a$ | | Standard Deviation | |
|---|---|---|---|---|---|---|---|
| ISO | ACT$_R$ | ISO | ACT$_R$ | ISO | ACT$_R$ | ISO | ACT$_R$ |
| 8.3 | 8.1 | 7.7 | 7.7 | 43.6 | 40.8 | 23.8 | 28.6 |

### 4.3.3 Example 3 Dual vector field on a single Cartesian grid An STL model of the incisor tooth

We verify our methodology on the STL models of four types of human teeth: incisor, premolar, molar and canine. The STL model of the incisor and the corresponding flattened STL are presented in Figure 4.8. The incisor represents the case when the dual vector field on a single Cartesian grid leads to the significant improvement in terms of the length of the tool path and the machining time. The components of the dual vector fields $V_{D,R}(u,v) = (\alpha_R(u,v), \beta_R(u,v))$ and $V_{D,L}(u,v) = (\alpha_L(u,v), \beta_L(u,v))_L$ are shown on the surface and in the parametric domain in Figure 4.8 (c)-(h).VFAGs are presented in Figure 4.8 (i)-(l). Finally, machined surfaces are shown in Figure 4.8 (m) - (n).

Table 4.7 shows the benefits. The toolpath is 43% shorter and 46% faster against the standard ISO.  The advantage with regard to NX9 in terms of the length of the tool path is also very significant. For instance, when $h$=0.01, the ACT$_L$ generates the tool path of 570.9 whereas the best NX9 result is 1049.3. In the meantime the advantage in the machining time on HAAS is 17%. It should be noted that *neither MasterCam nor NX9 can produce the 5 axis tool path for the STL surface directly*. In order to compare their performance we flattened the STL surface, generated a boundary fitted curvilinear grid and approximated the surface on that grid. Therefore, *our MasterCam and NX9 toolpath generation is partly based on the proposed techniques*.  Finally, Table 4.8 shows that the efficiency of the ACT, measured by the number of the required CC points, increases whereas the average kinematic error practically does not change.
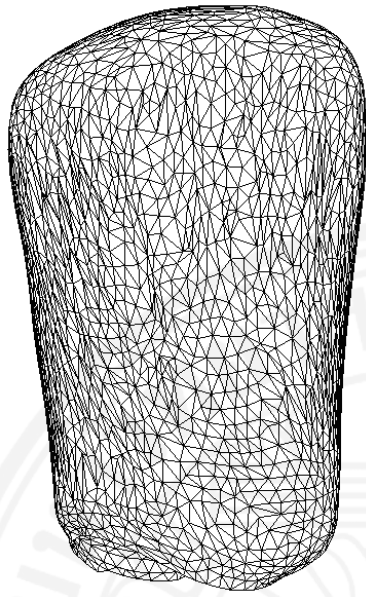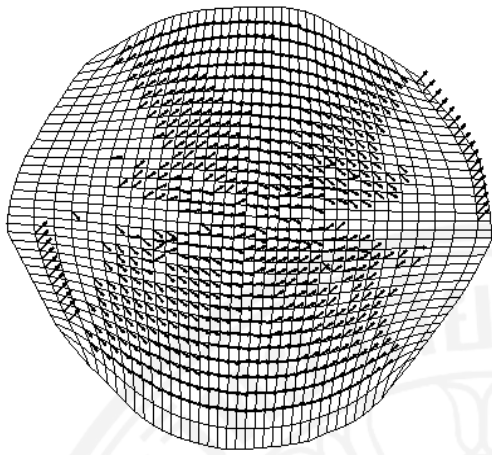
(a)     STL model of the incisor
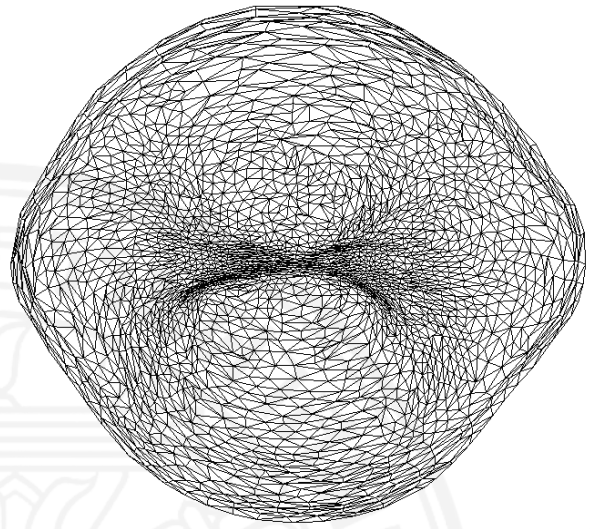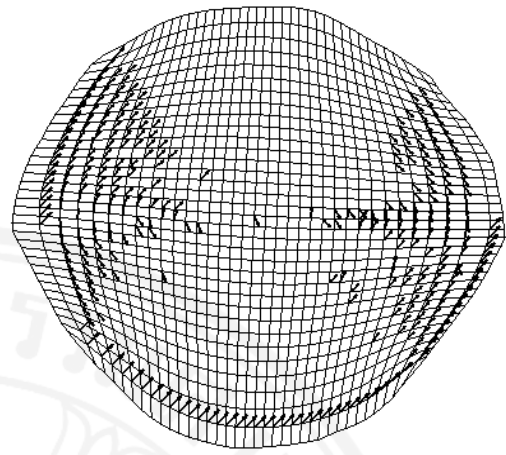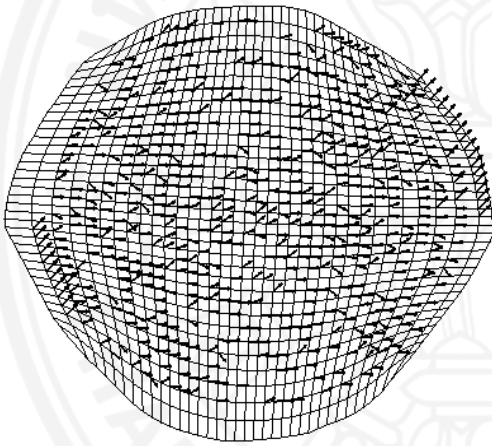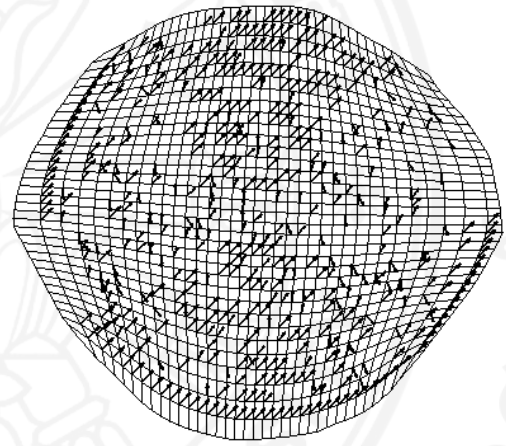
(b)     flattened incisor
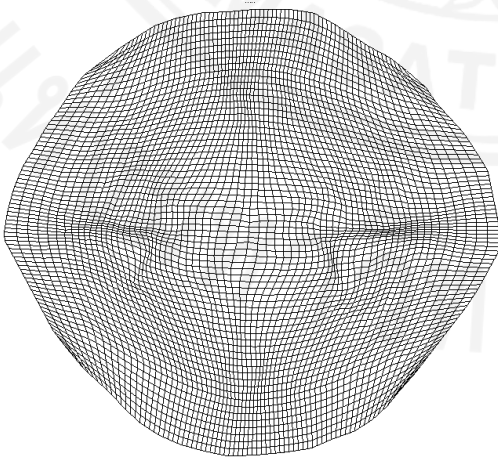
(c)    $V_R$

(d)    $V_L$

(e)     $\alpha_R(u,v)$

(f)     $\beta_R(u,v)$

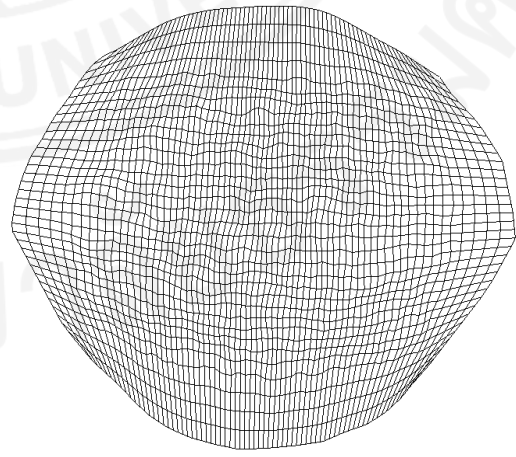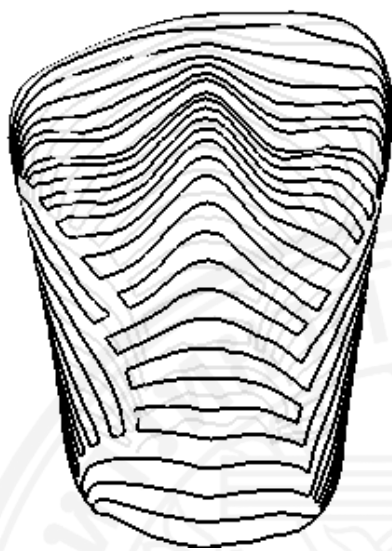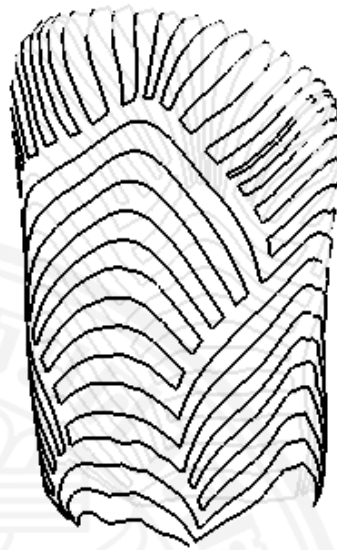(g)     $\alpha_L(u,v)$

(h)     $\beta_L(u,v)$

(i)     VFAG$_R$

(j)     VFAG$_L$

(k)    BSFC$_R$                          (l)    BSFC$_L$



(m)    Virtual milling, ACT$_R$          (n)    Virtual milling, ACT$_L$

Figure 4.8: Machining the incisor tooth

Table 4.7: Incisor tooth: ACT vs. the reference methods

| Toolpath Generation Methods | | | | Scallop Height (mm) | | |
|---|---|---|---|---|---|---|
| | | | | **0.065** | **0.025** | **0.0125** |
| **Performance** | **Toolpath Length (mm)** | | Master CAM | 6834.8 | 14373.3 | 27614.1 |
| | | | HS | 655.9 | 1477.7 | 2781.5 |
| | | | FP | 800.1 | 940.4 | 1049.3 |
| | | | ISO | 756.4 | 837.9 | 1005.5 |
| | | | ACT $_R$ | 469.1 | 515.6 | 582.9 |
| | | | ACT $_L$ | 456.0 | 498.5 | 570.9 |
| | **Machining Time** | **HAAS VF2TR** | HS | 0:18:22.0 | 0:40:40.2 | 1:19:15.1 |
| | | | FP | 0:21:13.4 | 0:28:27.7 | 0:30:50.6 |
| | | | ISO | 0:34:19.2 | 0:38:35.2 | 0:46:14.4 |
| | | | ACT $_R$ | 0:19:47.5 | 0:21:34.2 | 0:25:02.3 |
| | | | ACT $_L$ | 0:24:50.6 | 0:27:11.2 | 0:31:25.2 |
| | | **MAHO 600E** | HS | 0:07:34.5 | 0:16:48.4 | 0:32:04.6 |
| | | | FP | 0:07:30.5 | 0:08:53.7 | 0:09:55.8 |
| | | | ISO | 0:11:10.7 | 0:12:49.0 | 0:15:38.9 |
| | | | ACT $_R$ | 0:07:13.9 | 0:07:56.6 | 0:09:11.0 |
| | | | ACT $_L$ | 0:07:13.1 | 0:08:09.3 | 0:09:33.1 |
| **Advantage ref. to ISO** | **Toolpath Length (mm)** | | ACT $_R$ | 38.00% | 38.5% | 42.0% |
| | | | ACT $_L$ | 39.70% | 40.5% | 43.2% |
| | **Machining Time** | **HAAS VF2TR** | ACT $_R$ | 42.30% | 44.1% | 45.9% |
| | | | ACT $_L$ | 27.60% | 29.5% | 32.0% |
| | | **MAHO 600E** | ACT $_R$ | 35.30% | 38.0% | 41.3% |
| | | | ACT $_L$ | 35.40% | 36.4% | 39.0% |

Table 4.8: Incisor tooth: CC points, kinematic error, ACT vs. ISO

| | **HAAS VF-2TR** | | | | | | | | | **MAHO 600-E** | | | | | | | | |
|---|---|---|---|---|---|---|---|---|---|---|---|---|---|---|---|---|---|---|
| | **h=0.065 mm** | | | **h=0.025 mm** | | | **h=0.0125 mm** | | | **h=0.065 mm** | | | **h=0.025 mm** | | | **h=0.0125 mm** | | |
| | $N_{CC}$ | $\bar{\varepsilon}$ | $\sigma_\varepsilon$ | $N_{CC}$ | $\bar{\varepsilon}$ | $\sigma_\varepsilon$ | $N_{CC}$ | $\bar{\varepsilon}$ | $\sigma_\varepsilon$ | $N_{CC}$ | $\bar{\varepsilon}$ | $\sigma_\varepsilon$ | $N_{CC}$ | $\bar{\varepsilon}$ | $\sigma_\varepsilon$ | $N_{CC}$ | $\bar{\varepsilon}$ | $\sigma_\varepsilon$ |
| **ISO** | 576 | 0.048 | 0.173 | 1709 | 0.030 | 0.136 | 4880 | 0.021 | 0.122 | 36 | 0.013 | 0.029 | 246 | 0.011 | 0.026 | 1282 | 0.008 | 0.024 |
| **ACT$_R$** | 222 | 0.044 | 0.069 | 923 | 0.026 | 0.056 | 2545 | 0.016 | 0.072 | 7 | 0.010 | 0.023 | 99 | 0.009 | 0.017 | 611 | 0.006 | 0.013 |
| **ACT$_L$** | 574 | 0.051 | 0.178 | 1443 | 0.031 | 0.134 | 3425 | 0.027 | 0.109 | 60 | 0.014 | 0.032 | 350 | 0.009 | 0.024 | 1137 | 0.007 | 0.024 |

## 4.3.4 Example 4 O–grids applied to the STL models of canine, premolar and molar teeth

The following three cases of the STL surfaces corresponding to premolar, molar and canine teeth are characterized by the unstructured (chaotic) vector field. Consequently, VFAGs do not produce any improvement even though the grids can be aligned with some small clusters of the vectors. However, we show that the tools provided by ACT still can be used to improve the quality of the toolpath generation. We show that boundary fitted curvilinear tool path combined with a manual selection of the type of the grid and BSFC lead to a substantial improvement.

The STL-premolar and its flattened version are presented in Figure 4.9 (a) - (d). The boundary fitted initial grids in Figure 4.9 (e) and (f) are the H-grid and the O-grid respectively. In order to evaluate the suitability of the grid we compute the alignment functional (3.4) as follows:

$$F_{V,H,canine} = 16.0, \qquad\qquad F_{V,O,canine} = 14.0, F_{V,H,premolar} = 16.7,$$

$$F_{V,O,premolar} = 14.0, F_{V,H,molar} = 19.3, \ F_{V,O,molar} = 17.6.$$

Clearly, the O-grid is more suitable for the three dental models. The corresponding toolpaths and virtually machined surfaces are shown in Figure 4.9 (g) – Figure 4.9 (l). The results for the molar and canine teeth are displayed in Figure 4.10 and Figure 4.11. Finally, Table 4.9 presents the benefits of ACT compared to ISO and to NX9 and MasterCAM. The proposed framework provides the advantage in both the toolpath length and machining time with regard to the benchmark methods. For instance, the premolar tooth can be machined by ACT with the advantage of 26% in length and 43% in time relative to ISO.

Table 4.10 provides the number of CC points versus the scallop height and the kinematics error.

93
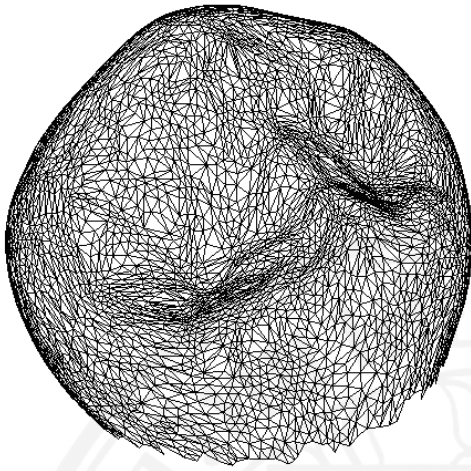
(a)　　STL model of the premolar
tooth
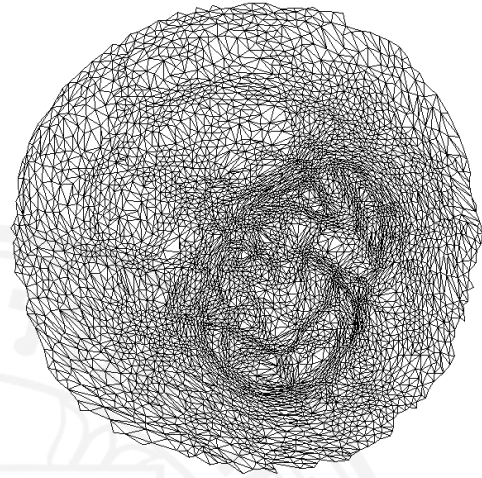
(b)　　flattened premolar tooth

(c)　　$V_R$

(d)　　$V_L$

(e)　　H-grid

(f)　　O-grid

(g)     $ISO_H$

(h)     $ISO_O$

(i)     $BSFC_H$

(j)     $BSFC_O$

(k)     Virtual milling $ISO_H$
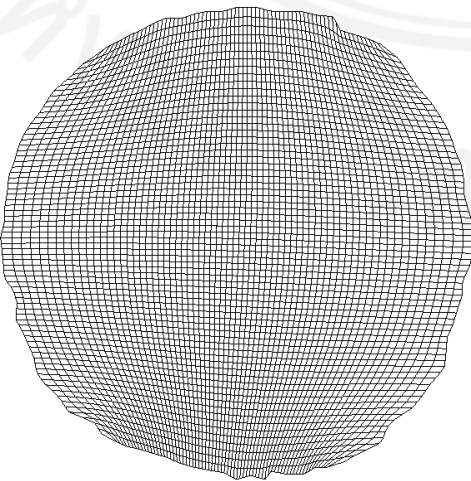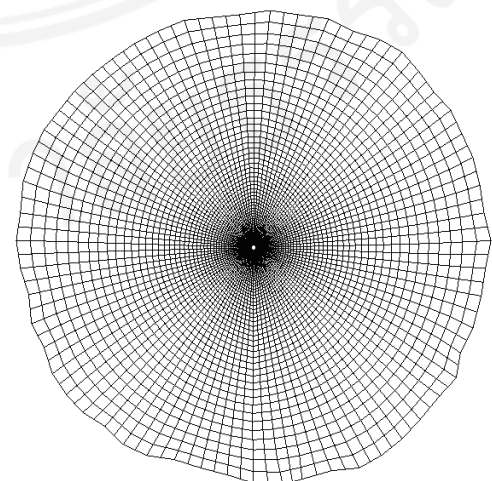
(l)     Virtual milling $BSFC_O$

Figure 4.9: Machining the premolar tooth

(a)    STL model of the molar tooth       (b)    flattened molar tooth
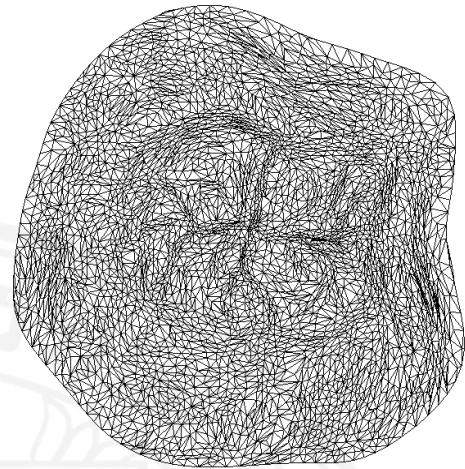
(c)    H-grid                  (d)    O-grid

(e)    $ISO_H$                  (f)    $ISO_O$

(g)     BSFC$_H$

(h)     BSFC$_O$



(i)     Virtual milling, ISO$_H$
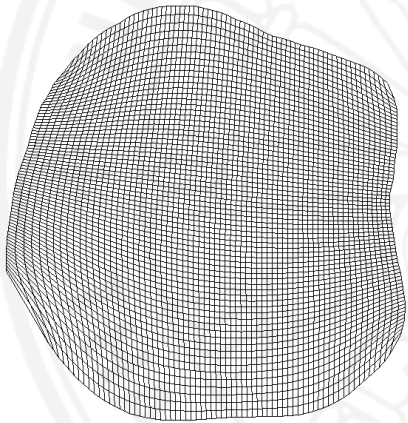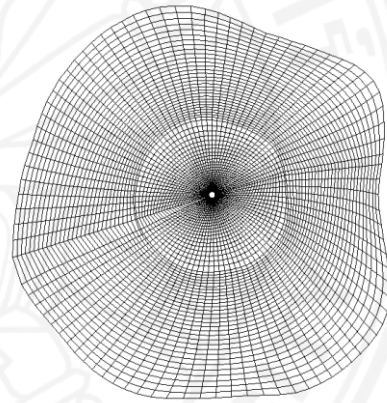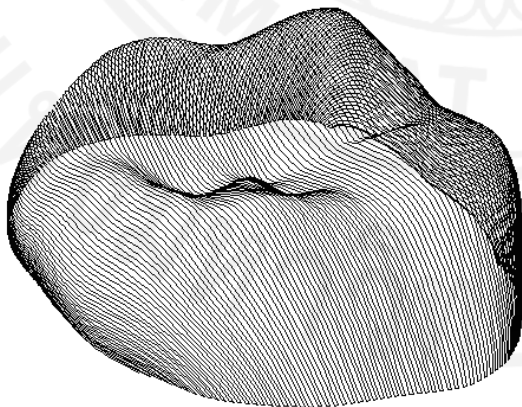
(j)     Virtual milling, BSFC$_O$
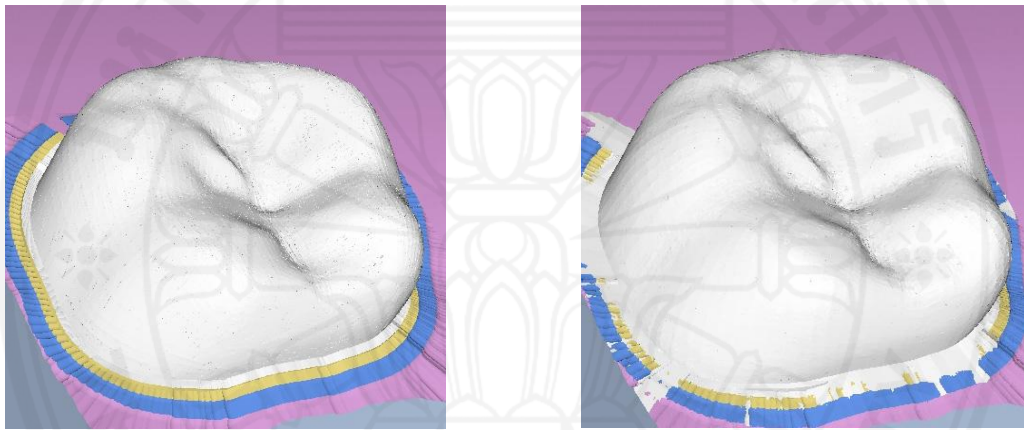
Figure 4.10: Machining the molar tooth



(a)     STL model of a canine tooth

(b)     Flattened canine

(c)     H-grid                   (d)     O-grid
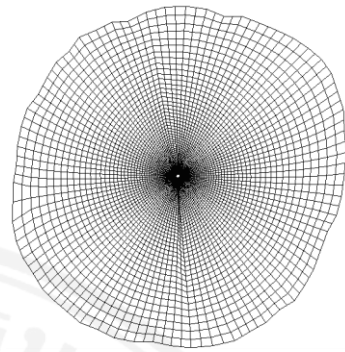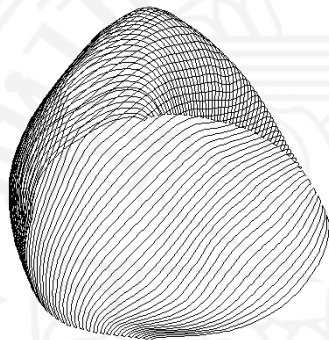
(e)     $ISO_H$                   (f)     $ISO_O$
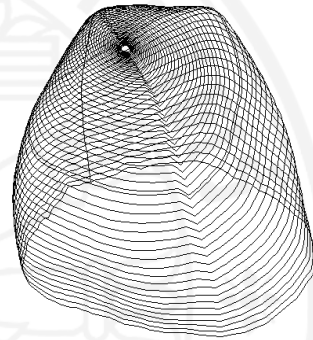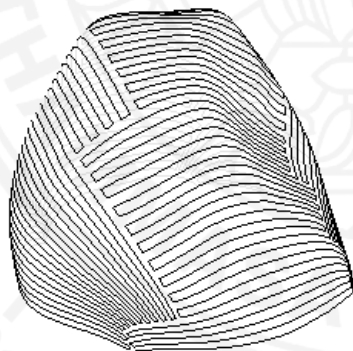
(g)   $BSFC_H$                  (h)  $BSFC_O$
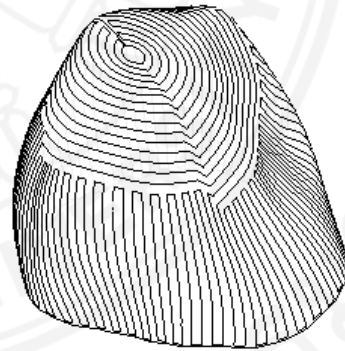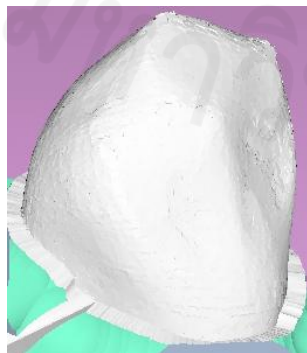
(i)    Virtual Milling $ISO_H$        (j)    Virtual Milling $BSFC_O$

Figure 4.11: Machining the canine tooth

98

Table 4.9: ACT vs. the reference methods, molar, premolar and canine tooth

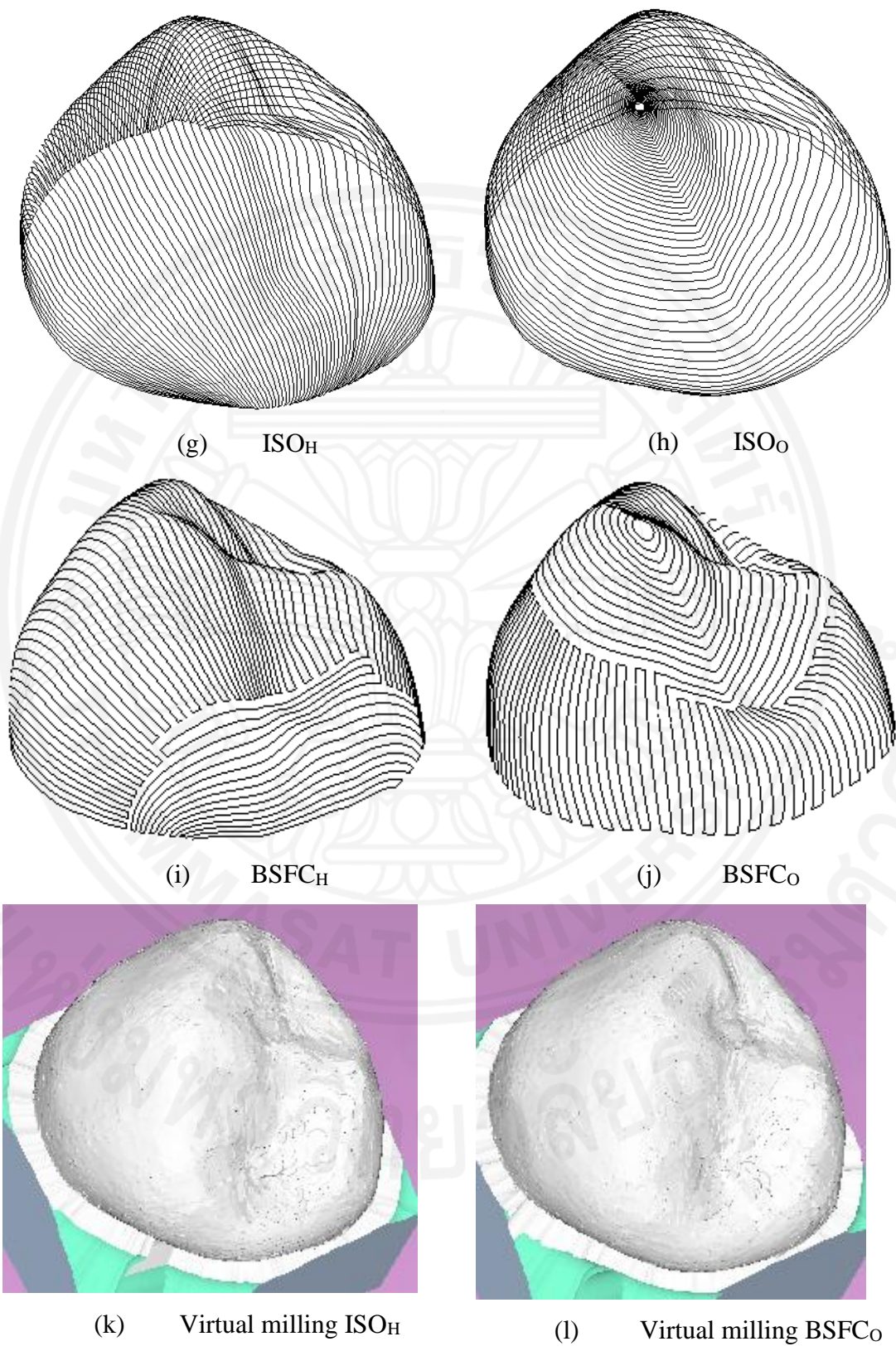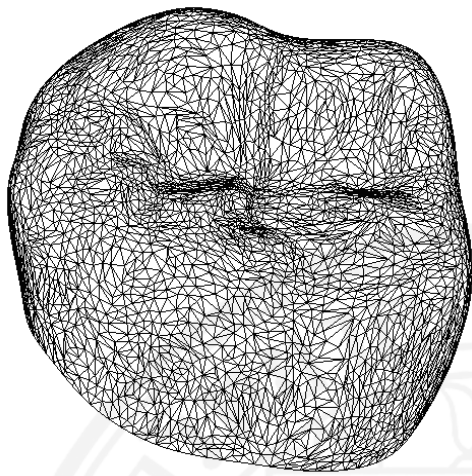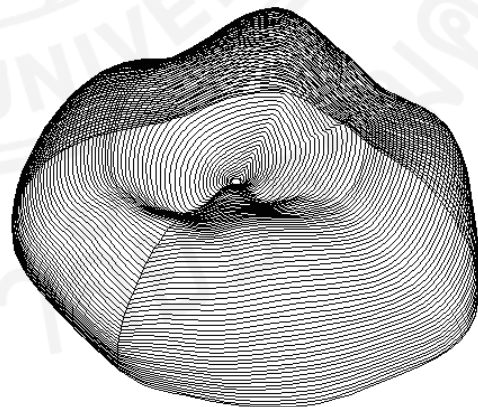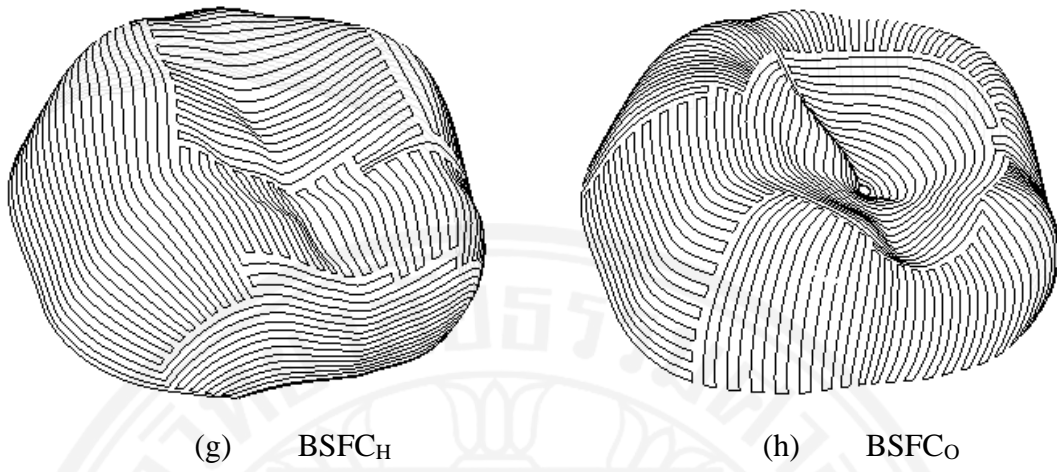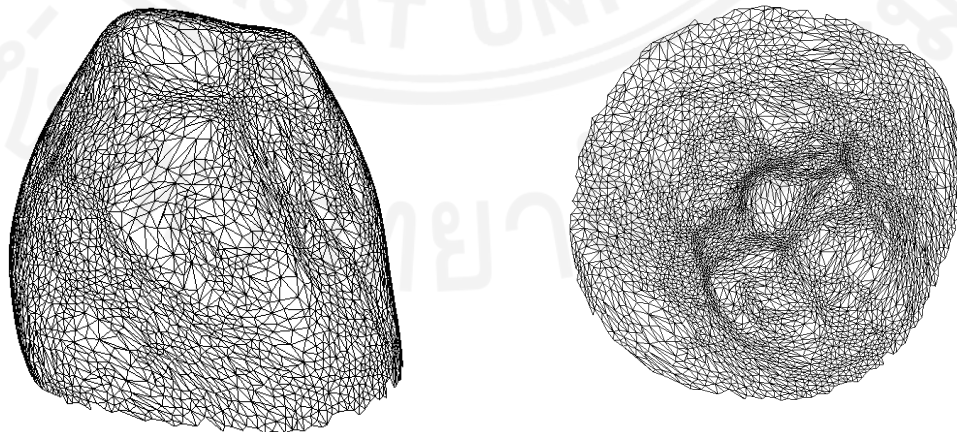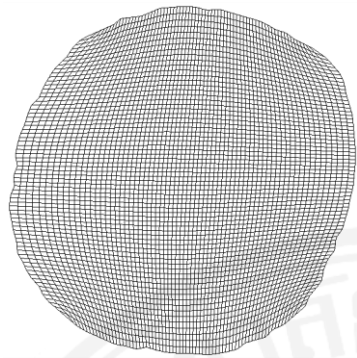| | | Toolpath Generation Techniques | Canine | | | Premolar | | | Molar | | |
|---|---|---|---|---|---|---|---|---|---|---|---|
| | | | Scallop Height (mm) | | | Scallop Height (mm) | | | Scallop Height (mm) | | |
| | | | 0.065 | 0.025 | 0.0125 | 0.065 | 0.025 | 0.0125 | 0.065 | 0.025 | 0.0125 |
| Performance | Toolpath Length (mm) | Master CAM | 4261.3 | 9615.0 | 18802.0 | 5275.9 | 12560.3 | 25009.4 | 6483.1 | 15102.6 | 30074.0 |
| | | HS | 1013.0 | 2330.4 | 4599.0 | 1023.5 | 2360.9 | 4614.8 | 1284.6 | 2992.0 | 5912.0 |
| | | FP | 1120.5 | 1181.6 | 1230.2 | 1129.6 | 1156.9 | 1217.7 | 1099.9 | 1141.9 | 1184.5 |
| | | ISO | 766.7 | 778.4 | 801.5 | 761.7 | 773.2 | 783.5 | 847.6 | 854.4 | 855.4 |
| | | O-Grid | 664.6 | 664.5 | 664.4 | 616.9 | 622.6 | 620.5 | 826.9 | 827.7 | 828.2 |
| | | $BSFC_H$ | 610.7 | 620.3 | 634.3 | 616.1 | 617.5 | 623.5 | 782.5 | 784.8 | 785.4 |
| | | $BSFC_O$ | 617.8 | 627.4 | 641.6 | 573.2 | 574.6 | 580.1 | 742.9 | 745.1 | 745.7 |
| | HAAS VF2TR | HS | 0:20:36.5 | 0:47:34.7 | 1:33:34.8 | 0:24:28.4 | 0:56:43.5 | 1:50:48.3 | 0:37:12.3 | 1:27:20.7 | 2:51:51.9 |
| | | FP | 0:24:54.2 | 0:26:15.4 | 0:27:18.8 | 0:34:15.9 | 0:35:04.8 | 0:36:43.3 | 0:37:03.1 | 0:38:46.2 | 0:39:52.8 |
| | | ISO | 0:24:21.8 | 0:24:48.3 | 0:25:19.3 | 0:36:41.9 | 0:38:14.5 | 0:42:14.5 | 0:41:27.5 | 0:41:55.5 | 0:42:34.1 |
| | | O-Grid | 0:22:15.8 | 0:22:33.5 | 0:22:52.9 | 0:28:09.1 | 0:28:24.6 | 0:30:41.5 | 0:35:19.5 | 0:35:35.1 | 0:35:40.0 |
| | | $BSFC_H$ | 0:20:55.9 | 0:21:05.1 | 0:21:07.9 | 0:28:44.5 | 0:28:50.6 | 0:30:30.3 | 0:32:47.4 | 0:32:55.0 | 0:32:58.7 |
| | | $BSFC_O$ | 0:20:01.9 | 0:20:10.7 | 0:20:13.3 | 0:27:57.2 | 0:28:03.1 | 0:29:40.2 | 0:33:17.6 | 0:33:25.3 | 0:33:29.1 |
| | MAHO 600E | HS | 0:13:48.8 | 0:31:42.8 | 1:02:24.8 | 0:17:35.1 | 0:40:19.1 | 1:18:37.1 | 0:28:52.8 | 1:07:35.2 | 2:13:07.7 |
| | | FP | 0:10:45.1 | 0:11:20.2 | 0:11:48.2 | 0:13:48.4 | 0:14:06.2 | 0:14:42.3 | 0:19:19.1 | 0:20:13.7 | 0:20:41.2 |
| | | ISO | 0:12:20.3 | 0:12:55.3 | 0:13:18.7 | 0:19:20.1 | 0:19:30.1 | 0:19:46.5 | 0:21:19.7 | 0:21:34.5 | 0:22:25.1 |
| | | O-Grid | 0:10:13.7 | 0:10:38.5 | 0:10:55.9 | 0:12:06.4 | 0:12:11.7 | 0:12:15.6 | 0:17:48.3 | 0:17:58.1 | 0:18:02.0 |
| | | $BSFC_H$ | 0:10:15.3 | 0:10:38.3 | 0:10:39.7 | 0:13:40.9 | 0:13:42.7 | 0:13:48.7 | 0:18:32.3 | 0:18:40.6 | 0:18:47.1 |
| | | $BSFC_O$ | 0:09:18.3 | 0:09:39.1 | 0:09:40.4 | 0:11:00.3 | 0:11:01.7 | 0:11:06.6 | 0:18:45.0 | 0:18:53.3 | 0:18:59.9 |
| Advantage rel. to ISO | Toolpath Length (mm) | O-Grid | 13.3% | 14.6% | 17.1% | 19.0% | 19.5% | 20.8% | 2.4% | 3.1% | 3.2% |
| | | $BSFC_H$ | 20.3% | 20.3% | 20.9% | 19.1% | 20.1% | 20.4% | 7.7% | 8.1% | 8.2% |
| | | $BSFC_O$ | 19.4% | 19.4% | 19.9% | 24.7% | 25.7% | 26.0% | 12.3% | 12.8% | 12.8% |
| | HAAS VF2TR | O-Grid | 8.6% | 9.1% | 9.6% | 23.3% | 25.7% | 27.3% | 14.8% | 15.1% | 16.2% |
| | | $BSFC_H$ | 14.1% | 15.0% | 16.6% | 21.7% | 24.6% | 27.8% | 20.9% | 21.5% | 22.5% |
| | | $BSFC_O$ | 17.8% | 18.7% | 20.1% | 23.8% | 26.6% | 29.8% | 19.7% | 20.3% | 21.3% |
| | MAHO 600E | O-Grid | 17.1% | 17.6% | 17.9% | 37.4% | 37.5% | 38.0% | 16.5% | 16.7% | 19.6% |
| | | $BSFC_H$ | 16.9% | 17.7% | 19.9% | 29.2% | 29.7% | 30.2% | 13.1% | 13.4% | 16.2% |
| | | $BSFC_O$ | 24.6% | 25.3% | 27.3% | 43.1% | 43.4% | 43.8% | 12.1% | 12.5% | 15.3% |

Table 4.10: Molar, premolar and canine: CC points, kinematic error, ACT vs. ISO
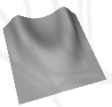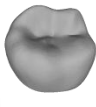
| Scallop height | Method | Type | HAAS VF2TR | | | MAHO 600E | | |
|---|---|---|---|---|---|---|---|---|
| | | | Molar | Premolar | Canine | Molar | Premolar | Canine |
| 0.065 | ISO | $N_{CC}$ | 1645 | 788 | 342 | 379 | 203 | 58 |
| | | $\overline{\varepsilon}$ | 0.078 | 0.059 | 0.035 | 0.039 | 0.019 | 0.012 |
| | | $\sigma_{\varepsilon}$ | 0.170 | 0.173 | 0.065 | 0.048 | 0.074 | 0.033 |
| | O-Grid | $N_{CC}$ | 1637 | 708 | 302 | 577 | 163 | 59 |
| | | $\overline{\varepsilon}$ | 0.073 | 0.064 | 0.041 | 0.038 | 0.024 | 0.012 |
| | | $\sigma_{\varepsilon}$ | 0.174 | 0.280 | 0.062 | 0.058 | 0.051 | 0.031 |
| | BSFC$_H$ | $N_{CC}$ | 1575 | 748 | 306 | 478 | 174 | 59 |
| | | $\overline{\varepsilon}$ | 0.069 | 0.060 | 0.035 | 0.038 | 0.021 | 0.012 |
| | | $\sigma_{\varepsilon}$ | 0.167 | 0.220 | 0.058 | 0.049 | 0.062 | 0.030 |
| | BSFC$_O$ | $N_{CC}$ | 1619 | 741 | 304 | 468 | 175 | 56 |
| | | $\overline{\varepsilon}$ | 0.068 | 0.057 | 0.033 | 0.036 | 0.021 | 0.011 |
| | | $\sigma_{\varepsilon}$ | 0.167 | 0.209 | 0.056 | 0.051 | 0.060 | 0.030 |
| 0.025 | ISO | $N_{CC}$ | 3080 | 1654 | 984 | 776 | 445 | 171 |
| | | $\overline{\varepsilon}$ | 0.048 | 0.037 | 0.026 | 0.026 | 0.017 | 0.011 |
| | | $\sigma_{\varepsilon}$ | 0.143 | 0.163 | 0.059 | 0.046 | 0.065 | 0.018 |
| | O-Grid | $N_{CC}$ | 3099 | 1655 | 920 | 1171 | 435 | 164 |
| | | $\overline{\varepsilon}$ | 0.042 | 0.037 | 0.028 | 0.026 | 0.017 | 0.010 |
| | | $\sigma_{\varepsilon}$ | 0.142 | 0.253 | 0.051 | 0.032 | 0.035 | 0.018 |
| | BSFC$_H$ | $N_{CC}$ | 2966 | 1638 | 933 | 974 | 427 | 159 |
| | | $\overline{\varepsilon}$ | 0.044 | 0.036 | 0.026 | 0.024 | 0.016 | 0.010 |
| | | $\sigma_{\varepsilon}$ | 0.128 | 0.202 | 0.053 | 0.035 | 0.048 | 0.016 |
| | BSFC$_O$ | $N_{CC}$ | 2957 | 1632 | 936 | 974 | 418 | 165 |
| | | $\overline{\varepsilon}$ | 0.040 | 0.036 | 0.026 | 0.024 | 0.017 | 0.009 |
| | | $\sigma_{\varepsilon}$ | 0.138 | 0.196 | 0.052 | 0.036 | 0.048 | 0.016 |
| 0.0125 | ISO | $N_{CC}$ | 6359 | 3692 | 2115 | 1878 | 1206 | 520 |
| | | $\overline{\varepsilon}$ | 0.021 | 0.025 | 0.018 | 0.014 | 0.012 | 0.009 |
| | | $\sigma_{\varepsilon}$ | 0.130 | 0.183 | 0.048 | 0.042 | 0.057 | 0.016 |
| | O-Grid | $N_{CC}$ | 6309 | 3698 | 2086 | 2897 | 1134 | 490 |
| | | $\overline{\varepsilon}$ | 0.021 | 0.024 | 0.018 | 0.015 | 0.012 | 0.008 |
| | | $\sigma_{\varepsilon}$ | 0.101 | 0.236 | 0.046 | 0.023 | 0.025 | 0.016 |
| | BSFC$_H$ | $N_{CC}$ | 6207 | 3621 | 2079 | 2292 | 1170 | 480 |
| | | $\overline{\varepsilon}$ | 0.019 | 0.025 | 0.017 | 0.014 | 0.012 | 0.008 |
| | | $\sigma_{\varepsilon}$ | 0.104 | 0.207 | 0.043 | 0.030 | 0.040 | 0.016 |
| | BSFC$_O$ | $N_{CC}$ | 6292 | 3597 | 2093 | 2261 | 1158 | 492 |
| | | $\overline{\varepsilon}$ | 0.019 | 0.024 | 0.017 | 0.013 | 0.011 | 0.008 |
| | | $\sigma_{\varepsilon}$ | 0.105 | 0.194 | 0.044 | 0.029 | 0.038 | 0.015 |

## 4.4 Discussion

The ACT technology is flexible and presents many options. However, there is no universal recipe applicable to every surface. Nevertheless, a correct selection of the tools available within the proposed framework always leads to an improvement of the toolpath in terms of its length and the machining time.

Table 4.11 summarizes the experiments presented in the paper and shows combinations which provided the maximum benefit.

Table 4.11: Performance of ACT

| Toolpath Generation Techniques Combination | Dental-like | Face | Incisor | Canine | Premolar | Molar |
|---|---|---|---|---|---|---|
| Surface Flattening | ☒ | ☒ | ☒ | ☒ | ☒ | ☒ |
| Surface Decomposition | ☒ | | | | | |
| H-grid | ☒ | ☒ | ☒ | | | |
| O-grid | ☒ | | | ☒ | ☒ | ☒ |
| Vector Field Aligned Grid | ☒ | ☒ | ☒ | | | |
| Biased Space Filling Curve | ☒ | ☒ | ☒ | ☒ | ☒ | ☒ |
| **Max advantage relative to ISO** | | | | | | |
| Toolpath Length | 20.7% | 17.4% | 43.2% | 20.9% | 26.0% | 12.8% |
| Machining Time HAAS VF-2TR | 72.2% | 13.0% | 45.9% | 20.1% | 29.8% | 22.5% |
| Machining Time MAHO-600E | 68.3% | 11.2% | 41.3% | 27.3% | 43.8% | 19.6% |

# Chapter 5

# Conclusions and Future Work

## 5.1    Conclusions

A new method for generation of vector field aligned tool paths for five-axis machining has been presented and analyzed. The new idea is the numerical generation of a curvilinear grid adapted to the vector field of optimal directions and the biased space filling curve. The method provides up to a 70% decrease of the machining time with regard to the iso-parametric tool path, works better than preceding methods based on the non-biased space filling curves, and outperforms advanced tool path generation developed by MasterCam and NX9 ( former Unigraphics) .

The method has been generalized into a new framework for generation of adaptive vector field aligned toolpaths and has been applied to STL files representing complex shaped surfaces. The STL files are parameterized by a modification of the radial plane method combined with the numerical grid generation.

The tests against the benchmark methods show that the kinematic error and the roughness of the workpiece remain practically unchanged, while the machining time, the tool path length and the waviness have been considerably reduced. The method provides up to 70% decrease of the machining time with regard to the iso parametric tool path and up to 64% with regard to Follow Periphery of NX9 (the best reference method). The advantage with regard to Helical/Spiral of NX9 and MasterCAM is overwhelming: the machining time is 10-20 times shorter.

Although there is no  a universal recipe applicable to every surface a correct selection of the tools available within the proposed framework always leads to an improvement of the tool path in terms of its length and the machining time.

## 5.2    Future work

- Hybrid-patterns for complex surfaces. Different pattern such as spiral, zigzag, curvilinear zigzag and space filling curves can be combined to enhance the machining efficiency.

- Clustering. The clustering technique should be used to exploit similarity of the surface characteristics and to decompose the surface into appropriate patches.

- Reliable parameterization. Flattening algorithm for a complex surface should be improved. The radial plane algorithm can fail when flattening a complex shaped surface characterized by twists.

- Extended cost functions. High-speed micro-milling for the dental industry requires superior accuracy. Therefore, the mechanical engineering cost functions such as the force and the thermal load must be considered by the tool path generation algorithms.

# Chapter 6
# Open Problems

This dissertation analyzes the impact of the tool positions and orientations on the machining time and the accuracy of the machined part surface with the understanding that there are many other parameters and processes that affect the efficiency and quality of the five axis machining. Among them are the machining feed rate [119-122], kinematics and dynamics of the CNC mechanisms [123,124], the cutting forces and tool deflections [125], thermal deformations [126-129] as well as the systematic errors [118,130]. Some other, less prominent but still important, sources of errors are machine operating conditions such as the material removal rate (feed rate), the depth of the cut, wet or dry cutting, clamping conditions, the tool wear and other tool imperfections [5].

As a matter of fact, not every part is the 5 axis candidate. The validation of the suitability of 5 axis mode is in fact an open problem. For instance, the rotational joints change the stability conditions of the cutting operations (the natural frequencies of the system) which may lead to an unexpected chatter (self-excited vibrations) and unwanted waviness of the part surface. Even under stable, chatter free conditions, the tool is subjected to periodic forced vibrations leading to overcuts or undercuts. These effects may amount to as much as 75% of all the errors [139].

Furthermore, the tool deflection errors are one of the most prominent [140]. Milling a complex shape may be affected by deflections of the end mills caused by variation of the cutting forces, especially when a corner cutting (complex pocket milling) is involved [141,142]. The end milling force and deflection depend on the tool path, tool geometry, cutting conditions and the material properties [143,144]. Although it is difficult to entirely eliminate these errors, a considerable reduction can be achieved by various compensating strategies [145]. As far as the accuracy-related geometric errors are concerned, they can be attributed to three main types. The first type is related to the kinematics of the 5 machine [148] and includes the systematic errors [130] and errors attributed to the initial set-up [118]. The machines with three linear axes have a total of 21 linear independent geometric error components [149], whereas the five-

axis milling machine has 42 components (twice of the three-axis machine!) [150]. The second source is the imperfection of the movements the machine components and its fixtures [151,152].

Moreover, even within the framework of this dissertation the efficiency improvement can be measured using a variety of cost functions leading to different results on different machines. Such cost functions can be based on the machining strip, the feed direction [87], the force-minimization [88], aligning with optimal directions [40,41] etc. Most of these criteria are machine dependent and yet the tool path generation software such as MasterCam or NX (Unigraphics) generates the tool path irrespectively of the machine kinematics. Clearly, up to now there does not exist a model which unifies or combines the above mentioned sources of errors or at least classifies their importance relative to a particular part surface and a particular machine. As far as the kinematic of the 5 axis machines is considered, the majority of the research papers analyze the machines with orthogonal linear axes leaving the non-orthogonal case out of the scope.

Finally, we state the following interesting open problems related to the main subjects of this dissertation:

**Vector Field Alignment**

- Is it possible to entirely align the tool path with the given vector field using some kind of clustering or other decomposition of the part surface (see for instance [40,41])?
- How to apply the proposed vector field alignment methods and the cost functions if we allow to change the tool during the machine operation? This includes not only the size of the tool but the tool shape as well (for instance [186])?
- How to combine the vector field alignment with a possible decomposition of the surface performed to flatten the STL file?
- Is it possible to combine the proposed method with other file formats such STEP or IGES (NURBS)?

- How to apply the alignment techniques to spiral tool paths using the adaptive curvilinear polar grids?
- How to define automatically the best type of curvilinear grid (H-type, O-type, C-type, polar grid) given the particular vector field?

**Biased Space Filling Curves**

- How to apply the biased space filling curves to the domains with arbitrary shaped islands (complex pocket machining)?

- Is it possible to generate a BSFC if we allow the diagonal step (8 connected pattern) and how should then the grid generation method work?

**STL flattening**

- Is it possible to apply the proposed radial flattening techniques to an arbitrary surface using decomposition?

- How to combine the decomposition of the vector field and decomposition of the STL surface?

**Controller Execution**

Is the algorithm invariant with regard to the controller execution? Clearly, it is not the case for high speed machining in the case when the time of moving the tool from one CC point to another is shorted the update rate of servo controller.

# References

1. Bohez, ELJ. (2002). Five-axis milling machine tool kinematic chain design and analysis. *International Journal of Machine Tools and Manufacture.* 42(4), 505-520.

2. Lo, CC. (1999). Efficient cutter-path planning for five-axis surface machining with a flat-end cutter. *Computer-Aided Design.* 31(9), 557-566.

3. Dragomatz, D;Mann, S. (1997). A classified bibliography of literature on NC milling path generation. *Computer-Aided Design.* 29(3), 239-247.

4. Sarma, R. (2000). An assessment of geometric methods in trajectory synthesis for shape-creating manufacturing operations. *Journal of Manufacturing Systems.* 19(1), 59-72.

5. Makhanov, S. (2010). Adaptable geometric patterns for five-axis machining: a survey. *The International Journal of Advanced Manufacturing Technology.* 47(9-12), 1167-1208.

6. Lasemi, A;Xue, D;Gu, P. (2010). Recent development in CNC machining of freeform surfaces: A state-of-the-art review. *Computer-Aided Design.* 42(7), 641-654.

7. Cho, JH;Kim, JW;Kim, K. (2000). CNC tool path planning for multi-patch sculptured surfaces. *International Journal of Production Research.* 38(7), 1677-1687.

8. Makhanov, SS;Anotaipaiboon, W. (2007). *Advanced Numerical Methods to Optimize Cutting Operations of Five Axis Milling Machines*. Springer.

9. Choi, YK;Banerjee, A. (2007). Tool path generation and tolerance analysis for free-form surfaces. *International Journal of Machine Tools and Manufacture.* 47(3-4), 689-696.

10. Li, F;Wang, XC;Ghosh, SK;Kong, DZ;Lai, TQ;Wu, XT. (1995). Tool-path generation for machining sculptured surface. *Journal of Materials Processing Technology.* 48(1–4), 811-816.

11. Pi, J;Red, E;Jensen, G. (1998). Grind-free tool path generation for five-axis surface machining. *Computer Integrated Manufacturing Systems.* 11(4), 337-350.

12. Makhanov, SS. (1999). An application of variational grid generation techniques to the tool-path optimization of industrial milling robots *Computational Mathematics and Mathematical Physics.* 39:9(

13. Makhanov, SS;Batanov, D;Bohez, E;Sonthipaumpoon, K;Anotaipaiboon, W;Tabucanon, M. (2002). On the tool-path optimization of a milling robot. *Computers & Industrial Engineering.* 43(3), 455-472.

14. Feng, HY;Huiwen, L. (2002). Constant scallop-height tool path generation for three-axis sculptured surface machining. *CAD Computer Aided Design.* 34(9), 647-654.

15. Li, SX;Jerard, RB. (1994). 5-axis machining of sculptured surfaces with a flat-end cutter. *Computer-Aided Design.* 26(3), 165-178.

16. Chen, ZC;Vickers, GW;Dong, Z. (2003). Integrated steepest-directed and iso-cusped toolpath generation for three-axis CNC machining of sculptured parts. *Journal of Manufacturing Systems.* 22(3), 190-201.

17. Held, M. (1991). On the computational geometry of pocket machining. *On the Computational Geometry of Pocket Machining.*

18. Held, M. (1991). A geometry-based investigation of the tool path generation for zigzag pocket machining. *The Visual Computer.* 7(5-6), 296-308.

19. Loney, GC;Ozsoy, TM. (1987). NC machining of free form surfaces. *Computer-Aided Design.* 19(2), 85-90.

20. Chen, YD;Ni, J;Wu, SM. (1993). Real-time CNC tool path generation for machining IGES surfaces. *Journal of engineering for industry.* 115(4), 480-486.

21. Rao, N;Ismail, F;Bedi, S. (1997). Tool path planning for five-axis machining using the principal axis method. *International Journal of Machine Tools and Manufacture.* 37(7), 1025-1040.

22. Feng, HY;Teng, Z. (2005). Iso-planar piecewise linear NC tool path generation from discrete measured data points. *CAD Computer Aided Design.* 37(1), 55-64.

23. Park, SC;Choi, BK. (2000). Tool-path planning for direction-parallel area milling. *Computer-Aided Design.* 32(1), 17-25.

24. Park, SC;Chung, YC. (2002). Offset tool-path linking for pocket machining. *Computer-Aided Design.* 34(4), 299-308.

25. Park, SC;Chung, YC;Choi, BK. (2003). Contour-parallel offset machining without tool-retractions. *Computer-Aided Design.* 35(9), 841-849.

26. Kim, BH;Choi, BK. (2002). Machining efficiency comparison direction-parallel tool path with contour-parallel tool path. *Computer-Aided Design.* 34(2), 89-95.

27. Suresh, K;Yang, DCH. (1994). Constant scallop-height machining of free-form surfaces. *Journal of engineering for industry.* 116(2), 253-259.

28. Yoon, J-H. (2005). Fast tool path generation by the iso-scallop height method for ball-end milling of sculptured surfaces. *International Journal of Production Research.* 43(23), 4989-4998.

29. Li, H;Dong, Z;Vickers, GW. (1994). Optimal toolpath pattern identification for single island, sculptured part rough machining using fuzzy pattern analysis. *Computer-Aided Design.* 26(11), 787-795.

30. Jensen, CG. (1993). Analysis and synthesis of multi-axis sculptured surface machining. *Analysis and Synthesis of Multi-axis Sculptured Surface Machining.*

31. Chiou, CJ;Lee, YS. (1999). A shape-generating approach for multi-axis machining G-buffer models. *CAD Computer Aided Design.* 31(12), 761-776.

32. Chiou, C-J;Lee, Y-S. (2002). A machining potential field approach to tool path generation for multi-axis sculptured surface machining. *Computer-Aided Design.* 34(5), 357-371.

33. Han, Z;Yang, DCH. (1999). Iso-phote based tool-path generation for machining free-form surfaces. *Journal of Manufacturing Science and Engineering, Transactions of the ASME.* 121(4), 656-664.

34. Han, Z;Yang, DCH;Chuang, JJ. (2001). Isophote-based ruled surface approximation of free-form surfaces and its application in NC machining. *International Journal of Production Research.* 39(9), 1911-1930.

35. Ding, S;Mannan, MA;Poo, AN;Yang, DCH;Han, Z. (2003). Adaptive iso-planar tool path generation for machining of free-form surfaces. *CAD Computer Aided Design.* 35(2), 141-153.

36. Yang, DCH;Han, Z. (1999). Interference detection and optimal tool selection in 3-axis NC machining of free-form surfaces. *CAD Computer Aided Design.* 31(5), 303-315.

37. Yin, Z. (2004). Adaptive tool path generation from measured data. *Proceedings of the Institution of Mechanical Engineers, Part B: Journal of Engineering Manufacture.* 218(1), 103-111.

38. Lee, YS;Ji, H. (1997). Surface interrogation and machining strip evaluation for 5-axis CNC die and mold machining. *International Journal of Production Research.* 35(1), 225-252.

39. Faux, ID;Pratt, MJ. (1980). *Computational Geometry for Design and Manufacture*. Ellis Horwood Ltd.

40. CA, M;ELJ, B;SS, M. (2005). Critical point analysis of 3D vector field for 5-axis toolpath optimization. *In Proceedings of the 4th Asian Conference on Industrial Automation and Robotics ACIAR*.

41. Makhanov, S. (2007). Optimization and correction of the tool path of the five-axis milling machine: Part 1. Spatial optimization. *Mathematics and Computers in Simulation.* 75(5–6), 210-230.

42. Marshall, S;Griffiths, JG. (1994). A new cutter-path topology for milling machines. *Computer-Aided Design.* 26(3), 204-214.

43. Marshall, S;Griffiths, JG. (1994). A survey of cutter path construction techniques for milling machines. *International Journal of Production Research.* 32(12), 2861-2877.

44. Liu, X;Li, Y;Ma, S;Lee, C-h. (2015). A tool path generation method for freeform surface machining by introducing the tensor property of machining strip width. *Computer-Aided Design.* 66(1-13.

45. Butz, AR. (1968). Space filling curves and mathematical programming. *Information and Control.* 12(4), 314-330.

46. Butz, AR. (1969). Convergence with Hilbert's space filling curve. *Journal of Computer and System Sciences.* 3(2), 128-146.

47. Velho, L;Gomes, JdM. (1991). Digital halftoning with space filling curves. *SIGGRAPH Comput Graph.* 25(4), 81-90.

48. Dafner, R;Cohen-Or, D;Matias, Y. (2000). Context-based Space Filling Curves. *Computer Graphics Forum.* 19(3), 209-218.

49. Hafiane, A;Chaudhuri, S;Seetharaman, G;Zavidovique, B. (2006). Region-based CBIR in GIS with local space filling curves to spatial representation. *Pattern Recognition Letters.* 27(4), 259-267.

50. Griffiths, JG. (1994). Toolpath based on Hilbert's curve. *Computer-Aided Design.* 26(11), 839-844.

51. Cox, JJ;Takezaki, Y;Ferguson, HRP;Kohkonen, KE;Mulkay, EL. (1994). Space-filling curves in tool-path applications. *Computer-Aided Design.* 26(3), 215-224.

52. Hopcroft, JE;Ullman, JD. (1979). *Introduction to automata theory, languages, and computation*. Addison-Wesley.

53. Gan, W-F;Fu, J-Z;Shen, H-Y;Chen, Z-Y;Lin, Z-W. (2014). Five-axis tool path generation in CNC machining of T-spline surfaces. *Computer-Aided Design.* 52(51-63.

54. Lin, Z;Fu, J;Shen, H;Gan, W;Yue, S. (2015). Tool path generation for multi-axis freeform surface finishing with the LKH TSP solver. *Computer-Aided Design*.

55. Makhanov, SS;Anotaipaiboon, W (2003) Toolpath generation for five-axis NC machining using space-filling curves. In Proceedings of The Third Asian Conference on Industrial Automation and Robotics.

56. Sun, Y;Ren, F;Zhu, X;Guo, D. (2012). Contour-parallel offset machining for trimmed surfaces based on conformal mapping with free boundary. *International Journal of Advanced Manufacturing Technology.* 60(1-4), 261-271.

57. Dolen, M;Yaman, U. (2014). New morphological methods to generate two-dimensional curve offsets. *International Journal of Advanced Manufacturing Technology.* 71(9-12), 1687-1700.

58.   Can, A;Unuvar, A. (2010). A novel iso-scallop tool-path generation for efficient five-axis machining of free-form surfaces. *International Journal of Advanced Manufacturing Technology.* 51(9-12), 1083-1098.

59.   Anotaipaiboon, W;Makhanov, SS. (2005). Tool path generation for five-axis NC machining using adaptive space-filling curves. *International Journal of Production Research.* 43(8), 1643-1665.

60.   Moodleah, S;Makhanov, SS. (2015). 5-axis machining using a curvilinear tool path aligned with the direction of the maximum removal rate. *The International Journal of Advanced Manufacturing Technology.* 1-26.

61.   Anotaipaiboon, W;Makhanov, SS. (2008). Curvilinear space-filling curves for five-axis machining. *Computer-Aided Design.* 40(3), 350-367.

62.   Bohez, E;Makhanov, SS;Sonthipermpoon, K. (2000). Adaptive nonlinear tool path optimization for five-axis machining. *International Journal of Production Research.* 38(17), 4329-4343.

63.   Makhanov, SS;Ivanenko, SA. (2003). Grid generation as applied to optimize cutting operations of the five-axis milling machine. *Applied Numerical Mathematics.* 46(3–4), 331-351.

64.   Bieterman, MB;Sandstrom, DR. (2003). A Curvilinear Tool-Path Method for Pocket Machining. *Journal of Manufacturing Science and Engineering.* 125(4), 709-715.

65.   Sun, Y-W;Guo, D-M;Jia, Z-Y. (2006). Spiral cutting operation strategy for machining of sculptured surfaces by conformal map approach. *Journal of Materials Processing Technology.* 180(1–3), 74-82.

66.   Veeramani, D;Gau, YS. (1998). Issues in patch-by-patch machining of compound sculptured surfaces. *IIE Transactions (Institute of Industrial Engineers).* 30(4), 341-355.

67.   Veeramani, D;Gau, YS. (1998). Models for tool-path plan optimization in patch-by-patch machining. *International Journal of Production Research.* 36(6), 1633-1651.

68.   Lee, SG;Kim, HC;Yang, MY. (2008). Mesh-based tool path generation for constant scallop-height machining. *International Journal of Advanced Manufacturing Technology.* 37(1-2), 15-22.

69. Yang, DCH;Chuang, JJ;OuLee, TH. (2003). Boundary-conformed toolpath generation for trimmed free-form surfaces. *CAD Computer Aided Design.* 35(2), 127-139.

70. Yang, DCH;Chuang, JJ;Han, Z;Ding, S. (2003). Boundary-conformed toolpath generation for trimmed free-form surfaces via Coons reparametrization. *Journal of Materials Processing Technology.* 138(1-3), 138-144.

71. Li, CL. (2007). A geometric approach to boundary-conformed toolpath generation. *CAD Computer Aided Design.* 39(11), 941-952.

72. Gray, PJ;Bedi, S;Ismail, F. (2005). Arc-intersect method for 5-axis tool positioning. *CAD Computer Aided Design.* 37(7), 663-674.

73. Park, SC. (2003). Tool-path generation for Z-constant contour machining. *CAD Computer Aided Design.* 35(1), 27-36.

74. Park, SC. (2004). Sculptured surface machining using triangular mesh slicing. *Computer-Aided Design.* 36(3), 279-288.

75. Park, SC;Shin, H. (2002). Polygonal chain intersection. *Computers & Graphics.* 26(2), 341-350.

76. Xu, XJ;Bradley, C;Zhang, YF;Loh, HT;Wong, YS. (2002). Tool-path generation for five-axis machining of free-form surfaces based on accessibility analysis. *International Journal of Production Research.* 40(14), 3253-3274.

77. Lauwers, B;Kiswanto, G;Kruth, JP. (2003). Development of a Five-axis Milling Tool Path Generation Algorithm based on Faceted Models. *CIRP Annals - Manufacturing Technology.* 52(1), 85-88.

78. Zhang, K;Tang, K. (2014). An efficient greedy strategy for five-axis tool path generation on dense triangular mesh. *The International Journal of Advanced Manufacturing Technology.* 74(9-12), 1539-1550.

79. Xu, J;Sun, Y;Zhang, L. (2015). A mapping-based approach to eliminating self-intersection of offset paths on mesh surfaces for CNC machining. *Computer-Aided Design.* 62(131-142.

80. L, B;vy;Petitjean, S;Ray, N; Maillot, r. (2002). Least squares conformal maps for automatic texture atlas generation. *ACM Trans Graph.* 21(3), 362-371.

81. Nassehi, A;Essink, W;Barclay, J. (2015). Evolutionary algorithms for generation and optimization of tool paths. *CIRP Annals - Manufacturing Technology.*

82. Munlin, M;Makhanov, SS;Bohez, ELJ. (2004). Optimization of rotations of a five-axis milling machine near stationary points. *Computer-Aided Design.* 36(12), 1117-1128.

83. Affouard, A;Duc, E;Lartigue, C;Langeron, JM;Bourdet, P. (2004). Avoiding 5-axis singularities using tool path deformation. *International Journal of Machine Tools and Manufacture.* 44(4), 415-425.

84. Sørby, K. (2007). Inverse kinematics of five-axis machines near singular configurations. *International Journal of Machine Tools and Manufacture.* 47(2), 299-306.

85. Yang, J;Altintas, Y. (2013). Generalized kinematics of five-axis serial machines with non-singular tool path generation. *International Journal of Machine Tools and Manufacture.* 75(119-132.

86. Zou, Q;Zhang, J;Deng, B;Zhao, J. (2014). Iso-level tool path planning for free-form surfaces. *Computer-Aided Design.* 53(117-125.

87. Kumazawa, GH;Feng, H-Y;Barakchi Fard, MJ. (2015). Preferred feed direction field: A new tool path generation method for efficient sculptured surface machining. *Computer-Aided Design.* 67-68(1-12.

88. Lazoglu, I;Manav, C;Murtezaoglu, Y. (2009). Tool path optimization for free form surface machining. *CIRP Annals - Manufacturing Technology.* 58(1), 101-104.

89. Davim, JP. (2012). *Machining of complex sculptured surfaces*. Springer.

90. Bohez, EL;Makhanov, SS;Munlinb, M;Phien, HN;Tabucanon, MT. (2009). On 5-axis freeform surface machining optimization: vector field clustering approach. *International Journal of CAD/CAM.* 5(1).

91. Pottmann, H;Ravani, B. (2000). Singularities of motions constrained by contacting surfaces. *Mechanism and Machine Theory.* 35(7), 963-984.

92. Castagnetti, C;Duc, E;Ray, P. (2008). The Domain of Admissible Orientation concept: A new method for five-axis tool path optimisation. *CAD Computer Aided Design.* 40(9), 938-950.

93. Marciniak, K. (1987). Influence of surface shape on admissible tool positions in 5-axis face milling. *Computer-Aided Design.* 19(5), 233-236.

94. Kruth, J-P;Klewais, P. (1994). Optimization and Dynamic Adaptation of the Cutter Inclination during Five-Axis Milling of Sculptured Surfaces. *CIRP Annals - Manufacturing Technology.* 43(1), 443-448.

95. Gani, EA;Kruth, JP;Vanherck, P;Lauwers, B. (1997). A geometrical model of the cut in five-axis milling accounting for the influence of tool orientation. *The International Journal of Advanced Manufacturing Technology.* 13(10), 677-684.

96. Elber, G. (1995). Freeform surface region optimization for 3-axis and 5-axis milling. *Computer-Aided Design.* 27(6), 465-470.

97. Lo, C-C. (1999). Real-time generation and control of cutter path for 5-axis CNC machining. *International Journal of Machine Tools and Manufacture.* 39(3), 471-488.

98. Rao, A;Sarma, R. (2000). On local gouging in five-axis sculptured surface machining using flat-end tools. *Computer-Aided Design.* 32(7), 409-420.

99. Li, Z;Chen, W. (2006). A global cutter positioning method for multi-axis machining of sculptured surfaces. *International Journal of Machine Tools and Manufacture.* 46(12–13), 1428-1434.

100. Warkentin, A;Ismail, F;Bedi, S. (1998). Intersection approach to multi-point machining of sculptured surfaces. *Computer Aided Geometric Design.* 15(6), 567-584.

101. Yoon, JH;Pottmann, H;Lee, YS. (2003). Locally optimal cutting positions for 5-axis sculptured surface machining. *CAD Computer Aided Design.* 35(1), 69-81.

102. Jun, CS;Cha, K;Lee, YS. (2003). Optimizing tool orientations for 5-axis machining by configuration-space search method. *CAD Computer Aided Design.* 35(6), 549-566.

103. Gray, P;Bedi, S;Ismail, F. (2003). Rolling ball method for 5-axis surface machining. *CAD Computer Aided Design.* 35(4), 347-357.

104. Hosseinkhani, Y;Akbari, J;Vafaeesefat, A. (2007). Penetration-elimination method for five-axis CNC machining of sculptured surfaces. *International Journal of Machine Tools and Manufacture.* 47(10), 1625-1635.

105. Kim, Y-J;Elber, G;Bartoň, M;Pottmann, H. (2015). Precise gouging-free tool orientations for 5-axis CNC machining. *Computer-Aided Design.* 58(0), 220-229.

106. Radzevich, SP. (2005). A cutting-tool-dependent approach for partitioning of sculptured surface. *Computer-Aided Design.* 37(7), 767-778.

107. Tang, TD;Bohez, ELJ;Koomsap, P. (2007). The sweep plane algorithm for global collision detection with workpiece geometry update for five-axis NC machining. *Computer-Aided Design.* 39(11), 1012-1024.

108. Elber, G;Cohen, E. (1999). A unified approach to verification in 5-axis freeform milling environments. *Computer-Aided Design.* 31(13), 795-804.

109. Beudaert, X;Pechard, P-Y;Tournier, C. (2011). 5-Axis tool path smoothing based on drive constraints. *International Journal of Machine Tools and Manufacture.* 51(12), 958-965.

110. Morishige, K;Takeuchi, Y. (1997). 5-axis control rough cutting of an impeller with efficiency and accuracy. *Robotics and Automation, 1997. Proceedings., 1997 IEEE International Conference on.* 1241-1246 vol.1242.

111. Morishige, K;Takeuchi, Y;Kase, K. (1999). Tool path generation using C-space for 5-axis control machining. *Journal of Manufacturing Science and Engineering, Transactions of the ASME.* 121(1), 144-149.

112. Tulsyan, S;Altintas, Y. (2015). Local toolpath smoothing for five-axis machine tools. *International Journal of Machine Tools and Manufacture.* 96(15-26.

113. Bi, Q;Shi, J;Wang, Y;Zhu, L;Ding, H. (2015). Analytical curvature-continuous dual-Bézier corner transition for five-axis linear tool path. *International Journal of Machine Tools and Manufacture.* 91(0), 96-108.

114. Farouki, RT;Han, CY;Li, S. (2014). Inverse kinematics for optimal tool orientation control in 5-axis CNC machining. *Computer Aided Geometric Design.* 31(1), 13-26.

115. Radzevich, SP. (2007). *Kinematic geometry of surface machining*. CRC Press.

116. Radzevich, SP;Goodman, ED. (2002). Computation of optimal workpiece orientation for multi-axis NC machining of sculptured part surfaces. *Journal of Mechanical Design, Transactions of the ASME.* 124(2), 201-212.

117. Hu, P;Tang, K. (2011). Improving the dynamics of five-axis machining through optimization of workpiece setup and tool orientations. *Computer-Aided Design.* 43(12), 1693-1706.

118. Anotaipaiboon, W;Makhanov, SS;Bohez, ELJ. (2006). Optimal setup for five-axis machining. *International Journal of Machine Tools and Manufacture.* 46(9), 964-977.

119. Chih-Ching, L. (1998). A new approach to CNC tool path generation. *Computer-Aided Design.* 30(8), 649-655.

120. Erdim, H;Lazoglu, I;Ozturk, B. (2006). Feedrate scheduling strategies for free-form surfaces. *International Journal of Machine Tools and Manufacture.* 46(7-8), 747-757.

121. Qian, L;Yang, B;Lei, S. (2008). Comparing and combining off-line feedrate rescheduling strategies in free-form surface machining with feedrate acceleration and deceleration. *Robotics and Computer-Integrated Manufacturing.* 24(6), 796-803.

122. Ko, JH;Yun, WS;Cho, DW. (2003). Off-line feed rate scheduling using virtual CNC based on an evaluation of cutting performance. *CAD Computer Aided Design.* 35(4), 383-393.

123. Fussell, BK;Jerard, RB;Hemmett, JG. (2003). Modeling of cutting geometry and forces for 5-axis sculptured surface machining. *CAD Computer Aided Design.* 35(4), 333-346.

124. Bailey, T;Elbestawi, MA;El-Wardany, TI;Fitzpatrick, P. (2002). Generic simulation approach for multi-axis machining, Part 1: Modeling methodology. *Journal of Manufacturing Science and Engineering, Transactions of the ASME.* 124(3), 624-633.

125. López de Lacalle, LN;Lamikiz, A;Sánchez, JA;Salgado, MA. (2007). Toolpath selection based on the minimum deflection cutting forces in the programming of complex surfaces milling. *International Journal of Machine Tools and Manufacture.* 47(2), 388-400.

117

126. Creighton, E;Honegger, A;Tulsian, A;Mukhopadhyay, D. (2010). Analysis of thermal errors in a high-speed micro-milling spindle. *International Journal of Machine Tools and Manufacture.* 50(4), 386-393.

127. Haitao, Z;Jianguo, Y;Jinhua, S. (2007). Simulation of thermal behavior of a CNC machine tool spindle. *International Journal of Machine Tools and Manufacture.* 47(6), 1003-1010.

128. Ramesh, R;Mannan, MA;Poo, AN;Keerthi, SS. (2003). Thermal error measurement and modelling in machine tools. Part II. Hybrid Bayesian Network—support vector machine model. *International Journal of Machine Tools and Manufacture.* 43(4), 405-419.

129. Vanherck, P;Dehaes, J;Nuttin, M. (1997). Compensation of thermal deformations in machine tools with neural nets. *Computers in Industry.* 33(1), 119-125.

130. Bohez, ELJ. (2002). Compensating for systematic errors in 5-axis NC machining. *CAD Computer Aided Design.* 34(5), 391-403.

131. Seames, W. (2001). *Computer Numerical Control: Concepts &amp; Programming*. Cengage Learning.

132. Apro, K. (2008). *Secrets of 5-Axis Machining*. Industrial Press Inc.

133. Xu, X. (2009). *Integrating advanced computer-aided design, manufacturing, and numerical control: principles and implementations*. Information Science Reference Hershey.

134. Callaghan, R (2007) Machine tool and motion error standardized definitions for simplified error modeling. Tech. Report (Independent Quality Labs, Inc., 2007),

135. Ibaraki, S;Sawada, M;Matsubara, A;Matsushita, T. (2010). Machining tests to identify kinematic errors on five-axis machine tools. *Precision Engineering.* 34(3), 387-398.

136. Wang, M;Hu, J;Zan, T. (2010). Kinematic error separation on five-axis NC machine tool based on telescoping double ball bar. *Frontiers of Mechanical Engineering in China.* 5(4), 431-437.

137. Tsutsumi, M;Tone, S;Kato, N;Sato, R. (2013). Enhancement of geometric accuracy of five-axis machining centers based on identification and

compensation of geometric deviations. *International Journal of Machine Tools and Manufacture.* 68(11-20).

138. Tutunea-Fatan, OR;Bhuiya, MSH. (2011). Comparing the kinematic efficiency of five-axis machine tool configurations through nonlinearity errors. *Computer-Aided Design.* 43(9), 1163-1172.

139. Schmitz, TL;Ziegert, JC;Canning, JS;Zapata, R. (2008). Case study: A comparison of error sources in high-speed milling. *Precision Engineering.* 32(2), 126-133.

140. Lim, EM;Menq, C-H. (1995). The prediction of dimensional error for sculptured surface productions using the ball-end milling process. Part 2: Surface generation model and experimental verification. *International Journal of Machine Tools and Manufacture.* 35(8), 1171-1185.

141. Iwabe, H;Fujii, Y;Saito, K;Kishinami, T. (1994). Study on corner cut by end mill: analysis of cutting mechanism and new cutting method at inside corner. *International Journal of the Japan Society for Precision Engineering.* 28(3), 218-223.

142. Matsubara, T;Tanaka, H;Mizumoto, H. (1991). Study on accuracy in end-mill operations (2nd report). Machining accuracy in side cutting tests. *International Journal of the Japan Society for Precision Engineering.* 25(4), 291-296.

143. Law, K (1998) Process design for error compensation in end milling of pockets. M. Phil. Thesis, City University of Hong Kong.

144. Law, KM;Geddam, A;Ostafiev, V. (1999). A process-design approach to error compensation in the end milling of pockets. *Journal of Materials Processing Technology.* 89(238-244.

145. Law, KM;Geddam, A. (2003). Error compensation in the end milling of pockets: a methodology. *Journal of Materials Processing Technology.* 139(1), 21-27.

146. Ramesh, R;Mannan, M;Poo, A. (2003). Thermal error measurement and modelling in machine tools.: Part I. Influence of varying operating conditions. *International Journal of Machine Tools and Manufacture.* 43(4), 391-404.

147. Donmez, MA;Hahn, MH;Soons, JA. (2007). A Novel Cooling System to Reduce Thermally-Induced Errors of Machine Tools. *CIRP Annals - Manufacturing Technology.* 56(1), 521-524.

148. Kim, T;Sarma, SE. (2002). Toolpath generation along directions of maximum kinematic performance; A first cut at machine-optimal paths. *CAD Computer Aided Design.* 34(6), 453-468.

149. Weck, M. (1984). *Handbook of Machine Tools: Metrological analysis and performance tests*, vol 4. Wiley.

150. Bohez, EL;Ariyajunya, B;Sinlapeecheewa, C;Shein, TMM;Belforte, G. (2007). Systematic geometric rigid body error identification of 5-axis milling machines. *Computer-Aided Design.* 39(4), 229-244.

151. Jung, J-H;Choi, J-P;Lee, S-J. (2006). Machining accuracy enhancement by compensating for volumetric errors of a machine tool and on-machine measurement. *Journal of Materials Processing Technology.* 174(1), 56-66.

152. Marin, RA;Ferreira, PM. (2003). Analysis of the influence of fixture locator errors on the compliance of work part features to geometric tolerance specifications. *Journal of Manufacturing Science and Engineering.* 125(3), 609-616.

153. Lee, Y-S. (1998). Non-isoparametric tool path planning by machining strip evaluation for 5-axis sculptured surface machining. *Computer-Aided Design.* 30(7), 559-570.

154. Lee, YS. (1998). Mathematical modelling using different endmills and tool placement problems for 4- and 5-axis NC complex surface machining. *International Journal of Production Research.* 36(3), 785-814.

155. Dong, J;Ferreira, PM;Stori, JA. (2007). Feed-rate optimization with jerk constraints for generating minimum-time trajectories. *International Journal of Machine Tools and Manufacture.* 47(12-13), 1941-1955.

156. Kim, T;Sarma, SE. (2002). Toolpath generation along directions of maximum kinematic performance; a first cut at machine-optimal paths. *Computer-Aided Design.* 34(6), 453-468.

157. Li, LL;Zhang, YF;Li, HY;Geng, L. (2011). Generating tool-path with smooth posture change for five-axis sculptured surface machining based on cutter's

accessibility map. *The International Journal of Advanced Manufacturing Technology.* 53(5-8), 699-709.

158. Anotaipaiboon, W;Makhanov, SS. (2011). Minimization of the kinematics error for five-axis machining. *Computer-Aided Design.* 43(12), 1740-1757.

159. Castillo, JE;Otto, JS. (2000). Numerical techniques for the transformation to an orthogonal coordinate system aligned with a vector field. *Computers &amp; Mathematics with Applications.* 40(4-5), 523-535.

160. Brackbill, JU;Saltzman, JS. (1982). Adaptive zoning for singular problems in two dimensions. *Journal of Computational Physics.* 46(3), 342-368.

161. Giannakopoulos, AE;Engel, AJ. (1988). Directional control in grid generation. *Journal of Computational Physics.* 74(2), 422-439.

162. Winslow, AM. (1966). Numerical solution of the quasilinear poisson equation in a nonuniform triangle mesh. *Journal of Computational Physics.* 1(2), 149-172.

163. Vorburger, TV;Raja, J. (1990). *Surface Finish Metrology Tutorial*. National Inst. of Standards and Technology.

164. A, T. (1998). Function: The Key to Surface Finish Requirements. *In Proc of 4th Biennial International Manufacturing Technology Conference Session 8.*

165. American National Standard. ASME/ANSI B46.1-1985. Surface Texture. American Society of Mechanical Engineers (1985). New York,

166. Gaspar, M;Weichert, F. (2013). Integrated construction and simulation of tool paths for milling dental crowns and bridges. *Computer-Aided Design.* 45(10), 1170-1181.

167. Bern, MW;Eppstein, D. (2000). Quadrilateral Meshing by Circle Packing. *Int J Comput Geometry Appl.* 10(4), 347-360.

168. Frey, PJ;George, P-L (2010) Mesh Optimization. In: Mesh Generation. ISTE, 591-622.

169. Siladic, MF (1988) Numerical grid generation and potential airfoil analysis and design. DTIC Document.

170. 3D Systems Inc, Stereolithography Interface Specification. P/N 50065-S01-00 (1989).

171. The Initial Graphics Exchange Specification (IGES) Version 5.0 (1990). National Institute of Standards and Technology ,Gaithersburg, MD.

172. ISO 10303-21:2002 Industrial automation systems and integration -- Product data representation and exchange -- Part 21: Implementation methods: Clear text encoding of the exchange structure (2002).

173. Automatisation industrielle. Representation externe des donnees de definition de produits. Specification du standard d'echange et de transferts (SET), Version 85-08, Z68-300, Association Francaise de Normalisation (AFNOR) 85181 (1985). Paris.

174. http://en.wikipedia.org/wiki/CATIA.

175. http://en.wikipedia.org/wiki/PHIGS.

176. Marcum, DL;Gaiter, JA. (1999). Unstructured surface grid generation using global mapping and physical space approximation. *8th International Meshing Roundtable*. 397–406.

177. Eck, M;DeRose, T;Duchamp, T;Hoppe, H;Lounsbery, M;Stuetzle, W (1995). Multiresolution analysis of arbitrary meshes. Paper presented at the *Proceedings of the 22nd annual conference on Computer graphics and interactive techniques*, 173-182.

178. Floater, MS. (1997). Parametrization and smooth approximation of surface triangulations. *Comput Aided Geom Des.* 14(3), 231-250.

179. Sheffer, A;de Sturler, E. (2001). Parameterization of faceted surfaces for meshing using angle-based flattening. *Engineering with Computers.* 17(3), 326-337.

180. McCartney, J;Hinds, BK;Seow, BL. (1999). The flattening of triangulated surfaces incorporating darts and gussets. *Computer-Aided Design.* 31(4), 249-260.

181. Zhong, Y;Xu, B. (2006). A physically based method for triangulated surface flattening. *Computer-Aided Design.* 38(10), 1062-1073.

182. Xu, J;Jin, C. (2013). Boundary-conformed machining for trimmed free-form surfaces based on mesh mapping. *International Journal of Computer Integrated Manufacturing.* 26(8), 720-730.

183. Saroul, L (2006) Surface extraction and flattening for anatomical visualization. Université de Saint-Etienne, France.

184. http://www.resurf3d.com/MeshFlatten_standalone.htm.

185. Rusinkiewicz, S (2004). Estimating Curvatures and Their Derivatives on Triangle Meshes. Paper presented at the *Proceedings of the 3D Data Processing, Visualization, and Transmission, 2nd International Symposium*, 486-493.

186. Gilles, P;Cohen, G;Monies, F;Rubio, W. (2013). Torus cutter positioning in five-axis milling using balance of the transversal cutting force. *The International Journal of Advanced Manufacturing Technology*. 66(5-8), 965-973.

# Appendix A

## List of Publications

**International Journals**

1. Moodleah, S;Makhanov, SS. (2015). 5-axis machining using a curvilinear tool path aligned with the direction of the maximum removal rate. *The International Journal of Advanced Manufacturing Technology.* 1-26.

2. Moodleah, S; Bohez, EL;Makhanov, SS. (2015). Five-Axis Machining of the STL Surfaces by Adaptive Curvilinear Toolpaths. *International Journal of Production Research.* [submitted Jun 15 2015].

**International Conferences**

1. Moodleah, S;Makhanov, SS. (2014). Vector Field Aligned Grids for 5-Axis Machining of Dental Parts. *The Fifth International Conference on Information and Communication Technology for Embedded Systems.*

2. Moodleah, S;Makhanov, SS. (2013). Optimization of 5-axis machining with application to dental implants. *The Second Asian Conference on Information Systems.*